High Temperature Nanoindentation Characterisation of P91 and P92 Steel

Michael I Davies

The University of Nottingham

Thesis submitted to the University of Nottingham for the Degree of Doctor of Philosophy

July 2013

Abstract

Modern demands in power generation call for higher efficiencies from every area of the power plant. One aspect of this is a drive to increase plant operating temperatures placing higher demand on structural materials. P91 and P92 are two steels commonly used in steam pipes. In order to accurately predict the service lifetime of components, mechanical properties at operating temperatures are critical. In particular properties of material around weld fusion joints are of interest as it is in these regions where failures occur.

Conventional techniques such as Vicker's hardness testing and uniaxial tensile testing are used to characterise the mechanical properties and creep behaviour of bulk materials. These techniques are often used to determine the properties of P91 and P92 parent and weld materials, the limitation of these techniques is that they require large volumes of material. They are therefore unable to determine differences in properties through the heat affected zone of the parent material which is typically only a few millimetres across.

Nanoindentation is a technique which offers a potential solution to this problem. It was developed in order to examine the properties of thin films and small material volumes. In recent years several approaches have been developed to perform nanoindentation experiments at elevated temperature. These approaches have been examined in order to establish which provides the best thermal stability for high temperature nanoindentation measurements. This technique has then been used to perform high temperature nanoindentation experiments to determine the mechanical properties and creep behaviour of P91 and P92 steel.

The correlation between nanoindentation measurements on bulk materials and those obtained using conventional methods is examined. In particular the significance of creep stress exponents calculated from nanoindentation dwell

Abstract

data is discussed. Nanoindentation is then used to characterise the heat affected zone of a weld, giving clear indications of the effects of microstructural differences on the material properties.

Acknowledgments

Nomenclature

Roman

A	nm^2	Projected indentation contact area
A$_p$	nm^2	Indenter area
a	-	Dimensionless constant
b	-	Dimensionless constant
C	nm/mN	Contact compliance
C$_f$	nm/mN	Compliance of instrument frame
c	-	Material dependent constant
E	GPa	Young's modulus
E$_i$	GPa	Indenter Young's modulus
E$_r$	GPa	Reduced modulus
E(t)	GPa	Relaxation modulus
H	GPa	Nanoindentation hardness
HV	GPa	Vicker's hardness
h	nm	Indentation depth
h$_c$	nm	Contact depth
h$_f$	nm	Final indentation depth
h$_{max}$	nm	Maximum indentation depth
$\dot{h}_{creep}$	nm/s	Rate of change of indentation depth
m	-	Geometry dependent fitting coefficient
m(t)	-	Time dependent fitting coefficient
n	-	Norton creep stress exponent
P	mN	Applied load
P$_{max}$	mN	Maximum experimental load
$\dot{P}_{creep}$	mN/s	Rate of change of load
Q	kJmol^{-1}	Activation energy

R	$JK^{-1}mol^{-1}$	Gas constant – 8.314
S	mN/nm	Contact stiffness
T	K	Temperature
t	s	Time

Greek

α	$^{o}C^{-1}$	Coefficient of thermal expansion
β	-	Geometric correction factor
$\dot{\varepsilon}$	s^{-1}	Strain rate
ϵ	-	Dimensionless constant
η	GPa.s	Viscosity
θ	^{o}	Indenter included half angle
σ	MPa	Stress
v	-	Poisson's ratio
v_i	-	Indenter Poisson's ratio

Table of Contents

Table of Figures

Table of Figures

Chapter 1 – Introduction

Since the industrial revolution of the 18th century fossil fuels have played an integral role in power generation. This revolution led not only to increased agricultural and industrial production but also unprecedented sustained population growth. Modern human life is dependent on the generation of electricity to power homes and commerce. This has led to ever increasing demands on natural resources and increasing pressure on ecosystems as a result of pollution from the by-products of fossil fuel combustion.

In recent decades public interest has turned to the generation of power by more environmentally friendly methods. There are two main ways to achieve this goal either by using environmentally neutral methods to generate so called "green energy" or by increasing the efficiency of current fossil fuel burning plants in order to minimise fuel consumption per unit of electricity. One way to achieve the latter is by increasing the operating temperature of the power plant. This has led to an increased interest in the mechanical properties and creep behaviour of structural materials at increased operating temperatures. The ability of existing plant equipment to meet modern demands is very much dependent on the high temperature stability of mechanical properties and creep behaviour compared to their conventional operating temperature. Welded components are seen very often in power plant applications (e.g. headers, pipe-work and chests). Many of these components operate at high temperatures and under high pressures. Due to the nature of their in service conditions, these components are often susceptible to failure[1, 2].

Modified 9Cr or grade P91 (ASTM A335 P91) is a modern steel which was developed by Oakridge National laboratory as a replacement for 1/2CrMoV (BS3604 grade 660) components suffering from ligament cracking. P91 first entered service in the UK in the late nineteen eighties. Although the new steel has only been in service for approximately half its design life, it has suffered a higher than expected incidence of weld cracking[2, 3]. Due to the service

1

Introduction

history of this material, it requires structural integrity assessments to justify its continued operation. Therefore research has also focused on the development of improved steel grades with increased rupture strength at elevated temperature. One such grade is P92 developed by Nippon steel in the early nineteen nineties[4].

As part of the approval process and subsequent failure analysis many conventional macro and micro scale tests have been used to characterise the mechanical properties and creep properties of the steel and weld materials. The most commonly used tests in characterising power station grade steels are uniaxial tensile tests [3, 5-7]. These are widely proven, accredited and well established testing techniques. Data from these tests is typically entered into creep models in order to make lifetime assessments for the materials [3, 8-10]. The stages of creep observed in a uniaxial tensile test are shown in Figure 1 below. When the stress is applied the material initially undergoes high strain rate deformation designated as primary creep. The strain rate slows over time until the material reaches a state of steady strain increase which is called secondary creep. In the tertiary creep regime there is a dramatic increase in the strain rate as the material fails and ruptures under the applied stress.
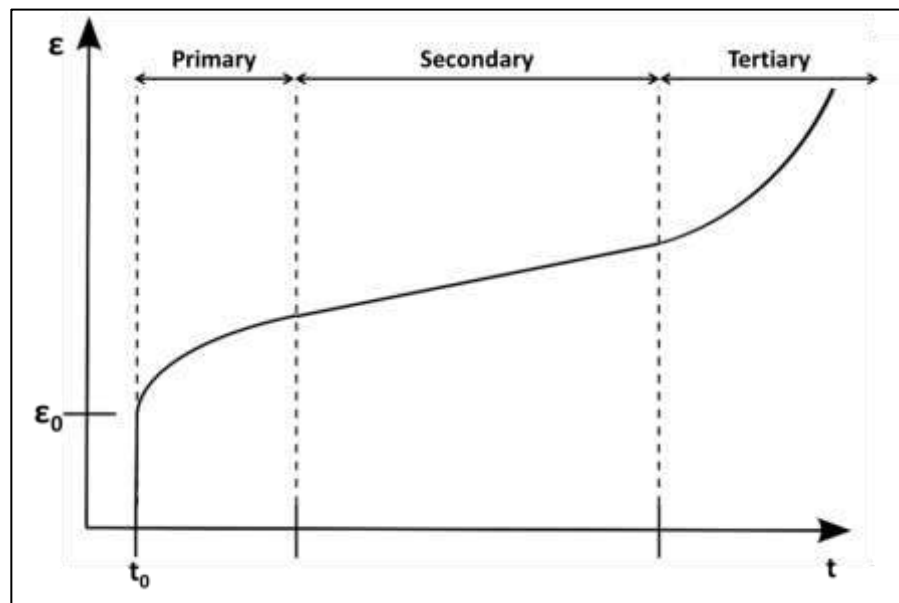
Figure 1: Stages of creep
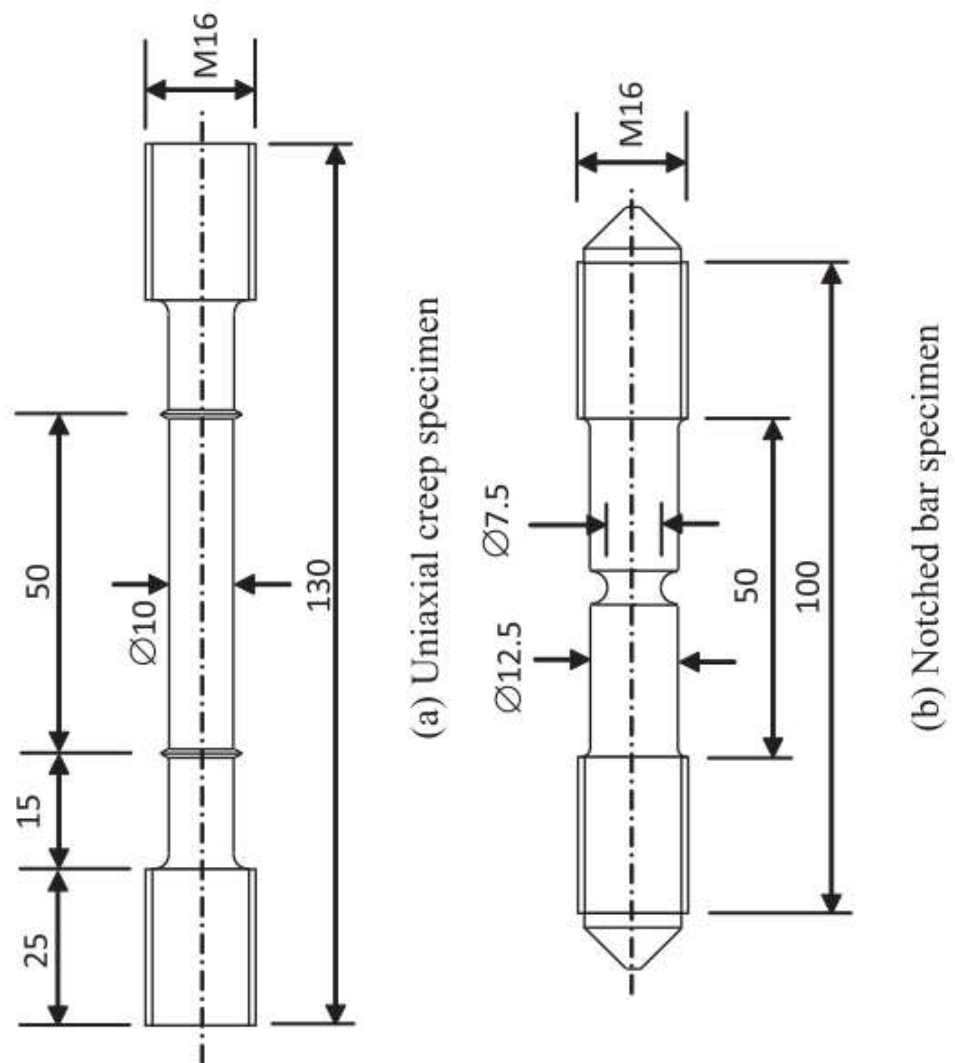
Figure 2: Typical uniaxial tensile test specimen geometry, from Saber et al.[8]

Introduction

Uniaxial tests use very specific sample geometries, the two most common are shown in Figure 2. In uniaxial testing the test specimen is clamped at either end and a continuous stress is applied, the change in strain is then monitored with respect to time. Experiments are performed at a range of different stresses in order to drive different strain rates. Uniaxial creep experiments typically collect data for several hundred hours in order to allow the material to go through the different stages of creep. This data is the assessed using creep models to evaluate the creep damage characteristics of the material under test[11].

Uniaxial tensile experiments are typically performed under very specific stress states as many materials will show differing behaviour depending on the applied stress. Figure 3 shows the stress dependence of the secondary creep strain rate for P91 steel. There is a clear difference between the creep rates observed in high and low stress states. The creep behaviour of P91 is also very highly temperature dependent. Figure 3 also shows the differences in creep rates observed at 600, 625 and 650°C. As we might expect, as the test temperature is increased, the strain rate at any given stress increases. This highlights why high temperature material characterisation is vital in predicting the behaviour and potential lifetime of these materials at increased operating temperatures.
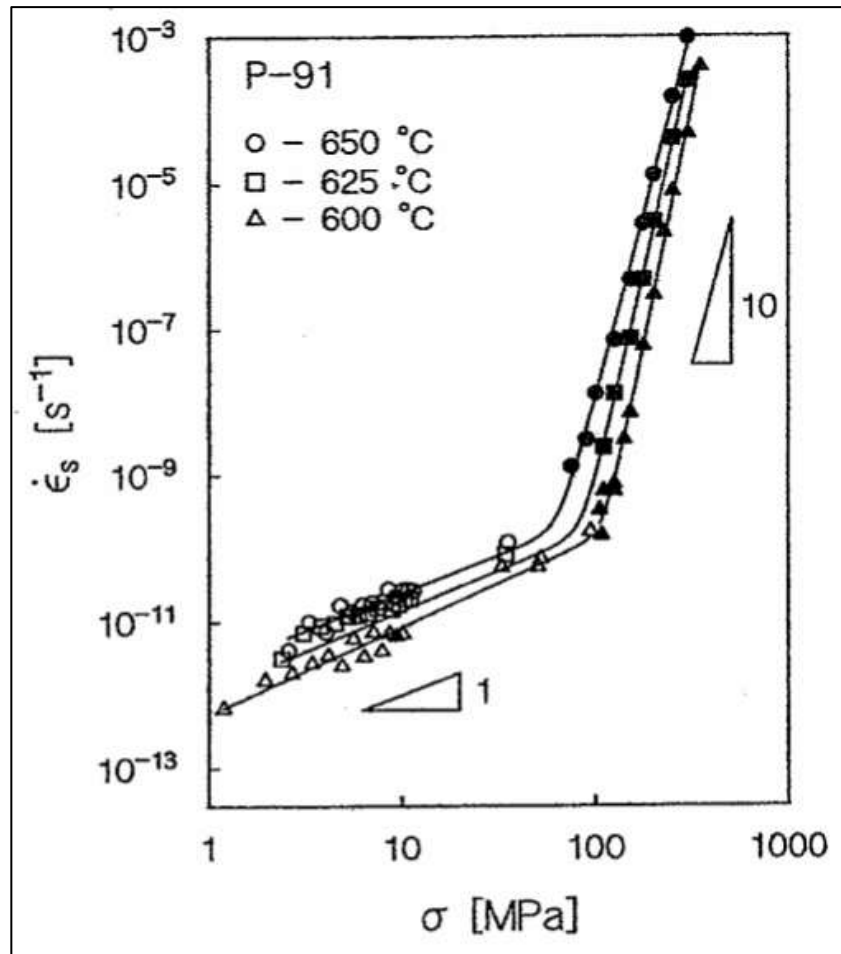
Figure 3: Dependence on secondary state creep rate on stress from Klueh[12]

Many uniaxial test rigs incorporate furnaces so that samples can be tested at elevated temperatures to determine the elastic, plastic and creep properties. One limitation of these tests is that they require relatively large volumes of material in order to make samples of the required geometry. Conventional uniaxial testing cannot be accurately employed to determine material properties for such graded structures such as power plant pipe welds, where the heat affected zone in the parent material is typically 2-4mm width and has a very different microstructure to the bulk parent material [13, 14]. These structures are typically found around fusion joints and repair welds[15].

Introduction

The work described in this thesis will focus one particular type of fusion joint which is discussed in greater detail in Section 3.4.1. In a fusion joint variation of creep properties perpendicular to the fusion line due to the difference of metallurgical features. These are typically classified as three distinct material features, the parent material, the weld material and the heat affected zone. The heat affected zone has two micro structurally distinct regions, a high temperature coarse grained region and a low temperature fine grained region. Previous experiments has found that it is the fine grained region in which type IV cracking occurs, type IV failure refers explicitly to failure as the result of the formation of creep voids in the heat affected zone of a welded cross section[16]. An example of type IV creep void formation from the work of Ogata et al. is shown in Figure 4[5]. Material property characteristics of the different grain structures are of extreme significance when trying to determine the failure characteristics of the weld, therefore test techniques are required which can be used to test smaller volumes of material than conventional uniaxial tests.
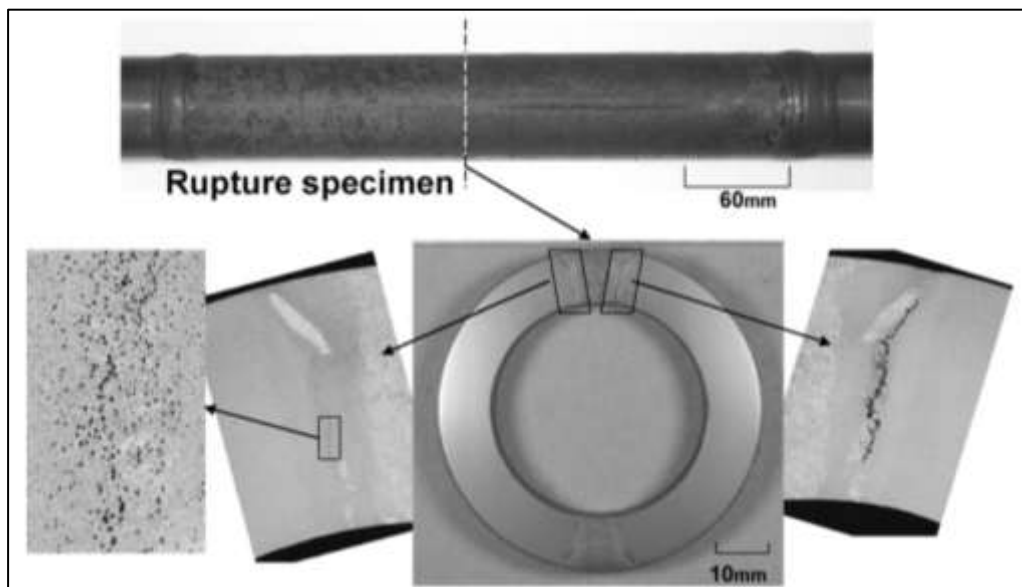
Figure 4: Type IV failure of a welded pipe section from Ogata et al.[5]

Chapter 2 – Literature review

One technique which has been developed specifically for performing small scale creep tests is the impression creep test. This does not require the removal material from the test vessel so full pipe sections can be tested. This technique can also obtain material properties from a relatively small volume of material [17]. This has the benefit that there is no need for repair of the vessel with the associated cost but also means that it is possible to characterise the heat affected zone of welds. This type of test does not generate tertiary creep behaviour i.e. no creep failures, therefore this test is also more stable and suitable for brittle materials[18].

Impression creep testing uses indenters of uniform cross section to provide constant stress as the size of the indent increases. The size of the test specimen is only limited by the size of the probe used. Typically flat bottomed cylindrical punch is pushed into the surface of the sample and the penetration depth monitored with time for several hundred hours. Punches are typically made of stainless steel or tungsten carbide at temperatures above 650°C. The advantages over conventional creep testing are that only a small quantity of test material is needed allowing testing of individual zones in the structure of the sample. Constant stress can be obtained with a constant load. Temperature and stress dependence of the steady state can be obtained from a single test sample [19-25].

A large volume of research has focussed on relating the results of impression creep tests to the behaviour of materials in uniaxial testing [23, 26-28]. One of the developments from this area of research is the accurate assessments of conversion factors which relate to the creep deformation rate in the impression creep test to an equivalent uniaxial creep strain. This is done using finite element models to evaluate the influence of the contact geometry on the creep strain[27]. One additional development is a change from using cylindrical probes to rectangular cross section probes in impression creep tests. This is done to remove problems associated with the singularities in the

stress field around the edge of cylindrical probes from the FE evaluation of the conversion factors[23].

 Previous work has been conducted using the impression creep technique to characterise material across a weld containing grade P91 steel as the parent material and a variety of fillers [3, 7, 8, 11, 12]. This was compared with data from the parent and weld material obtained by conventional uniaxial testing. Data was acquired at both room temperature and at 923K (just above the operating temperature of the grade P91 steel parent material weld) for conventional uniaxial testing and at 923K for the impression creep test technique. The findings of such previous works show that the impression creep testing technique produced comparable results to that of the conventional uniaxial testing, and so the technique was validated for the P91 steel weld.

As mentioned, these experimental techniques were limited in the size of the region they can investigate by the size of the probe and still took several hundred hours to gather data. In order to target smaller regions, techniques using indentation data to determine creep properties were developed. In the 1990's in microindentation tests on copper and steel were performed in order to evaluate creep behaviour[29]. These results were based on monitoring the size of the hardness impression and so the size of the investigated region was limited by the size of impression for which a change in the contact area could be observed. Nanoindentation provides the apparently ideal solution, very small volumes of material can be tested and as much smaller displacements can be measured, the tests can be performed much faster. Calculations can be made from a few minutes of sample data at peak load instead of several hundred hours.

Nanoindentation is becoming ever more established as an accepted technique for the extraction of mechanical properties of thin coatings, and samples too small to be easily tested using other methods [30-33]. Room temperature indentation testing has previously been used to characterise the mechanical

properties of welds [33, 34] and also to evaluate the change in properties through the heat affected zone of a weldment [35] . Elevated temperature nanoindentation has developed as a logical progression of nanoindentation as a means of testing samples under industrially relevant conditions. High temperature Nanoindentation is a relatively young field having only been developed in the last two decades and there is still a degree of uncertainty around which methods provide the most accurate and repeatable assessment of sample properties.

Depth sensing instrumentation led on from Vickers hardness testing, which uses the size of the residual contact impression to determine the hardness of bulk materials [11]. As thinner coatings were developed, the size of the impressions that were made to test them became too small for optical imaging. Small indents are made typically with a Berkovich geometry indenter, which is a triangle based pyramid rather than the square based Vickers indenter. The Berkovich geometry has same area to depth ratio as Vickers Indenter, but it is much easier to polish the Berkovich indenter to the sharp point needed for low depth indentation [36]. Initially other types of microscopy were used to measure the size of the indents [37]. This gave accurate results on some samples but the technique is time consuming and cannot include elastically recovered depth common in low load indents. Depth sensing indentation instrumentation was developed to allow the depth change for an applied load to be measured [38-40]. Methods were developed to extract Young's modulus and hardness from the data by analysing the loading and unloading curves [41]. The method used for data analysis in most commercially available nanoindenters was developed by Oliver and Pharr [42]. This method uses the depth data collected during experiments to determine projected contact areas which are then used to determine mechanical properties. Although widely used, this analysis has several material dependent limitations as a result of the estimation of contact area which is used to calculate the hardness and Young's modulus.

Literature review

One limitation of the analysis technique is the inability to account for pile up in the analysis. Pile up refers to material displaced from the sample surface and at the edge of an indent, but which still supports some of the indenter load. This material is not accounted for in Oliver and Pharr's contact area calculation as this is based on distance from the initial contact surface, so pileup around an indent can lead to underestimation of the contact area [43]. This has also been shown to be true for conventional hardness testing [44] although in this case the pileup is detected by the measurement imaging. In indentations on materials where the material deformation is largely plastic, pileup can lead to overestimation of hardness and elastic modulus. The effect of pileup is less predominant in materials that work harden which tend to display sink-in behaviour [45]. Sink-in describes the opposite effect whereby the material under load falls away from the edge of the indenter, the Oliver and Pharr method is much more accurate in predicting the contact area for materials which sink-in [46].

Another limitation of conventional analysis techniques is indentation size effects (ISE). This refers to the observed increase in material hardness at small length scales. The effect can be explained by considering the large strain gradients in small indentations which lead to geometrically necessary dislocations causing the observed hardening. Geometrically necessary dislocations, GND's, are those required in order to account for the permanent changes in the shape of the surface under indentation. Nix and Gao proposed that the hardness was connected to the depth by the relation in Equation 1.

$$\left(\frac{H}{H_0}\right)^2 = 1 + \frac{h^*}{h}$$

Equation 1

Where h^* is a characteristic depth, determined from the material properties and indenter shape and H_0 is the hardness at depths $h \gg h^*$ [47]. Under this

regime H^2 should increase linearly with h^{-1}. This relationship fits well for most micro-indentation data but does not correlate with experimental Nanoindentation data, depths below 0.2µm, or micro indentation with a spherical indenter.

Qu et al. and Xue et al. investigated the hypothesis that the discrepancy in the ISE model was due it not considering the shape of the indenter at its very tip [48].By considering the contact between the sample and a conical, or Berkovich, indenter with a spherical tip a model was created which more accurately predicted the ISE for Nanoindentation. [48, 49]. However, Zhang et al. [50] found that indenter tip radius could not be the main factor in explaining the difference between the Nix-Gao model and experimental results. This is because the indenter tip radius no longer affects the hardness once the contact radius exceeds one half of the indenter radius [48]. In most indenters the tip radius is <100nm so there is still a region 50-200nm where the indentation hardness is dominated by the ideal indenter shape, but which does not fit the Nix-Gao model. Huang et al., improved the fit to experimental data by modifying the Nix-Gao model to include a maximum allowable GND density. This is to represent the fact that repulsive forces between the GND's would tend to force the dislocations to spread beyond the effective stress field of the indenter therefore there must be an upper limit on the GND density [51]. Indentation data must be corrected for pileup/sink in behaviour of the material before it will fit to ISE modelling.

Crystalline materials often show a discrete transition from elastic to plastic deformation at small indentation depths, typically around 100 nm depending on the sharpness of the indenter, this is referred to as the pop-in behaviour. Below the pop-in event the materials show an extraordinarily high hardness, after the pop-in the material deforms elasto–plastically. The initially very high hardness decreases, until at higher indentation depths, a depth-independent hardness is found [52]. The easiest way to avoid indentation size effects is to use deeper indents. However, when working with coated systems it is not

always possible. In this study, where possible, indentations will be made to a number of depths in order to evaluate any ISE.

Surface roughness also influences the results of Nanoindentation experiments causing increased scatter in indentation curves as a results of irregular contact areas [53]. As would be expected the influence of this effect increases with decreasing contact area [54]. Removal of surface roughness effects is usually achieved through careful preparation of the sample being tested. Tensile stress in the indented volume tends to decrease hardness results whilst compressive stress tends to increase recorded hardness due to the magnitude of the shear stresses beneath the indenter relative to an unstressed specimen. This can be important in studies on thin films which tend to have large residual stresses. Assessment of such stresses by Nanoindentation can be difficult as the stress fields change after the instant of initial loading because the material is plastically deformed by the indenter [55]. Models have been developed to determine the stress field under the indenter although these give the best results when residual stresses are assumed to be small relative to the indentation stress field [56]. Stresses can be induced in coated systems as a result of non-uniform heating or differences in thermal expansion of the coating and substrate [57]. Due to the long stabilisation times required for high temperature Nanoindentation most of the stress is expected to relax, however there will still be some residual stresses. The effect of these stresses on results of high temperature Nanoindentation tests may be important to the determination of accurate high temperature hardness values although to date no work has been done to assess their magnitude.

As mentioned above one of the more modern developments in the field of nanoindentation field is the extension of the test technique to elevated temperatures. Early work to determine sample properties at elevated temperatures using depth sensing indentation was strongly influenced by the effect of thermal drift on the depth sensing apparatus used for data collection [58-60]. By thermally stabilising their apparatus, Beake and Smith were able

to obtain elevated temperature hardness and Young's modulus results for a range of bulk materials that gave good agreement with literature values [61].

Given the proven high temperature capability of the instrument used in the Beake and Smith study a similar instrument will be used for the nanoindentation experiments in this thesis. The important feature of apparatus is the orientation of the loading head. The instrument uses horizontal loading so the heated region is not below the depth sensing electronics. In addition to this a conductive shielding is used to remove heat radiated from the sample and indenter from the measurement area [62]. Most commercially available nanoindenters use a vertical loading head and these have been used for elevated temperature indentation characterisation of a range of materials using a heated sample stage [63-65]. The results of these experiments are however affected by the thermal instability of the system due to insufficient thermal stabilisation methods [66]. Elevated temperature mechanical properties have also been evaluated using AFM indentation with a heated sample stage. In one example testing was carried out on polymer coatings up to 130°C. However, the thermal stability of the system was undetermined and no thermal drift correction was made to the data [67].

Thermal equilibration of the sample and instrument must be considered as, if the sample and indenter are not in equilibrium, heat transfer will occur causing rapid thermal expansion which will affect the recorded depth as the contact area increases [68]. Only by maintaining the thermal stability of the system is it possible to record accurate, reproducible results. Schuh et al. [69]proposed a method for attaining thermal equilibrium in which the indenter tip is attached to the Nanoindenter by a shaft made of insulating material. The sample is heated to temperature and the indenter is moved into contact with the sample surface and held there for around 75 minutes to allow the indenter to equilibrate to the indenter temperature. As the indenter shaft is insulating the thermal gradient through the indenter is low and so a steady state is achieved, using this method samples were tested up to 450°C.

This technique has been used successfully for elevated temperature Nanoindentation studies on a range of materials [64, 70-73]. Thermal drift rates on indentations performed using this method are however still high when compared to room temperature measurements leading to a larger degree of uncertainty in results.

An alternative to this technique was presented by Giuliani et al. using nanoindentation to characterise AlN/CrN multilayer coating at 500°C [74]. The sample and indenter are heated to approximately the same temperature, the sample temperature is then fixed and the indenter temperature adjusted until the thermal drift of the system is minimised. This technique was also utilised by Korte and Clegg to achieve thermal equilibrium in their work on micro pillar compression at elevated temperatures [75].

Another technique reported in several sources while using a heated indenter, is to allow a short hold time with the indenter and sample in contact to allow them to thermally stabilise before starting to indent [76, 77]. Using this technique studies have been made on many materials at elevated temperatures ranging from silicon from 25°C-500°C [78] and polymers up to 80°C [79, 80], to superelasticity studies on NiTi at temperatures up to 200°C [81] and the assessment of the properties of the different phases in Al-Ni-Si alloys at 400°C [82]. No attempt is made to manually match the indenter and sample temperatures as in the method presented by Giulianni. This leads to increased thermal drift rates and, although stability is achieved in this way, there is some uncertainty about the actual indentation temperature as there is no way to control the equilibrium temperature reached.

This thermal stability is critical if the technique is to be applied to creep testing. This is because when evaluating nanoindentation data it is extremely difficult to distinguish between time dependent deformations as a result of thermal drift and those as a result of the creep under load of the material being tested.

Another consideration in the determination of high temperature mechanical properties of materials by nanoindentation is temperature-induced expansion of the indenter material. The contact area projection used in nanoindentation analysis relies on accurate calibration of the indenter tip geometry. This is done by determining what is referred to as the indenter area function which calculates a projected contact area for a given indentation depth. At higher temperatures the tip will expand which could lead to changes in the indenter area function. This is not a problem for the bulk of the indenter which, as a self-similar shape, expands linearly and will retain its relative dimensions. However, problems are conceivable at very low depths due to the radius of the indenter tip as this geometry will not expand uniformly leading to changes in the indenter area function. This effect is expected to diminish with increasing indentation depth. By considering the indenter as the superposition of two distinct geometries, the bulk pyramid geometry and the spherical tip [83], it is possible to assess the change in area function as a function of temperature. Using this method it has been shown that the change in area function from room temperature can be at most 0.04% for a diamond indenter with a tip radius of 500nm at 400K [69]. This represents the extreme of tip radius and so in practice the influence of tip expansion on recorded data is minimal.

In many cases high temperature load vs. depth nanoindentation studies have been combined with other nanomechanical test techniques in order to give a more thorough assessment of the samples properties. Fox-Rabinovich et al. have combined high temperature nanoindentation with impact testing, a technique where a solenoid connected to a timed relay is used to produce repetitive probe impacts on the surface in order to find a time to failure for a coating [84]. Also with scratch testing where the indenter is moved laterally across the coating surface with a gradually increasing load in order to determine failure loads for the coating being tested. These techniques and some more traditional testing methods were combined for TiAlN, AlCrN, AlTiN and TiAlCrSiYN coatings in order to assess their suitability for various

machining applications. Results of nanoscratch and impact testing correlated well with end milling and cutting tests carried out using the same samples [85-88].

Beake et al. have also performed testing on TiAlN, AlTiN, TiAlCrN and TiAlCrSiYN producing similar assessments on suitability for various machining applications by combining nano-impact testing, designed to simulate high strain rate contacts, with nanoindentation performed at ambient and elevated temperatures [89, 90]. Packard et al. combined high temperature Nanoindentation with contact mode imaging, using the indenter tip like an AFM probe to create an image of the indent by scanning across the surface. This enabled them to assess the recovery with time of the indentation impressions on a metallic glass sample at temperatures up to $250^{o}C$. The data was used to determine the behaviour of the sample either side of the glass transition temperature [65]. Combining techniques in this way has been used to provide a more thorough description of the samples behaviour giving information more relevant to the intended application.

There are several established methods in place for the extraction of the creep stress exponent and the activation energy from nanoindentation data. These give information about the creep deformation mechanism and the activation energy is the energy required to activate this mechanism respectively. The most commonly used method is the constant load method where the sample is held at maximum load for an extended dwell period and the change in depth is monitored. In order to find the creep characteristics using nanoindentation it is necessary to find the stress and strain at various stages in the dwell period. As the stress field under a Berkovich geometry indenter varies greatly through the affected region a representative stress value is used. This is consistent with principles established in early impression creep work which related the stress to the indentation hardness based on empirical observations [91]. Similarly the strain rate in indentation measurements cannot be described by a single value so a representative rate is used. The

general form of this approximation for a Berkovich indenter was devised by Mayo and Nix, again based on empirical observations [92].

The creep observed in nanoindentation dwell date is assumed to be due to steady state deformation and as such should relate to the standard secondary creep equation. Therefore by determining several values of stress and strain and plotting them on logarithmic axes it is possible to obtain a straight-line plot the gradient of which gives the stress exponent, n. This value can then be used in working lifetime assessments of materials. There are a number of studies which have used to try to evaluate the room temperature creep behaviour of low melting point materials such as solders, although in many cases there is no way to directly compare results with more conventional characterisation techniques. [93-97]

In order to try to validate this technique, in a previous study, room temperature nanoindentation creep tests were performed on 15 materials ranging from Cadmium to Aluminium. This study found that for some materials there was reasonable agreement with literature values of n, however for other materials there was relatively poor correlation. They also found a large degree of deviation in the results obtained from a single sample [98].

The drawbacks in this technique have been attributed to the validity of the assumptions on which it is based. Firstly it is unclear how well the approximations used to represent stress and strain fields giving a single value for calculations, represent the true stress and strain during an indentation test. This is important as for conventional creep tests the stress levels are carefully controlled so, in order to allow comparison more detailed information is needed about the actual stresses. This uncertainty in stress could explain the lack of correlation between experimental nanoindentation creep results and literature values [98].

The variability in measurements on a single sample has been attributed to the influence of primary creep on the recorded data due to the high and

extremely variable strain rates observed which are more indicative of primary creep [97]. The short duration of the nanoindentation creep test also means that new material is constantly entering the stress field beneath the indenter throughout the data collection. It has been suggested that this would lead to a greater input from primary creep. However this has been refuted for materials that have stress exponents greater than 5 since the work of Bower et al. suggests that in this case the stress level is equivalent over the whole of the load supporting area [99].

High temperature nanoindentation studies have previously been used to assess the creep behaviour of materials at a range of temperatures. Most of these nanoindentation creep studies have focused on qualitative comparisons of creep behaviour at different temperatures. These studies have typically looked at differences in creep rates with increasing temperature. In some cases this has been used to evaluate the effect of different heat treatments on material creep behaviour of samples. [100, 101]

Bhakhri and Klassen used a hold a peak load technique up to $550^{o}C$, to compare the activation energies of three aluminium alloys [102] and also the influence of reinforcing particles in aluminium on the activation energy [103]. Similar techniques have been used to assess the creep properties of Au/Sn solder through its effective working temperature range [104]. These studies have been able to distinguish between materials but in both investigations results have not been compared to exponents found by traditional creep determination techniques, instead they report "Nanoindentation creep" exponents.

In order to assess the viability of applying the nanoindentation creep technique to the problem of power station materials work is required to validate the techniques used both to collect data and to analyse the data in order to determine the creep behaviour. The second chapter of this thesis attempts to establish the best methods for obtaining low thermal drift during high temperature nanoindentation measurements in order to ensure that

creep measurements are a true reflection of the material deformation under load.

Chapters three and four are a detailed study of nanoindentation measurements of P91 steel, a material which has been thoroughly characterised using conventional techniques [5, 9, 10, 105, 106]. Data is presented from nanoindentation measurements used to determine both mechanical properties and creep behaviour of parent and weld material. This is used to provide a direct comparison between nanoindentation measurements to more conventional techniques. This comparison is also used to examine the potential effects of time dependent depth changes on nanoindentation data at elevated temperatures and evaluate a new analysis method developed to remove this effect.

In chapter five the study is expanded to determine the properties of P92 steel. This data is again compared to studies using conventional characterisation techniques where possible.   This section also includes a detailed study of the mechanical properties and creep properties of the heat affected zone of a welded section at 675$^{\text{o}}$C.

The appendices contain a careful analysis of the calibration assumptions made for high temperature nanoindentation test. This is done using comparisons of measurements on bulk reference samples to literature results.

Chapter 3 - Experimental methodology

3.1 Nanoindentation hardware

3.1.1 Room Temperature

Nanoindentation experiments were performed using a Micro Materials Ltd. (MML) Nanotest NTX platform 2. One of the unique features of the Nanotest is that the loading head is perpendicular to the instrument frame as shown in Figure 5. Most commercially available indenters use a vertical loading head, the different geometry allows very good thermal stability at elevated temperatures as the control electronics are behind the loading head, left of Figure 5, rather than above the heated area.

In nanoindentation a load is applied to an indenter on the surface of a sample and the displacement into that surface as the load is applied is measured. This data is then analysed to determine the mechanical properties of the sample- unlike conventional hardness and microhardness methods no post indentation imaging is used for the analysis. For the NanoTest™, load is applied using the pendulum assembly in Figure 5. The instrument uses electromagnetic force actuation, at the top of the pendulum is an electromagnet placed next to a permanent magnet. The supply voltage to the electromagnet is increased during loading, pulling the electromagnet towards to the permanent magnet. The assembly pivots around a frictionless hinge moving the indenter at the centre of the pendulum into the sample surface. Varying the applied voltage controls load, the depth change is recorded by monitoring the change in capacitance between the plates located behind the indenter holder. This is done by recording the output from a Wheatstone bridge circuit sensitive to the change in the plate spacing.
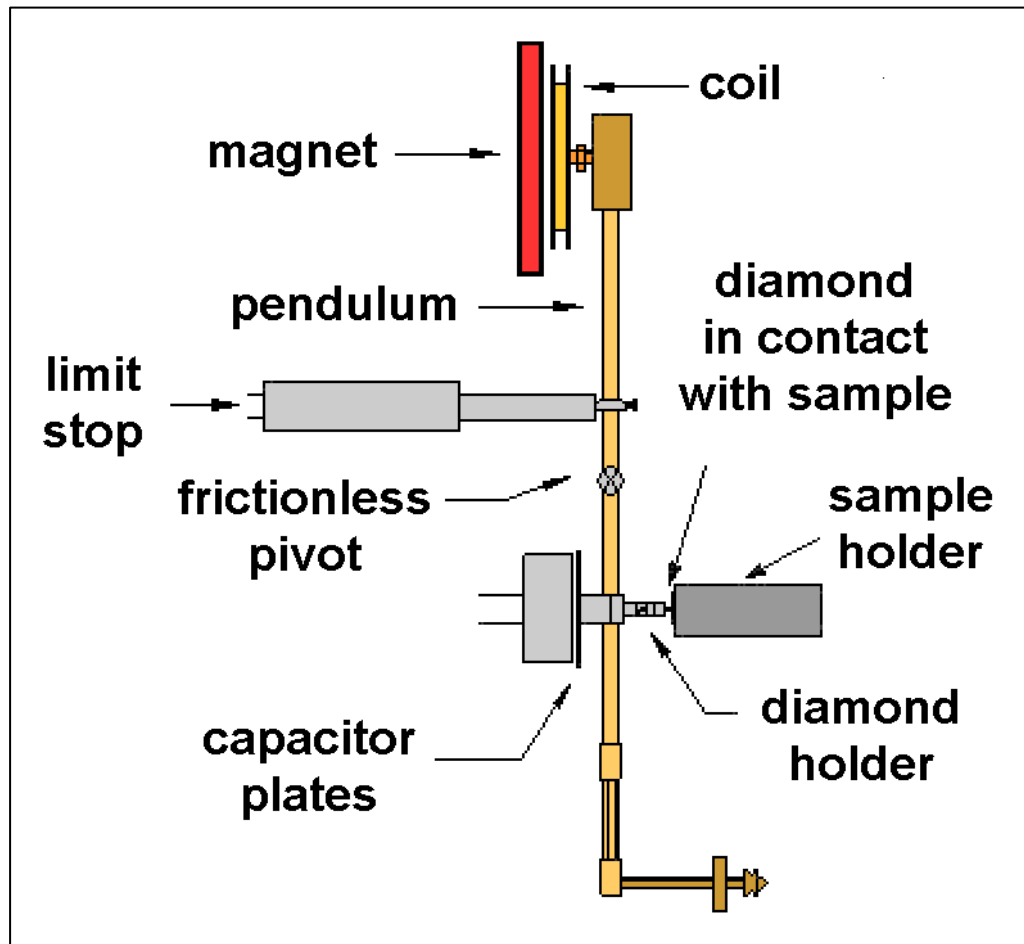
Figure 5: Nanotest Pendulum Design

The Nanotest™ is enclosed in a sealable chamber allowing the internal temperature to be controlled and also allowing experiments to be carried out in an Argon or Nitrogen atmosphere. The chamber was designed for this research project to allow purging for high temperature work on samples expected to oxidise. Nanoindentation results can be heavily affected by the formation of an oxide layer on samples due to the sensitivity of the depth measurement, this is explained in detail in section 3.3.2.

The design of the environmental chamber required careful planning and this constituted the first part of this project. The chamber was made of Perspex

with solid panels chemically bonded in order to minimise the number of mechanical joints. The design consists of a removable box bolted down to a fixed base. A door was cut into the top section to allow access to the NanoTest for changing samples etc. The only mechanical joints were between the base and the main box and around the chamber door. These joints were sealed using O-rings set into the Perspex. The final chamber design is shown in Figure 6. A gas handling system was also developed so that the flow rate of gas into the chamber could be controlled in order to allow rapid purging then careful maintenance of the atmosphere once the purge was complete.

The cabinet temperature was maintained using a tube heater connected to a PID controller, this could maintain the cabinet temperature within $\pm0.1^{o}$C. The importance of stable cabinet temperature will be discussed in section 3.2.1. Standard room temperature indentations were performed using Berkovich geometry synthetic diamond indenters - the Berkovich geometry is used as it is easier to polish a sharp tip than with Vickers geometry indenters [36]. The properties of the indenter were taken as E = 1141GPa and υ = 0.07 for calibration and analysis [107, 108].

Figure 6: Purging Chamber

3.1.2 Elevated Temperature

The pendulum design of the NanoTest™ gives the advantage that, when the hot stage is in use, the heat radiated from the sample and indenter is carried up and therefore away from the depth sensing hardware. This allows experiments to be performed at a maximum test temperature of 750°C. A schematic of the hardware used to perform high temperature experiments is shown in Figure 7. The high temperature assembly consists of both a heated indenter and sample stage. To aid the heat transfer away from the sensitive

hardware, a heat shield is placed behind the indenter as shown in the figure. At higher temperatures the shield can be water cooled to give additional protection. This was used when testing at temperatures in excess of 450°C. On the heated sample stage samples are mounted on an Aluminium nitride tile - the tile ensures that the samples are heated evenly across the contacting area.

The indenter and sample are heated using resistance heaters controlled by separate automated proportional–integral–derivative (PID) controllers. This means that the power supply to the heaters can be ramped up in a controlled way to avoid damage to the heating filaments whilst approaching the target temperature. Similarly, when returning to ambient temperatures the PID controller is used to cool the heaters at a constant rate to avoid thermally shocking the filaments. The PID settings are tuned once the system has reached the target to find optimum values for maintaining the required temperature. In addition to the thermocouples shown in Figure 7, in experiments reported in this thesis a thermocouple was attached to the sample surface using high temperature cement. This was used to compare the actual surface temperature to the target temperature on the control unit. It was observed that due to the temperature gradient through the heated sample stage there was a significant difference between the target temperature and the true surface temperature, up to 80°C difference at 650°C target temperature.

Initially attempts were made to solve the problem by using the surface thermocouple as the reference thermocouple for the PID controller. However it was found that in this set up the heater was too far from the control thermocouple, meaning that the sample heater could not stabilise accurately at the desired test temperature. Instead the surface thermocouple was used as a reference and the target temperature for the internal thermocouple adjusted until the surface thermocouple measured the desired test temperature.
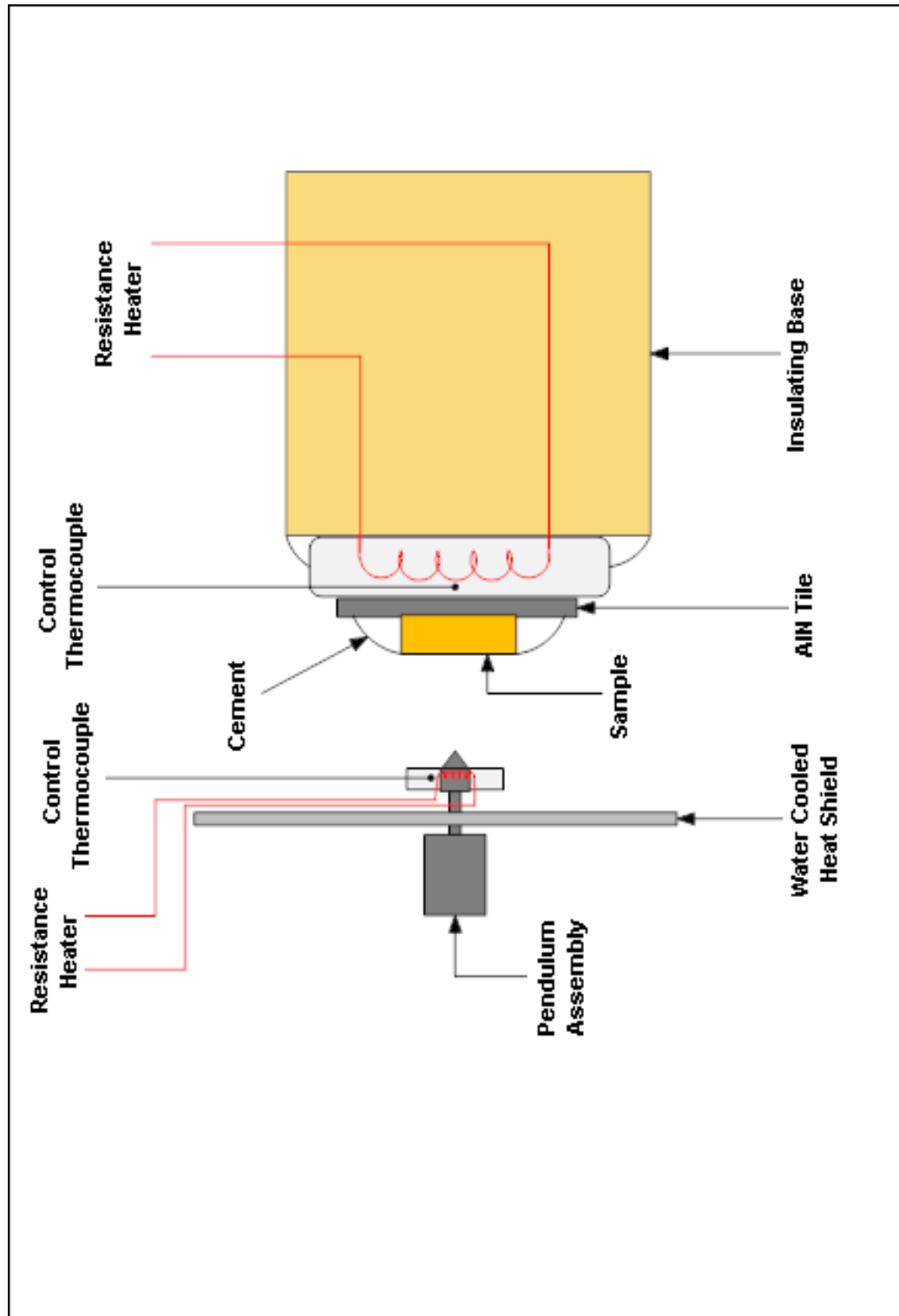
Figure 7: NanoTest heating hardware

Experimental Methodology

The use of a PID controlled heater in the indenter and stage, although the best solution for stable heating, was found to cause problems once the indenter and sample were brought into contact. Small differences in the indenter and sample temperature lead to heat transfer between the two bodies as they attempt to thermally stabilise. The PID controls then respond to correct the temperature change, this leads to another temperature difference and further heat transfer which again the PID controllers attempt to correct. The effect of this is observed in the depth signal as an oscillation caused by the continual expansion then contraction of the indenter as its temperature changes, see Figure 8. This is to be expected as the indenter has a much lower thermal mass than the sample and so responds more rapidly to temperature changes.

The effect was minimised by locking the power supply to the indenter so that only the sample was PID controlled. This proved to be successful completely removing the oscillation from the signal in samples tested subsequently. The success is demonstrated in Figure 8 with typical indents from experiments performed at 600°C on fused silica both with and without a power controlled indenter. This technique was developed in collaboration with Micro Materials and the power control method was incorporated into the NanoTest software so that the power to the indenter heater is automatically locked once the target temperature has been reached.
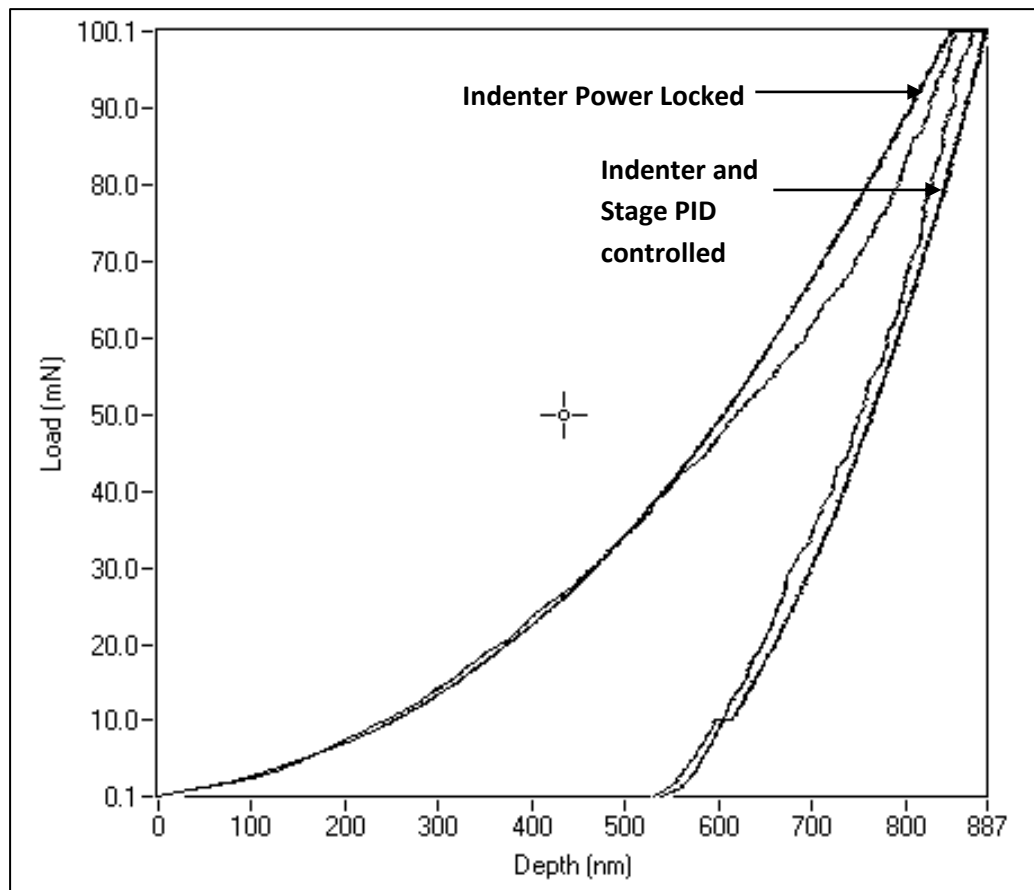
Figure 8: 600°C Indents on Fused Silica demonstrating the effect of power control

Samples were attached to the stage using OMEGABOND® 600 high temperature cement (Omega Engineering Ltd., UK). Other high temperature cements were tried but were found unsuitable due to evidence that they denatured at higher temperatures and were deposited on both the sample and indenter. Figure 9 is a SEM image of one of the high temperature indenters after testing using one of the alternative cements as a sample adhesive.

It is clear that material has been deposited at the tip of the indenter and is also on all three of the faces. Examination of the EDX spectrum of the deposited material showed it had the same composition as the cement with large peaks for silicon, magnesium and sodium. This result is shown in Figure 10, the indenter was coated with a thin platinum to improve the conductivity

of the surface for SEM imaging. No such deposits were found when using OMEGABOND®600.
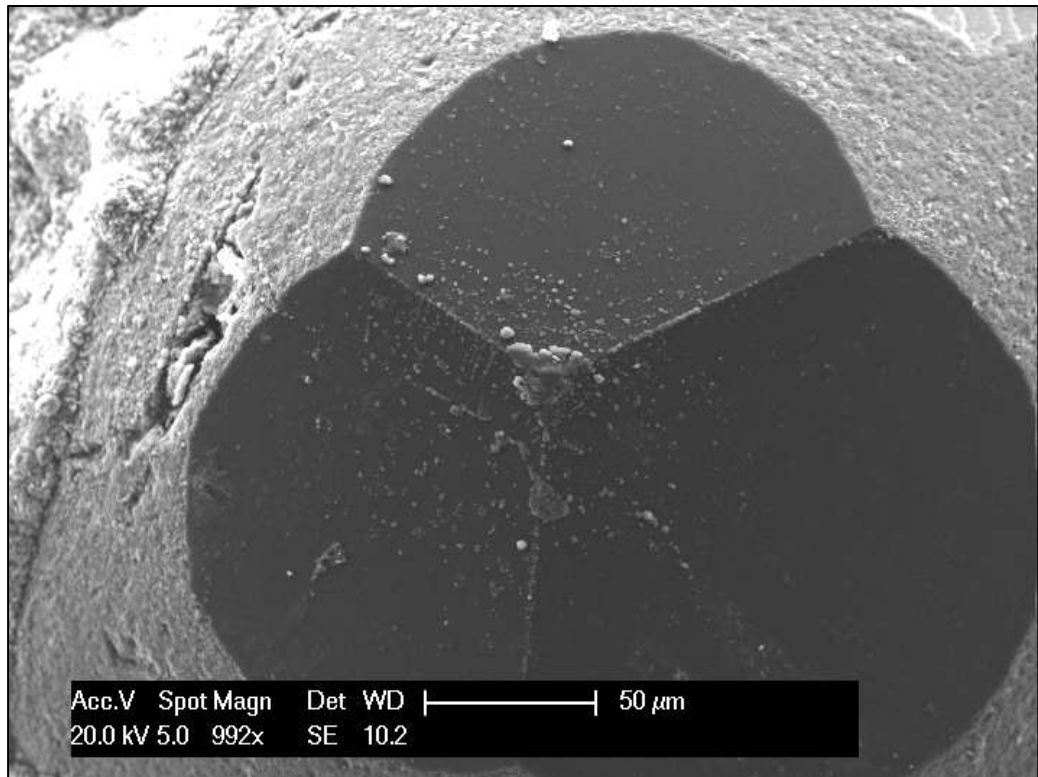
Figure 9: Evidence of cement deposited on indenter at elevated temperature
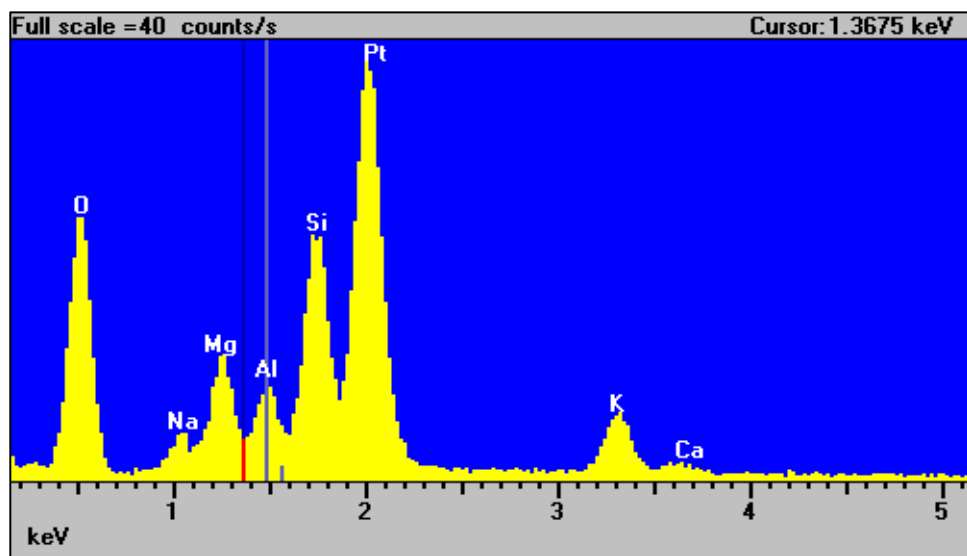
Figure 10: EDX spectrum of cement deposit

Experimental Methodology

Like room temperature tests, standard high temperature experiments are performed using Berkovich geometry indenters. However, at temperatures above 450°C diamond starts to oxidise. To avoid this, cubic Boron Nitride (cBN) indenters were used whenever testing above 450°C was performed. Table 1 shows a comparison of the mechanical and thermal properties of diamond and cBN at room temperature. At room temperature there is little difference between the two indenter materials

Table 1: Comparison of diamond and cBN mechanical and thermal properties

	Diamond	cBN
Young's Modulus (GPa)	1141	909*
Poisson's ratio	0.07	0.121
Thermal conductivity (Wm^{-1}K^{-1})	1600 [109]	1300 [109, 110]

* Theoretical ideal value

As the testing temperature is increased, the properties of the indenter change. In order to get correct Young's modulus values for the sample it is necessary to know the change in the Young's modulus of the indenter. For diamond the change is very small ~1.5% drop in modulus from 25°C to 500°C. cBN Young's modulus drops by ~3% over the same temperature range and ~4% when the test temperature is increased to the hardware maximum 750°C[107]. In order to ensure the greatest degree of accuracy in reported sample Young's modulus values, the indenter moduli used were those relevant to the test temperature. For these calculations the Poisson's ratio of the indenter was assumed to be the same at all temperatures.

29

3.2 Hardness and Young's Modulus determination

Exact experimental parameters varied between the different samples tested and these will be discussed as needed in the appropriate sections. This section is intended to provide an overview of how those parameters were selected and optimised.

All the experiments performed for this thesis used load controlled indentation. With the indenter in contact with the sample surface, the load on the indenter was increased gradually at a constant rate until the target load was reached. There was then a pause with the load held constant to allow any viscous deformation to relax before unloading, the duration of this pause is material dependent and was determined by preliminary experiments. At the end of the pause the load was removed from the sample, again at a rate set in the software, until at approximately 10% of the maximum load, unloading was paused for the thermal drift data collection.

3.2.1 Thermal Drift Correction

As the displacements measured in nanoindentation experiments are so small they can easily be affected by thermal fluctuations in the depth sensing hardware. As previously mentioned, in order to ensure the thermal stability of the system the hardware is contained in a temperature controlled chamber. However due to the sensitivity of the depth sensing capacitor it is still neccesary to monitor the thermal drift of the system. Typically this is done by pausing the load ramp during unloading and collecting depth data with the load held constant for a short duration, usually 60s at room temperature. The first 40% of the collected data is removed from the analysis so that viscoelastic recovery effects do not influnce the thermal drift correction. The remaining data is plotted depth vs. time and the gradient of this data is used as the thermal drift correction made to that set of indentation. Each nanoindentation made has its own thermal drift correction which is applied automatically by the analysis software. For certain samples it is not

appropriate to make thermal drift corrections in this way, this is discussed in detail along side the results in the relevant sections. An example of a room temperature thermal drift measurement of fused silica is shown in Figure 11, the thermal drift correction in this case was -0.0481nm/s.
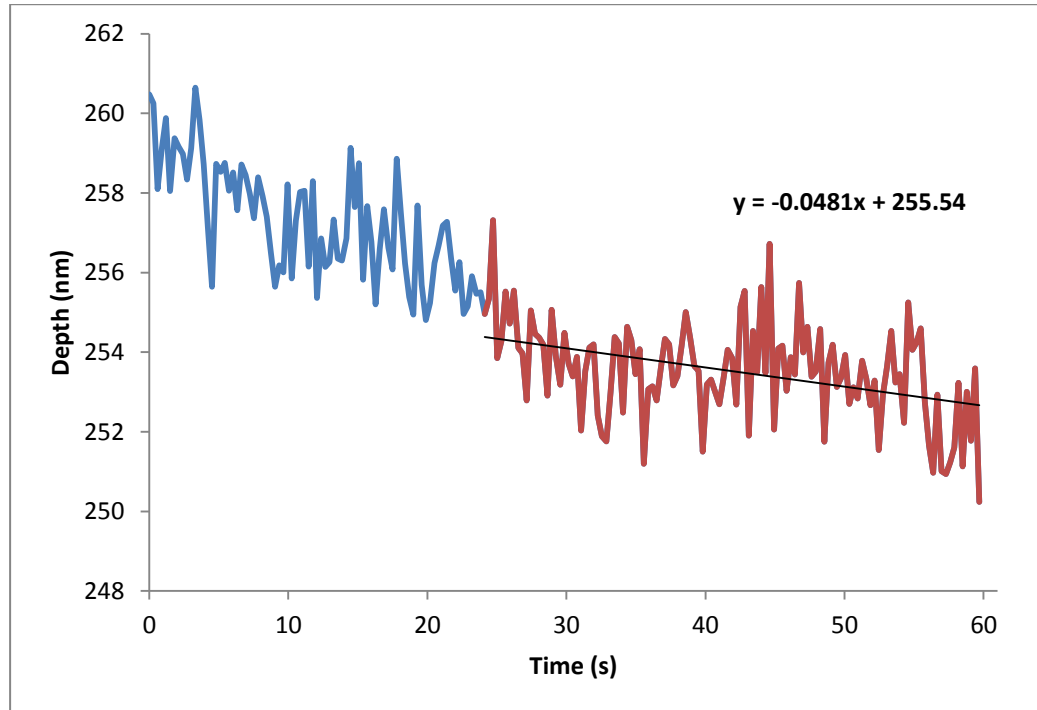
Figure 11: Typical thermal drift correction data

For materials at high temperature longer thermal drift data collections are used, typically 120s, as most samples show a greater degree of viscoelastic recovery. The effect of using insufficient data collection periods is shown in Figure 12. Both plots (a and b) show a 120s thermal drift data collection period from an experiment on fused silica at $600^{o}C$. In plot a) the thermal drift correction has been made using only the first 60s of the data. In plot b) the correction has been made using data collected over the full 120s, in both cases the first 40% of the data has been removed as stated above. The correction data is indicated in a) and b) with crosses. From the data it is clear that a 60s drift correction collection period is not sufficient as the sample is still recovering. As a result the thermal drift correction calculated in a) is -0.29nm/s compared to the data in b) which gives a correction of 0.01nm/s.
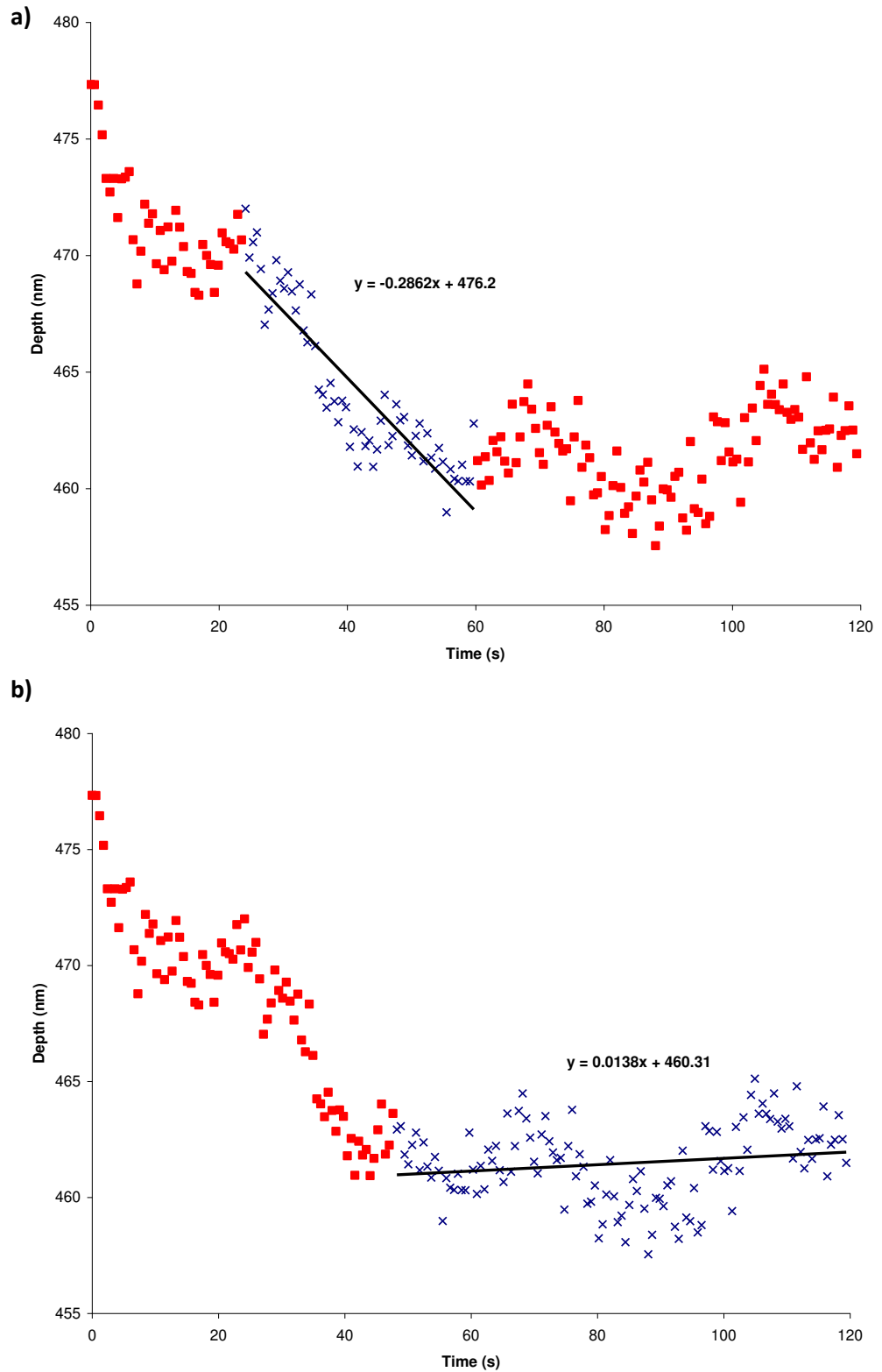
Figure 12: Thermal drift collection plots a) for 60s data collection b) for 120s data collection on fused silica at 600°C

3.2.2 Dwell at Peak Load

In nanoindentation, the creep or visco-elastic characteristics of the material must also be considered. Visco-elastic behaviour is driven by the applied load but for most materials at lower temperatures it diminishes after a few seconds to a stable rate. The magnitude is dependent on material and influences maximum depth and initial unloading data. This is critical as the initial unloading data is used in determining the contact stiffness for the indentation, therefore loading time and hold period at maximum load can influence hardness and modulus measurements. The technique used to correct this effect was publicised by Chudoba and Richter [111]. A dwell period at peak load was used to allow any visco-elastic depth change to stabilise before unloading, this technique has been shown to improve the correlation of measured material properties to those determined using other methods. The dwell period data is corrected for thermal drift to eliminate any effect of thermal instability on the data.

3.2.3 Data Analysis

Data reported in this thesis was analysed using the techniques popularised by Oliver and Pharr [112]. The starting point for the analysis is Sneddon's relationship for a conical tip shape indenting on a plane surface [113]. Sneddon's relations assume a rigid indenter. Oliver and Pharr account for a non-rigid indenter by considering the reduced modulus. This is the combined response determined by the Young's modulus of both the indenter and the sample, which is given by Equation 2, where E_r is the reduced modulus and E, ν and E_i, ν_i are the Young's modulus and Poisson's ratio of the sample and indenter respectively.

$$\frac{1}{E_r} = \frac{(1 - v^2)}{E} + \frac{(1 - v_i^2)}{E_i}$$

Equation 2

The reduced modulus is determined from the experimental data by measuring the sample stiffness. Stiffness is calculated from a least squares power law fit to the unloading data on the load-depth plot. The form of the power law fit is shown in Equation 3, where h_f is the final indentation depth after unloading and α and m are fitting constants dependent on the material being tested. The power law fit can then be differentiated with respect to h to find the stiffness S as shown in Equation 4.

$$P = \alpha \left(h - h_f \right)^m$$

Equation 3

$$S = \frac{dP}{dh}$$

Equation 4

Once the contact stiffness is known it can be related to the reduced modulus as shown in Equation 5. This equation also uses the contact area of the indentation, A. The contact area is the projected area of the elastic contact between the indenter and sample during unloading. It is calculated from the contact depth and the indenter area function. The contact depth is taken to be the difference between depth at maximum load, h and the surface displacement at the edge of the contact h_s as shown in Figure 13. h_f is the final depth after the load is removed and h_c is the contact depth.

$$E_r = \frac{\sqrt{\pi}}{2\beta} \frac{S}{\sqrt{A}}$$
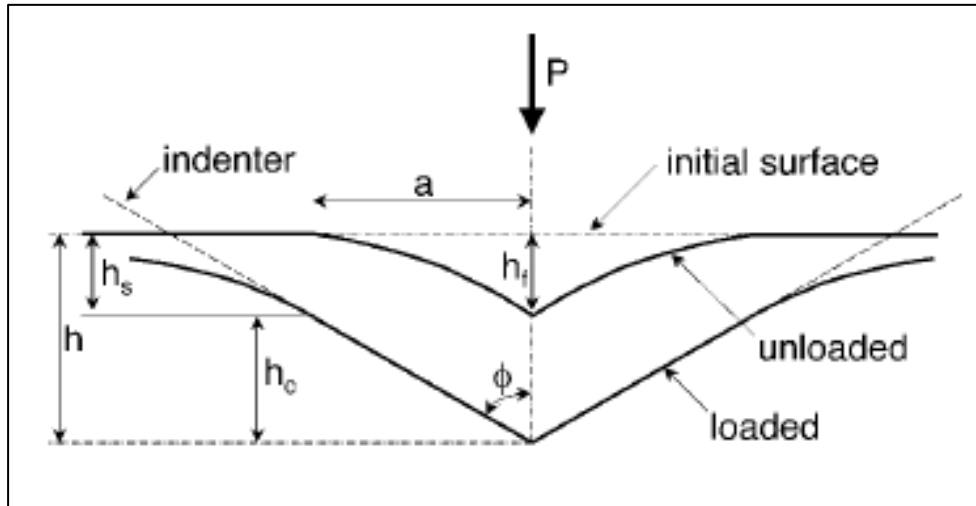
EE   **Equation 5**

Figure 13: Indenter contact schematic [112]

In practice the contact depth is found using Equation 6, where P_{max} is the maximum applied load, h_{max} is the depth at maximum load and ε is a constant dependent on the indenter geometry, ϵ is taken as 0.75 for Berkovich geometry indenters. Using the contact depth this gives a better contact area estimate for determining the hardness and modulus than the maximum or final depth as it has been shown to be a closer to the true load supporting contact area [46]. The area function of the indenter must be accurately determined to allow accurate analysis, the technique used to calibrate indenter area function is detailed in Appendix I.

$$h_c = h_{max} - \epsilon \left(\frac{P_{max}}{S} \right)$$

Equation 6

One additional consideration in the calculation of the reduced modulus is the load frame compliance. Failure to remove frame compliance can make indentation hysteresis curves appear more linear as shown in Figure 14.

In order to correct for the frame compliance, the instrument and sample are considered as two springs in series, the compliance of the sample is the inverse of the contact stiffness so the total compliance, C, is given by Equation 7.

$$C = C_f + \frac{\sqrt{\pi}}{2E_r}\frac{1}{\sqrt{A}}$$

Equation 7

Again A, is contact area and E_r is the reduced modulus, C_f is the frame compliance which is calibrated as detailed in Appendix I. Working back from Equation 7 it is possible to find the reduced modulus with the frame compliance removed.
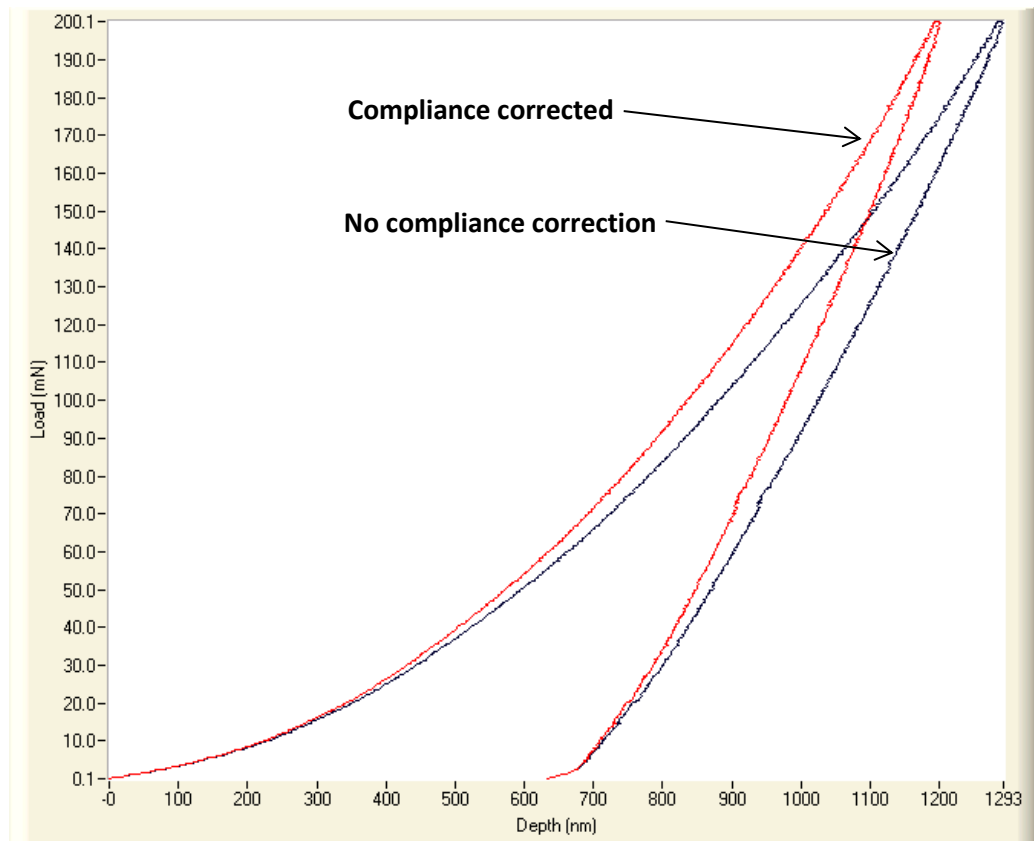
Figure 14: Compliance correction example

$$H = \frac{P_{max}}{A}$$

Equation 8

Once the contact area has been calculated it is also possible to determine the hardness of the sample from Equation 8. The hardness is simply the peak load divided by the contact area.

3.3 High Temperature Nanoindentation Methods

3.3.1 Thermal Stability

The thermal stability of the nanoindenter hardware is of key importance in obtaining reliable and reproducible high temperature data. In order to ensure system stability at the target temperature the nanoindenter is left to reach thermal equilibrium prior to beginning experiments. This is done by allowing the system to rest for one hour for every 100°C above room temperature once the target temperature has been reached. The delay is necessary as it allows the hardware to reach an equilibrium state with the additional heat source provided by the sample and indenter. At higher temperatures it is necessary to increase the target temperature of the cabinet temperature controller as the additional heat sources raise the overall chamber temperature by a few degrees.

Figure 16 shows temperature data gathered using k-type thermocouples attached to the depth sensor capacitor plates during a ramp to 600°C. As depth changes are determined from changes in the plate spacing the thermal stability of these plates is directly linked to the thermal stability of the measurements. It is clear from the recorded data that even the plate closest to the heated region the "bottom plate" reaches a reasonably stable temperature almost instantaneously once the target temperature is reached. During the first few hours after the target is reached the deviation in the

temperature is > ±0.5 ^{o}C over a 10 minute period. By the end of the 6 hour period this has fallen to > ±0.1 ^{o}C, in line with the thermal control achieved using the cabinet temperature controller.

The stage encoder depth calibration can be used as a tool to assess system stability. In a normal depth calibration the points are randomly distributed as in Figure 15a. If the system is still drifting, the calibration will display a noticeable trend due to the systematic change in capacitor plate spacing as in the Figure 15b.
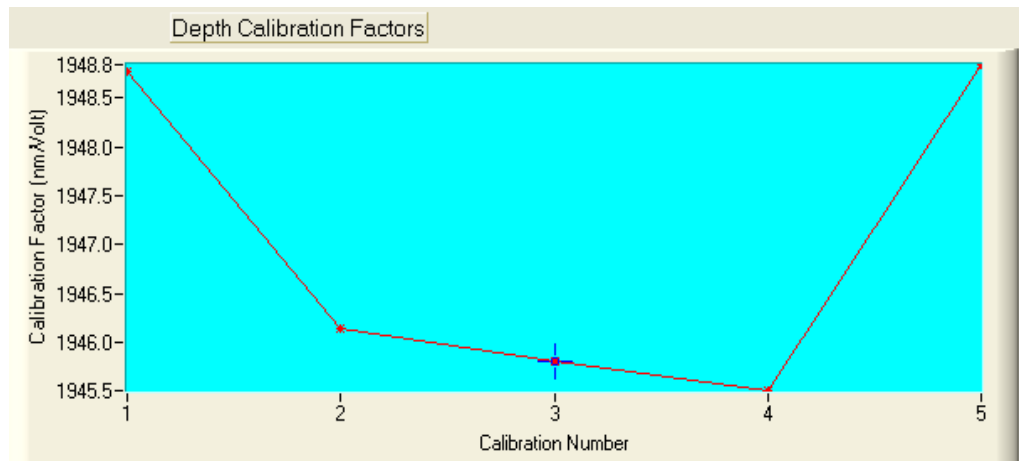
(a)
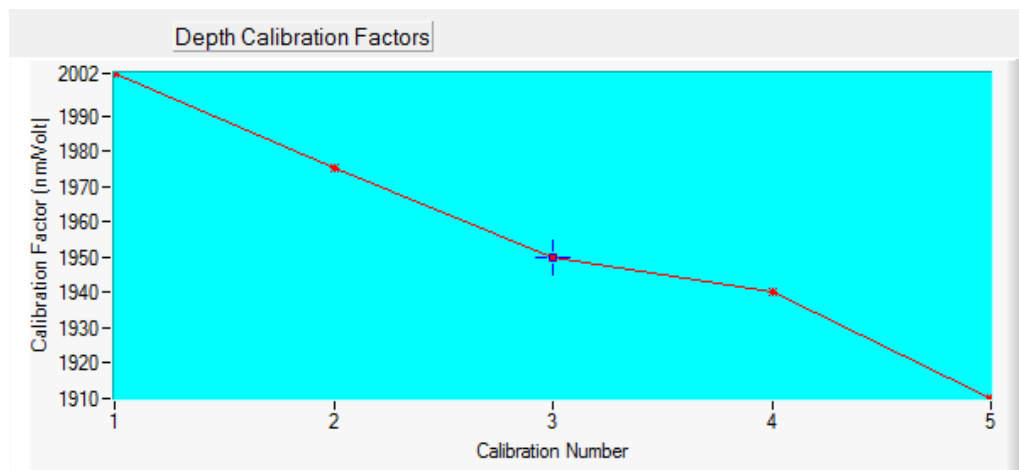
(b)

Figure 15: Depth Calibrations (a) Normal calibration (b) Calibration affected by thermal drift
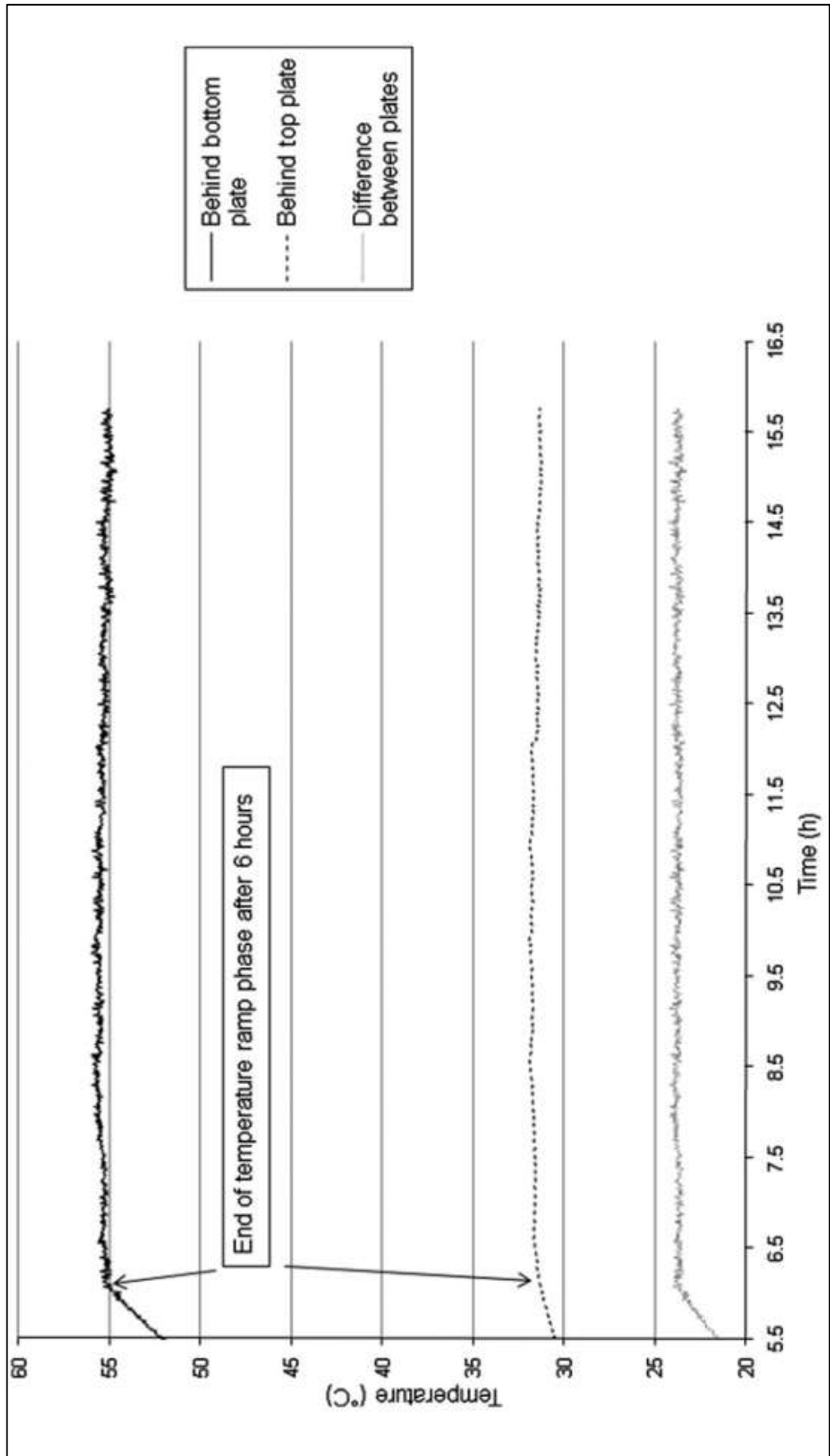
Figure 16: Thermal stabilisation of capacitor plates

Experimental Methodology

Once the system is stable, it is important to ensure that the sample and indenter are in thermal equilibrium before starting to indent. The first technique, proposed by Schuh et al. involves use of an unheated indenter [69]. The sample is heated to the target temperature and the system is allowed to stabilise. The indenter is then brought into contact with the sample and the left in that position until the system has once again stabilised. I.e. until the indenter and sample have reached some equilibrium temperature. This is determined by monitoring the drift of the output signal from the capacitance bridge. Tests are then performed one at a time. The indenter is kept in contact with the sample with a load of 0.03mN whilst moving between indentation positions in order to maintain the thermal link. At each new indentation location the indenter is left to stabilise for 15 minutes before making the indentation.

The second involves using both a heated sample and indenter. Although the sample and indenter are set to the same target temperature using the PID control, small differences between their temperatures can lead to heat transfer during the indentation cycle. This leads to higher thermal drift acting on the recorded data. In order to minimise the thermal drift a technique was used which has been adapted from the one presented by Korte and Clegg [75].

The indenter and sample are heated to the same temperature and the power on the indenter side is locked to remove any PID loop conflict effects. Once the system has been allowed to stabilise three indents are made on the sample and the average thermal drift rate recorded once more. The indenter temperature is then dropped by $10^{o}C$, the power is locked and the system left to stabilise for 15 minutes. Three more indents are then performed and the average thermal drift rate recorded.

The drift rate increases as the temperature difference between the indenter and stage increases. So the average drift rates are compared to assess

whether the indenter temperature is being correctly altered. The indenter temperature is then increased or decreased as necessary in 10°C increments until the drift rate is found to increase. At this point the temperature is changed by 5°C in the opposite direction and after stabilisation the drift assessed. The indenter temperature is then altered by ever decreasing steps to iteratively find the temperature corresponding to the minimum thermal drift. The indenter is held in contact with the sample at a 0.03mN load for 60 seconds prior to the start of each indentation; this allows any minor thermal stabilisation of the two bodies.

In order to establish which technique gave the greater thermal stability two samples were tested. Experiments were carried out on a standard fused silica reference sample at 300°C and 600°C. This was selected as an example of a readily available insulating sample. The other sample, selected for its high thermal conductivity, was gold. The gold sample was tested at 300°C only, as at higher temperatures there was a risk that creep effects would influence the recorded hardness and Young's modulus. The gold was taken from a jeweller's 24 carat sample (99.99% purity), it was polished to a mirror finish then annealed at 400°C for four hours to relax any residual stresses in the surface and also allow grain growth. This was done to prevent additional grain growth during high temperature experiments which may have affected results.

The high temperature methods used were as outlined in the methodology, section 3.1, with the exception that at this time surface thermocouples were not used so there is some uncertainty around the precise test temperature. The Fused Silica was tested at maximum loads of 10mN and 100mN at all test temperatures and using both methods, a loading time of 20s and unloading time of 10s was used in all experiments. At room temperature and 300°C a thermal drift correction data collection period of 60s was used. At 600°C this was increased to 120s as a longer period of visco-elastic recovery was observed and this needed to be removed from the correction data as outlined in section 3.2.1. Similarly at room temperature and 300°C, a 5s dwell at peak

load was sufficient to allow any loading rate dependent visco-elastic deformation to relax but at 600°C a 10s period was required.

Experiments on gold were performed at 10mN maximum load, again 20s loading and 10s unloading periods were used. Faster unloading rates were used to minimise any time dependent effects [114]. At room temperature a 60s thermal drift correction period was used, this was increased to 120s at 300°C due to increased creep recovery behaviour. At both test temperatures a 30s dwell period was sufficient to allow creep recovery before unloading.

Thermal drift data from the tests was monitored as this was taken as an indication of the overall system stability. Table 2 shows the thermal drift data from both samples at room temperature, 90% of the data has thermal drift below 0.15nm/s. This value was selected as the bench mark for acceptable levels of thermal drift as ideally the system would experience the same drift at elevated temperatures as at room temperature.

Table 2: Room Temperature thermal drift data

Sample	Test Temperature °C	Max. Load mN	% Indentations with drift		
			<0.15 nm/s	< 0.10 nm/s	<0.05 nm/s
FS	20	50-100	100	95	75
Au	20	10	90	20	0

Table 3 shows the thermal drift calculated from data collected using the heated indenter method. Using this technique 65-80% of the data from the two samples had drift rates below 0.15nm/s. Even at 600°C, 65% of the fused silica data has drift rates below 0.15nm\s.

Table 3: Heated Indenter thermal drift correction data

Sample	Test Temperature °C	Max. Load mN	% Indentations with drift		
			<0.15 nm/s	< 0.10 nm/s	<0.05 nm/s
FS	300	10	65	40	20
	300	100	-	-	-
	600	100	67	47	27
Au	300	10	80	80	60

Using the unheated indenter contact method, initially results appeared the same as for the heated indenter technique. ~65% of the 10mN indentations on fused silica at 300°C had drift rates below 0.15nm/s as shown in Table 4. However at higher indentation depths the thermal drift is much higher with no indentations below 0.15nm/s and an average drift rate of 0.22nm\s. Similarly experiments performed on the gold sample had extremely high drift rates with an average of 1.5nm/s.

Table 4: Unheated indenter thermal drift correction data

Sample	Test Temperature °C	Max. load MN	% Indentations with drift		
			<0.15 nm/s	< 0.10 nm/s	<0.05 nm/s
FS	300	10	63	31	13
		100	0	Average drift rate 0.22 nm/s	
Au	300	1-100	Average drift rates ≥1.5 nm/s		

In the case of the gold data using the unheated indenter method the thermal drift rate was so high that it had a noticeable effect on the standard load vs

depth indentation plots as shown in Figure 17. It is clear from the plots that the gold data is heavily affected by thermal drift with the effect worsening as the indentation depth increases.
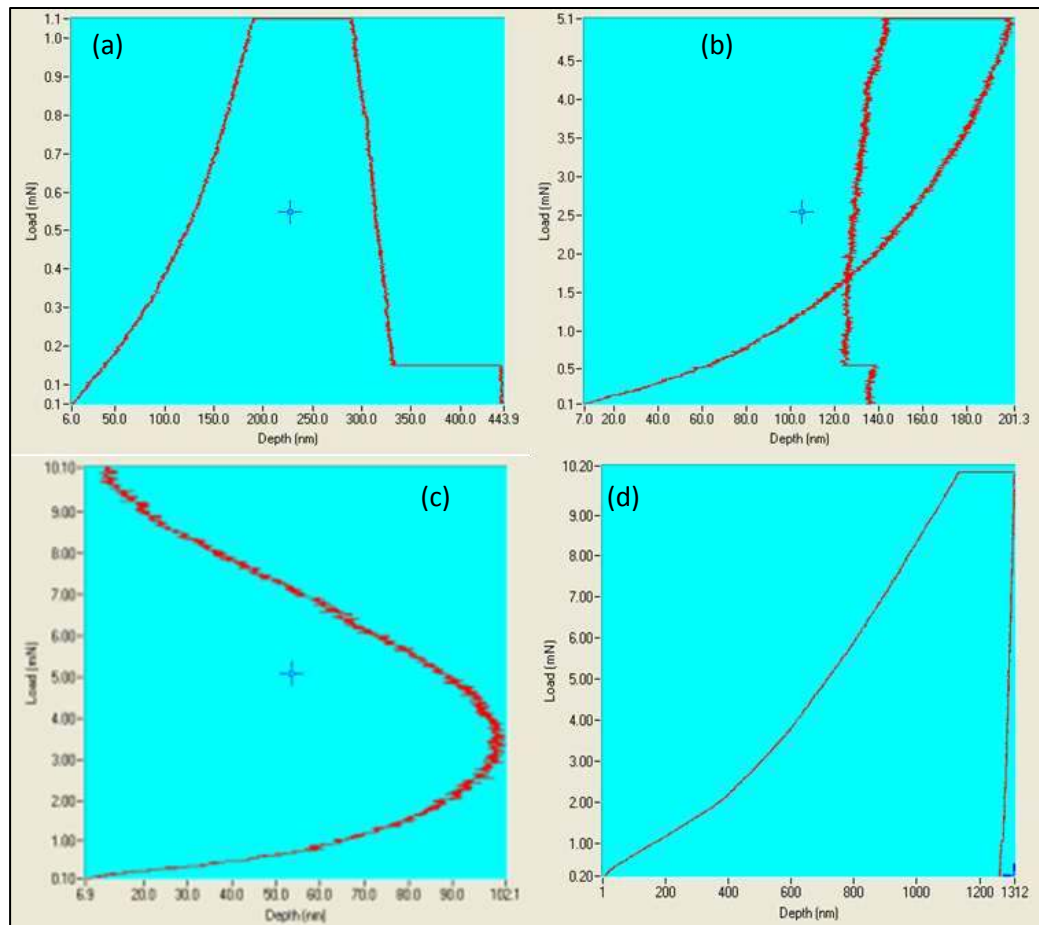
Figure 17: Gold curves with an unheated indenter (a) 1mN load, (b) 5mN load, (c) 10mN load, (d) representative 10mN indentation using heated indenter.

An explanation of these results was provided by a model of the thermal contact constructed by Dr Smith of Micro. Materials. Full details of the thermal model are presented in the journal paper by Everitt, Davies and Smith [115], presented here is an overview of the pertinent results from the model. The model suggests then when the unheated indenter is brought into contact with the heated sample, thermal equilibrium is quickly reached. The indenter does not however reach the same temperature as the heated body instead forming a localised thermally stable region at the point of contact at a lower temperature than the bulk of the sample. The result of this is a temperature

44

gradient between the main body of the sample and the region directly in contact with the indenter.

The indenter and sample are represented schematically in Figure 18 which shows the samples at a variety of temperatures being indented from the top down. In the insulating fused silica sample the temperature gradient is quite shallow as demonstrated in Figure 18 (a) and (c). As a result it would be possible for the indenter to move quite a distance before it encountered a significantly different temperature leading to instability. This would explain why it is possible to obtain results from this sample comparable with those obtained using the heated indenter method. It also explains why the higher load indentations exhibit much higher thermal drift rates as these reached far greater depths than the 10mN indentations.

In gold the temperature gradient is much steeper, as shown in Figure 18(b). The result of this is that as soon as the indenter starts to move it encounters significant temperature changes leading to thermal instability in the system and higher drift rates. The larger the change in depth the larger the temperature change encountered. This is supported by the experimental data, which showed increasing thermal drift with increased load (see Table 4).

Due to the unsuitability of the indenter contact method for higher test temperatures and conductive samples, the heated indenter method was adopted as the technique used for the other results presented in this thesis. Whilst adjusting the indenter temperature for the heated indenter method it was noted that there was a significant discrepancy between the test temperature entered into PID controller and the stable indenter temperature, see Figure 19 below. This was found to be due to the thermal gradient through the sample heater leading to a lower surface temperature. Following on from this investigation, all further high temperature work was performed using the heated indenter method outlined in the methodology with the

addition of surface thermocouples to ensure the accuracy of the test temperature.
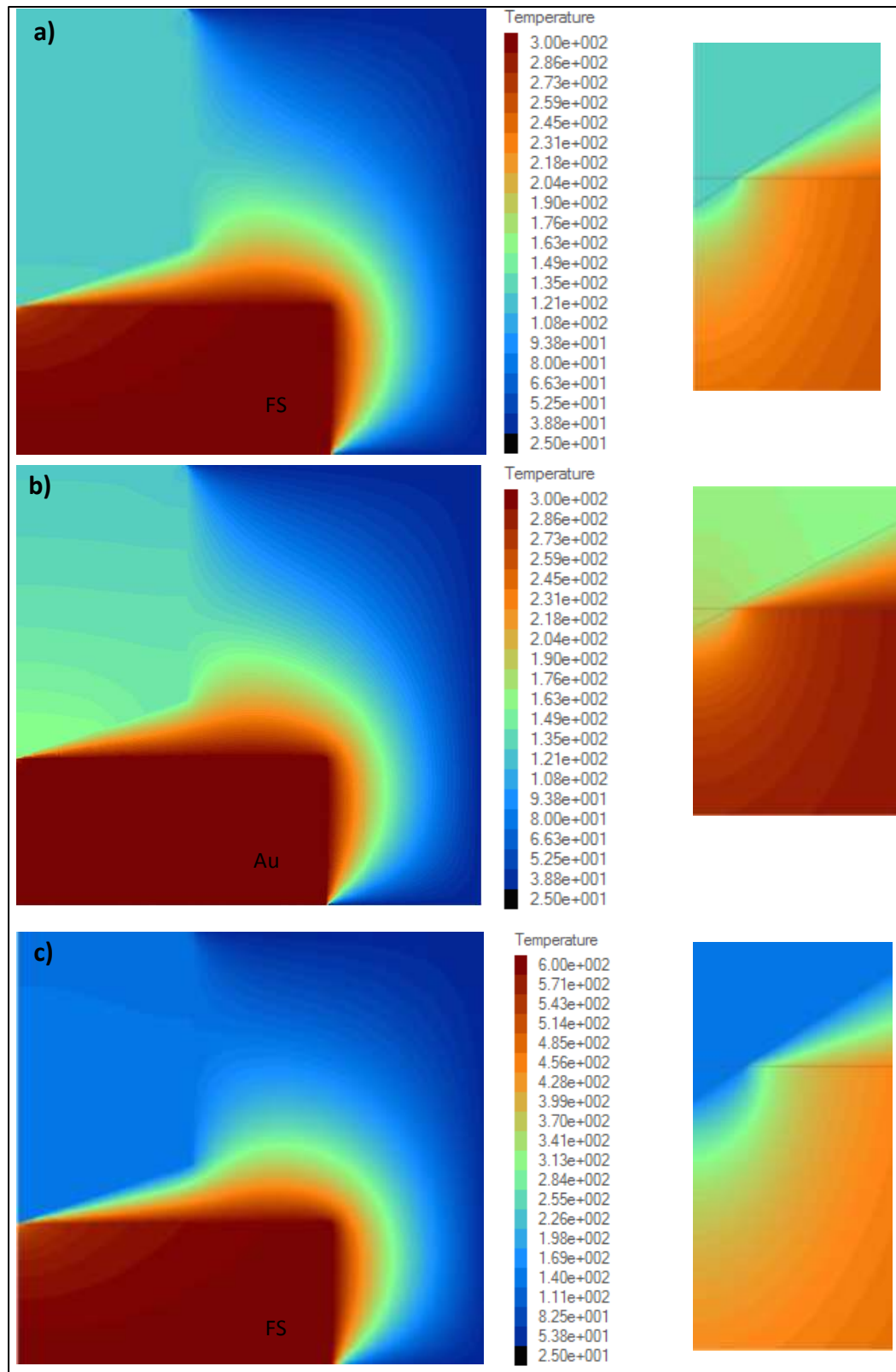
Figure 18: FEA thermal model results a) FS 300°C b) Au 300°C c) FS 600°C
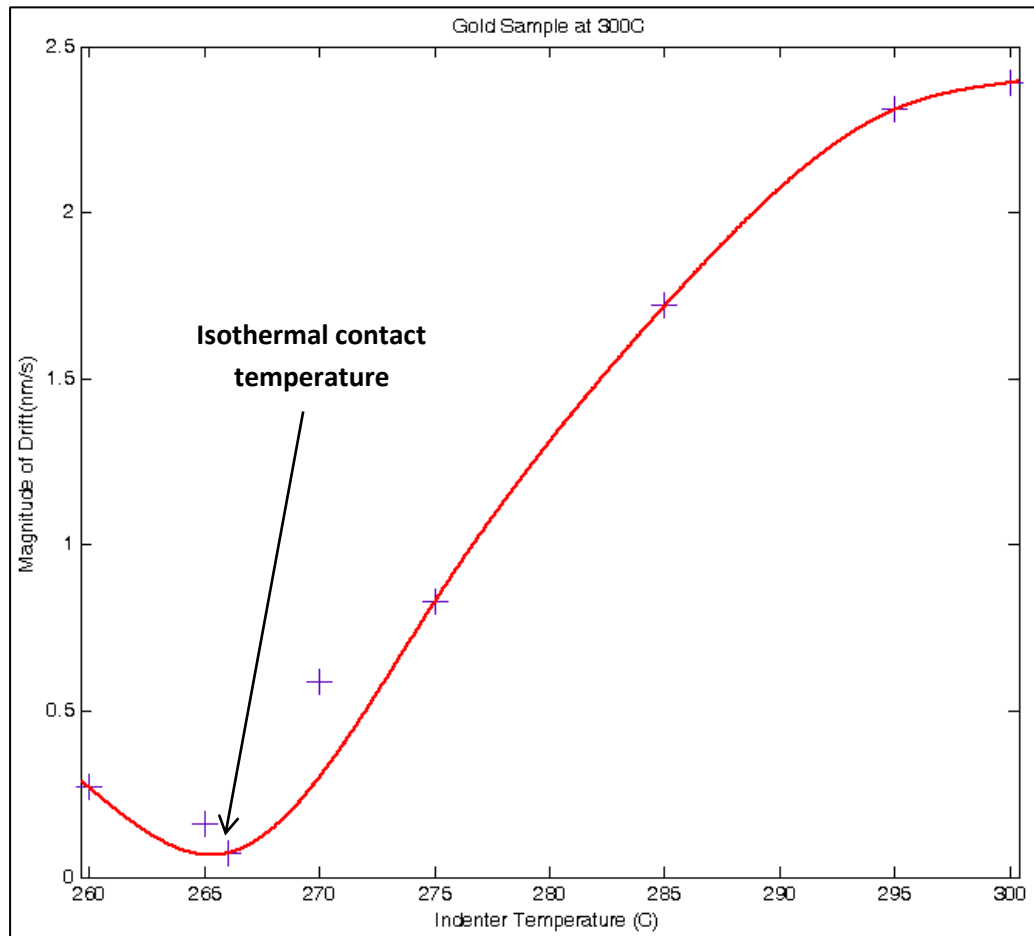
Figure 19: Indenter temperature stabilisation for Stage 300°C temperature

3.3.2 Argon Purging

As mentioned in section 3.1.1 the NanoTest was housed in a sealable chamber that could be purged to allow testing to be done in a low oxygen atmosphere. The gas system consists of a flow controller and a bypass, this enables the user to bypass the flow controller when filling the chamber to reduce purging time. The flow controller can then be employed to provide a low level throughput of gas to maintain the atmosphere in the chamber without disrupting experiments. It was decided to use argon gas in preference to nitrogen due to the potential for nitride formation on the surface of some samples during high temperature experiments. Experiments were performed to determine whether it was possible to achieve the required oxygen level in

the chamber, the oxygen level was monitored using a QRAE II oxygen monitor. By using the gas handling system it was possible to get oxygen levels below 0.01% of the volume of the chamber, this was the limit of the precision of the oxygen monitor and was the target.

Testing was performed on a standard fused silica reference sample in order to confirm that purging had no effect on the nanoindenter hardware. Tests were carried out at room temperature using a range of loads in an argon atmosphere. Results were found to be no different from those determined under standard test conditions.

Even though the chamber is designed to slow the rate of oxidation of samples, the time needed for the system to stabilise at higher temperatures means that in many cases a thin   layer has formed before experiments can begin. To minimise the influence of the oxide layer, a technique has been developed to move through the oxide before the experiment begins. This is done by increasing the initial load in the Nanotest experimental software. The initial load is the small force applied to hold the indenter on the sample surface prior to the start of experiments. By increasing this load, the indenter is forced through the oxide layer to the surface of the sample before data collection begins. An example of the effect of oxidation on the indentation is shown in Figure 20. This data is taken from tests on performed on a TiCN coating at 500°C, a thick oxide layer formed on the surfaced after several hours at temperature. Increasing the initial load extended the test window allowing more data to be collected before the oxide layer became too thick.
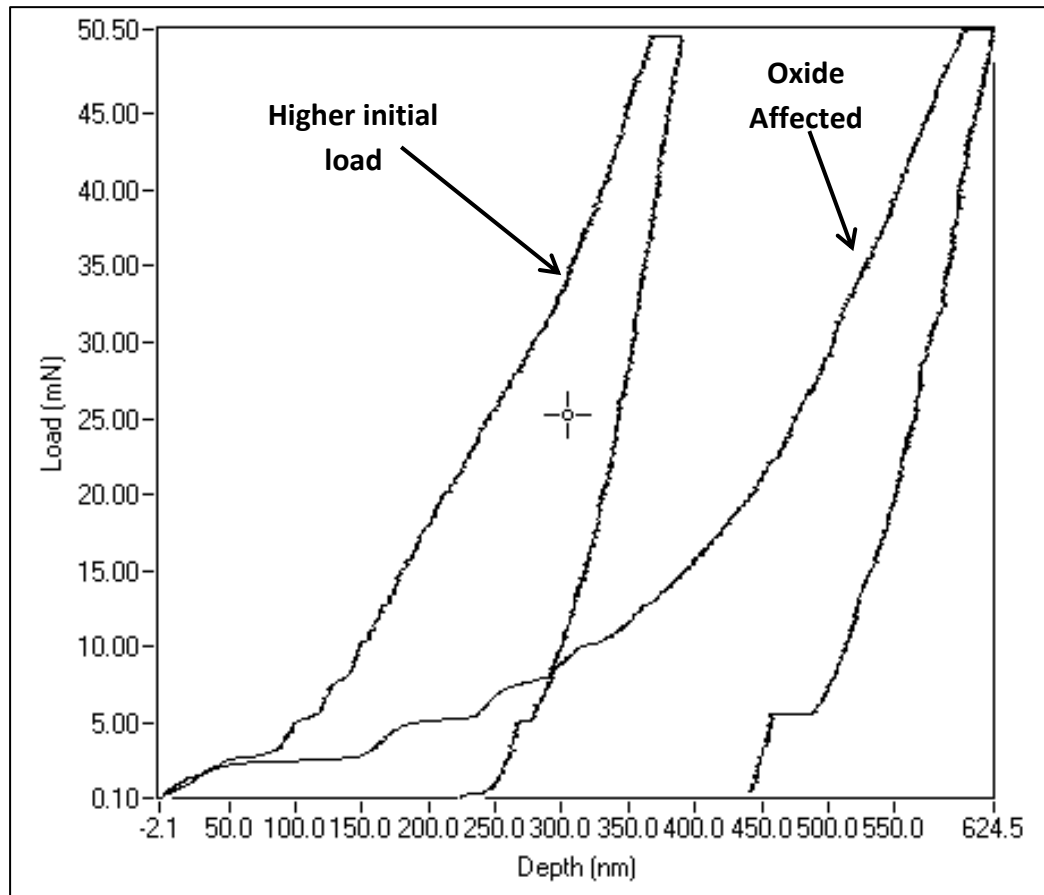
Figure 20: TiCN Hysteresis Curves affected by Sample Oxidation

The curve which reaches the greatest depth starts at the surface of the oxide and so there is a rapid depth increase at the start of the loading cycle as the indenter pushes through the oxide. For the indentation which reaches a lower depth the initial load was increased so that the indentation started much closer to the sample surface, the influence of the oxide layer is greatly reduced and the maximum depth is much lower than that of the first curve. It is important to note that experiments using this technique will not begin at 0mN load on the load depth plot. This is because the load axis will be offset by the initial load applied. It is therefore important to extrapolate the loading curve back to zero applied load in order to obtain the true load depth profile for the material being tested. This correction is made during data analysis and can be made as either a manual correction to the depth or a fit to the loading curve.

This technique allows the test window to be extended, this however is only useful for soft or extremely brittle oxide layers which can be pushed through before the start of the measurement. Even in these cases there is a chance that the oxide will add to the load support or change the creep behaviour of the indented region. Potential oxide influence will be discussed in detail within the relevant sections.

3.4 Nanoindentation creep testing

All creep test experiments were performed at elevated temperatures using the same equipment as standard high temperature nanoindentation experiments. The heated indenter methodology was also used to ensure the thermal stability of the hardware.

3.4.1 Samples

Sample of P91 and P92 steel were taken from circumferentially welded butt joints, details of the welding process and manufacturing method have been detailed by Yaghi et al. [116]. The chemical composition of the P91 and P92 parent and weld material is shown in Table 5. In order to sample the different microstructures in the welded pipe, samples of the parent material, PM, weld material, WM and heat affected zone, HAZ, were identified and removed using a water-jet cutter. A schematic of the regions within a typical weld are shown in Figure 21.

The water jet cutter was used to ensure that the cutting process did not affect the grain structure of the samples. The sample size was approximately 10mmx10mmx2mm. Samples were deliberately kept thin in order to minimise the temperature difference between the measured sample stage temperature and the temperature at the surface measurement thermocouple. Once cut the samples were mechanically polished, finishing with 1μm diamond grit, the bulk samples were then tested in this state.

Table 5: Composition (wt%) of P91 [116] and P92 [8]P92 parent and weld

	Fe	C	Mn	P	S	Si	Cr	W	Mo	V	Cu	Nb	N	B	Al	Ni
P91 PM	Bal	0.11	0.36	0.022	-	0.048	8.74		0.98	0.21	0.08	-	-	-	-	-
P91 WM	Bal	0.087	1.04	0.28	-	0.04	8.6		1.02	0.22	0.03	-	-	-	-	-
P92 PM	Bal	0.10	0.45	0.015	0.002	0.45	8.62	1.86	0.33	0.21	-	0.076	0.047	0.0034	0.019	0.27
P92 WM	Bal	0.09	0.73	0.007	0.005	0.26	8.47	1.67	0.47	0.189	-	0.042	0.046	-	-	0.65
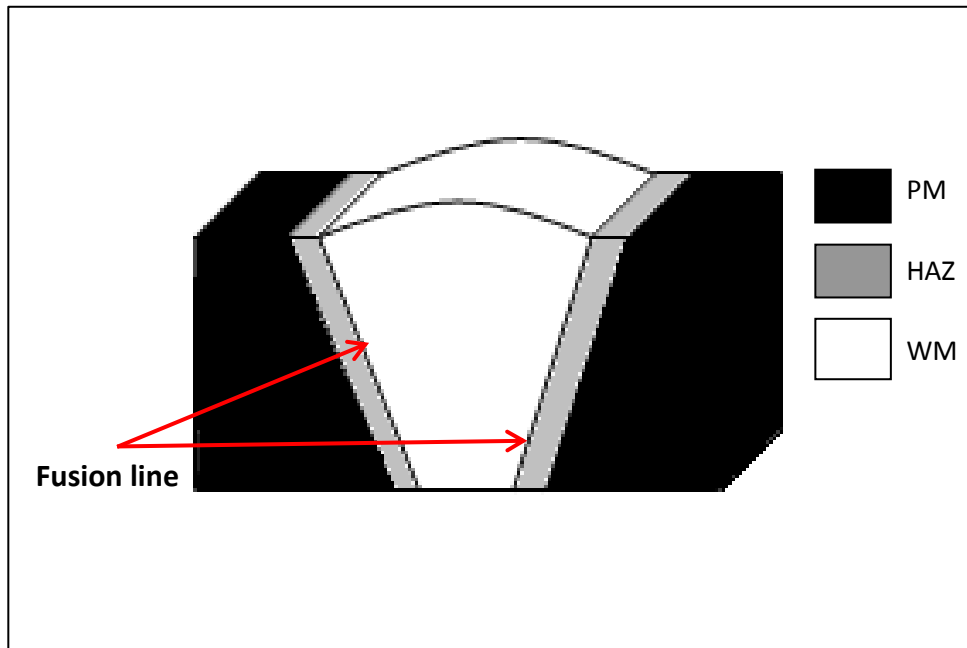
Figure 21: Schematic of regions within a fusion joint

The heat affected zone is approximately 5mm across and so each HAZ sample also contained regions of the parent and weld materials. In order to perform indentations across the HAZ it was necessary to accurately determine the position of the fusion line on each sample. This was done by etching the samples with acidic ferric chloride solution to reveal the different microstructures of the parent and weld materials [117]. Optical microscopy and micrometer measurements were then used to find the position of the fusion line relative to the edges of the sample. Once the position of the fusion line had been located the samples were repolished to give a good surface for nanoindentation measurements. The position of the fusion line on each sample was noted by measuring the distance from the edges of the sample at various points and the samples re-polished to allow indentation on a fresh surface. Figure 22 shows a typical optical image of the fusion line in P91.
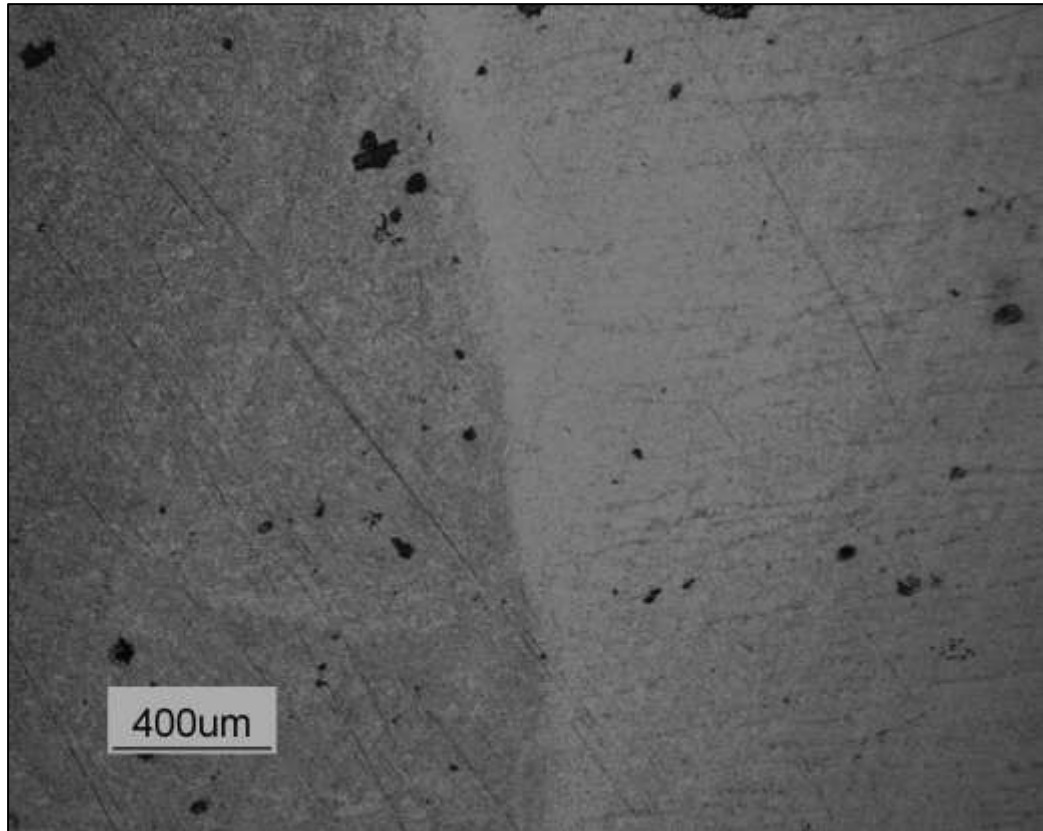
Figure 22: Optical image of fusion line in etched P91 sample

3.4.2 Berkovich indentation creep testing

Experiments were performed on the areas of interest on each sample in a manner similar to standard elevated temperature nanoindentation experiments. A 20s loading time and 10s unloading time were used, there was also a 120s thermal drift correction data collection. Unlike normal experiments however, a long 300s dwell at peak load was used in order to collect data to find the power law creep stress exponent.

The method followed to find the creep stress exponent is the same as is outlined in the review paper by Goodall and Clyne [98]. In order to calculate the stress exponent it is necessary to find representative stress value as the stress field in the sample varies by a large degree from the centre of the indentation to its edge. The technique of using a representative stress is consistent with principles developed in early impression creep work [91]. The

stress is taken as the applied force divided by the projected contact area as shown in Equation 9.

$$\sigma = \frac{P}{A}$$

Equation 9

The strain field beneath the indenter is similarly complex and so a representative strain value is also needed. The general form of this approximation for the Berkovich was developed by Mayo and Nix [92] and takes the form shown in Equation 10.

$$\dot{\varepsilon} = \frac{1}{h}\frac{dh}{dt}$$

Equation 10

The creep observed in nanoindentation dwell data is assumed to be due to steady state deformation and as such should relate to the standard secondary creep equation, Equation 11. As mentioned in Chapter 2 there are several questions around the validity of this assumption. In nanoindentation creep testing the indentation depth is constantly increasing. Therefore new material is continually entering the stress field and undergoing primary creep, this could have an influence on the measured creep exponent. This influence will be discussed with specific reference to relevant results in later Chapters 4 and 6. Nanoindentation creep tests are also much shorter than conventional creep tests therefore there is some question as to whether the material has reached the secondary creep regime. What is critical here is that the volume of material in the affected region is much smaller than in conventional tests and the deformation rates measured are much lower. The result is that the high strain rates associated with primary creep drop very rapidly. Throughout this study attempts will be made to compare experimental strain rates with those observed in more conventional tests.

$$\dot{\varepsilon} = c\sigma^n exp\left(-\frac{Q}{RT}\right)$$

Equation 11

Therefore by determining values of stress and strain and plotting them on logarithmic axes it is possible to obtain a straight-line plot, the gradient of which gives the stress exponent n.

A set of typical nanoindentation dwell data is shown in Figure 23. The first 60s of the data is creeping at a much faster rate than the rest of the data, this effect is driven by the applied load and is dependent on the loading rate. This data was removed from each data set before analysis, the remaining data was then divided into sections containing 5 data points. Each section was analysed using Equations 9 and 10 to find a representative stress and strain value. To determine the stress from Equation 9 the force used was the maximum load for the experiment and the contact area was calculated from the indenter area function using the depth at the centre of the section being analysed. To calculate the strain from Equation 10 the gradient of the section is used as *dh/dt* and the depth at the centre of the section used for *h*.
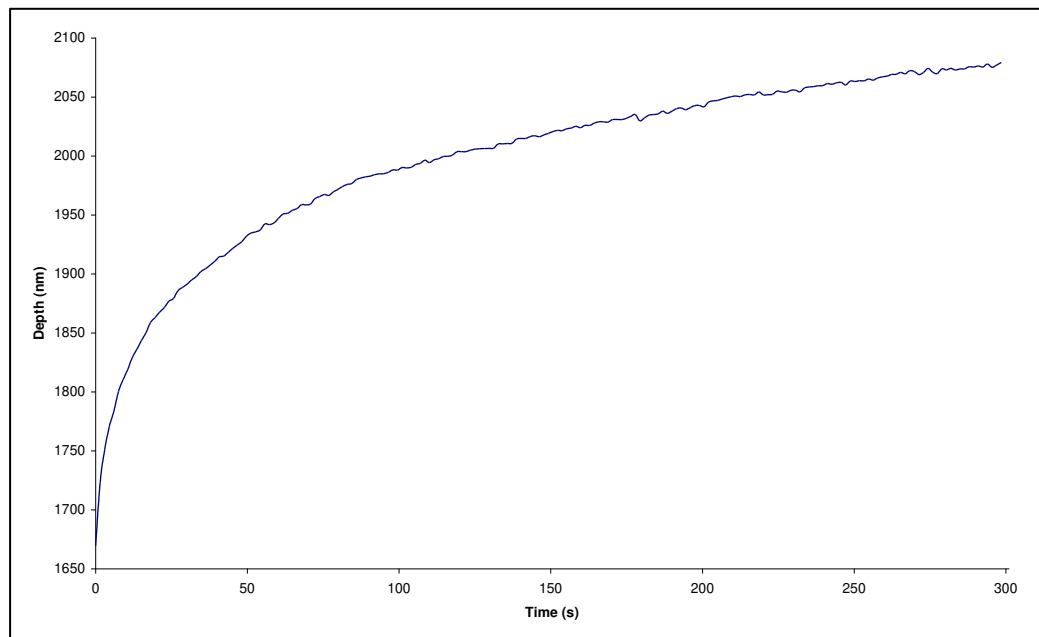
Figure 23: Typical nanoindentation peak load dwell data

The representative stresses and strains from each section were then plotted on log axes, the gradient of a fit to the data is the stress exponent for that data set. Dividing the data in this way allows a stress exponent to be found from each indentation made so that a mean exponent can be found from one set of indentations. An example of a Stress vs. strain plot is shown in Figure 24, the stress exponent is taken to be the gradient of the fit to the stress strain data shown on the plot.
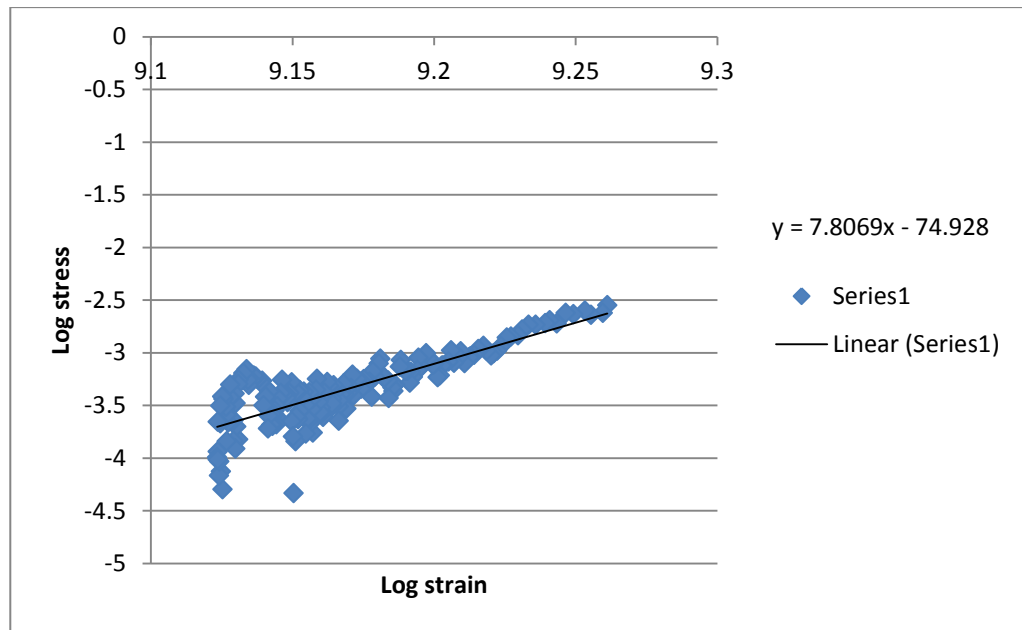
Figure 24: Example of stress vs. strain log plot

3.4.3 Determination of stresses during indentation creep experiments

The method outlined in section 3.4.2 uses empirical observations in order to evaluate a representative stress value. In order to allow more detailed analysis of the creep data it is important to be able to analyse the stress levels at which the indentation creep test was performed.

The stress state beneath a Berkovich is complex with maxima and minima in positions determined by the contact geometry. In order to evaluate this typically modelling is required to accurately evaluate the pressure distribution under load. For this study commercial software Oliver and Pharr for coatings (OPfC) (SIO, Ummanz, DE) was used to analyse the stresses during indentation

tests. This package differs from FE simulations in that there is no modelling, analytical calculations are used in order to evaluate the stress fields from the nanoindentation data. The analysis in the OPfC software is based around the concept of the effective indenter, this concept is covered in greater detail in section 5.4.1 and so will only be covered briefly now in order to explain the operation of the software.

 Load, depth and time data are exported from the NanoTest software and input into the OPfC software. The software then determines a fit to the nanoindentation unloading data and establishes the geometry of the "effective indenter" which best describes the interaction between indenter and sample shown by the unloading data. This effective indenter geometry is then used to evaluate the contact pressure under load which can then be used to determine the von Mises stress distribution under the indenter at different times during the indentation experiments. Results of this calculation can be viewed as 2D maps in the plane of the indentation. The full methodology for the analysis used in the software has been published by Schwarzer and Pharr [118].

Chapter 4 - Nanoindentation Characterisation of P91 Steel

4.1 Introduction

 Failures in welds for power station materials have been linked to differences in material properties across the heat affected zone (HAZ) of the weldment [16]. Lifetime prediction simulations for welded components are made based on the properties of the bulk parent and weld materials. In order to improve the accuracy of these assessments it is important to factor in the effect on the creep deformation of the different microstructures observed in the heat affected zone. Accurate characterisation of the properties of the different grain size regions is fundamental to achieving this goal.

Conventional test techniques such as Vickers hardness testing and acoustic wave transmission tests allow determination of the hardness and elastic modulus of bulk materials but have limited use in applications requiring the determination of properties of small structures or coatings [41, 112]. Similarly conventional uniaxial creep testing is a proven technique for determining the creep properties of bulk materials but the minimum sample size needed means it cannot be used to determine the change in creep behaviour across the heat affected zone [11, 17]. In order to find values for the material across the HAZ, test techniques such as impression creep testing have been developed in order to allow characterisation of smaller volumes of material [17, 20, 21, 23, 24, 26, 27, 96, 119-121]. Much of the work in this area has been to determine the relationship between the stresses in the impression creep test and those used in conventional uniaxial tests [26, 120-122]. Typically the stresses in the impression creep test are significantly higher than in uniaxial testing so that a conversion factor is needed in order to relate the results to the corresponding uniaxial test stress. Originally impression creep tests were performed using a flat ended conical probe[17, 120] although difficulties were encountered due to the singularities in the stress field at the

edge of the probe [119, 122]. As a result rectangular cross section probes and those with other geometries have been employed to minimise this effect [24, 119, 121, 122]. Whilst this technique allows characterisation of much smaller volumes of material than conventional creep test techniques, the probe is still quite large and only allows determination of general properties for the heat affected zone [3, 119, 120].

Nanoindentation offers a ready solution to this problem. Indentations can be made in the order of microns across, as a result they can be made at a much finer pitch than conventional hardness tests allowing accurate determination of the variation in hardness across the heat affected zone. Techniques have been developed in order to evaluate the creep behaviour from indentation dwell data in order to find properties such as the activation energy and creep stress exponent [91]. These techniques have been applied successfully in order to find the stress exponents of solders and other materials from room temperature experiments [93-95, 97, 123-127] although testing of a range of metallic bulk samples under similar conditions gave inconsistent results [98].

In the case of P91 steel the main interest is not in the room temperature properties but the mechanical and creep properties at operating temperatures ~650°C. There is a growing library of work related to the study of material creep behaviour at elevated temperature. So far this work has been mostly examined the effect of increasing test temperature on the creep rates at peak load in order to evaluate the creep resistance of the materials tested[100] although some sources have used the creep data to find elevated temperature creep stress exponents [128, 129]. This study will begin with an assessment of the validity of application of techniques to find stress exponents on bulk samples of parent and weld for P91. This data can then be compared to data from conventional tests in order to validate the technique before the heat affected zone can be characterised.

4.2 Experimental Results

Error bars in this section are ±2 standard error unless stated.

4.2.1 Room temperature measurements

Room temperature indentation experiments were performed on both the parent and weld materials in order to determine a baseline for nanoindentation hardness and Young's modulus. Indentations were made to a range of loads in order to evaluate any depth dependence in the properties determined. The Young's modulus results are shown in Figure 25. As expected the moduli of the parent and weld are the same within the deviation of the measurements. The modulus does not change as a function of depth as it is not affected by mechanical work hardening of the surface layers. The Young's modulus from these nanoindentation experiments is however not consistent with previous measurements which indicate a modulus of around 200GPa [13, 105].

Table 6: Room temperature results

Material	Load (mN)	Plastic Depth(nm)	Hardness (GPa)	Young's modulus
PM	10	302 ± 8	3.72 ± 0.18	230 ± 19
	50	755 ± 16	3.50 ± 0.14	260 ± 23
	100	1194 ± 15	3.13 ± 0.08	251 ± 8
	150	1509 ± 14	2.96 ± 0.05	253 ± 18
	200	1780 ± 19	2.79 ± 0.06	243 ± 19
WM	10	303 ± 14	3.71 ± 0.31	240 ± 67
	50	746 ± 12	3.57 ± 0.11	260 ± 9
	100	1110 ± 41	3.66 ± 0.31	265 ± 18
	150	1347 ± 86	3.79 ± 0.55	290 ± 24
	200	1608 ± 54	3.45 ± 0.26	299 ± 23
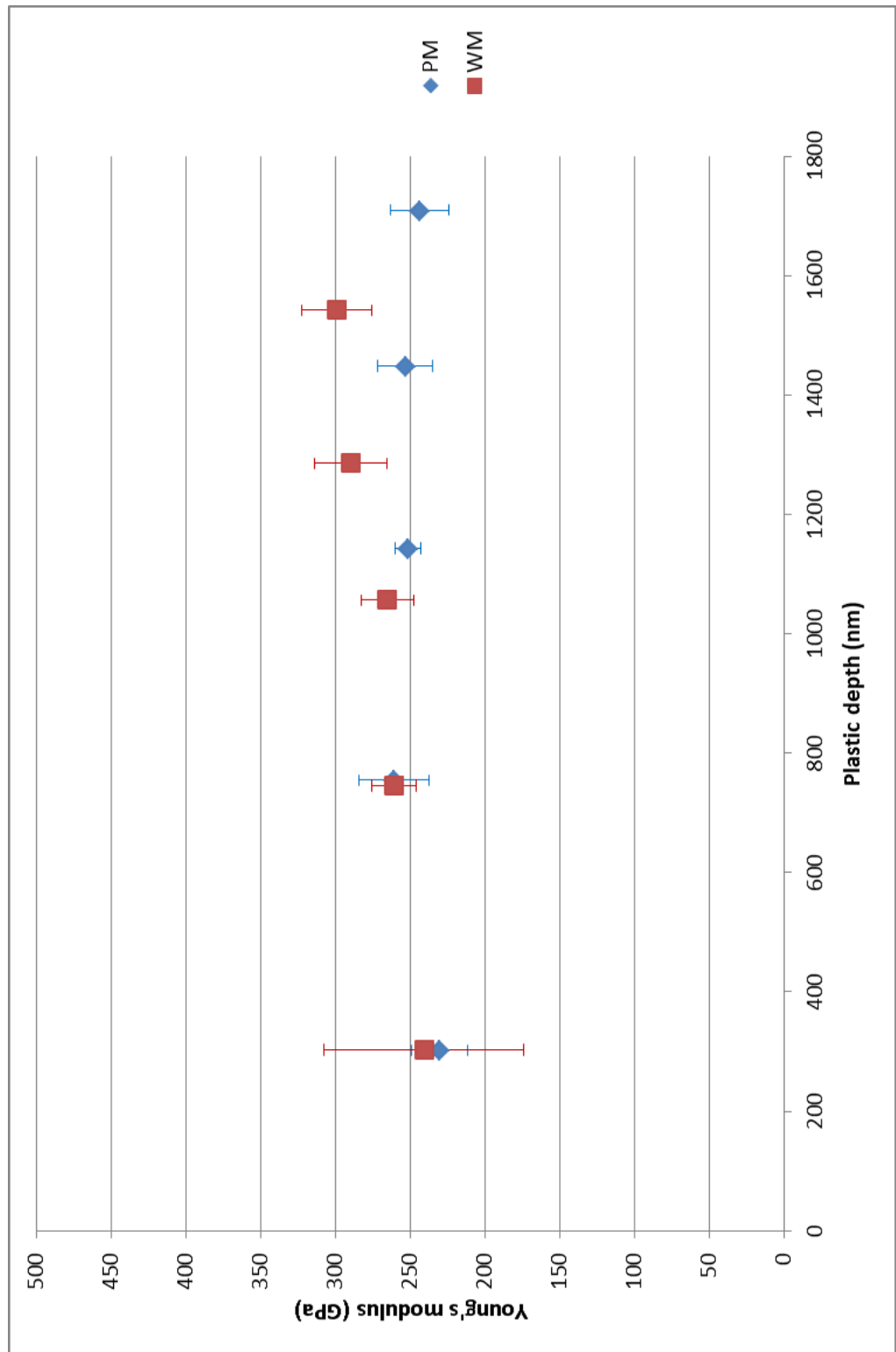
Figure 25: P91 Room temperature Young's modulus

Some of the difference in modulus may be due to errors in the area function as a result of the area function calibration not accounting for radial displacement of the reference material during indentation, this is discussed in more detail in Appendix I. Even so the difference between the results in this study and literature are too large to be explained solely by this effect. The difference is also too large to be explained by any effects due to crystallographic orientation of the indented grains or the composition of the material in the indented region[130]. Experiments were repeated on different samples of parent of weld and parent material and results were consistent with those shown in Table 6. Further study is required to understand and evaluate the observed differences but, as the focus of this thesis is elevated temperature properties and the room temperature result is consistent, no further examination is made in the current study.

Unlike the Young's modulus there is clear depth dependence in the room temperature hardness measurements in Table 6. This is due to a hard layer at the surface of the material formed by polishing. In order to obtain a surface suitable for nanoindentation the samples are mechanically polished since this is necessary in order to minimise the surface roughness. ISO14577 states that in order to remove the effect of surface roughness on indentation results the indentation depth should be at least 20 times RA. Polishing minimises the surface roughness and means that shallow indentations can be used to characterise the material. However in the case of samples such as steel, mechanical polishing causes work hardening of the surface. The effect of this on nanoindentation experiments contributes to depth dependence in the hardness measured on the sample. The results of this can be seen in Figure 26. The hardness of both the parent and weld materials is higher closer to the surface. The hardness then drops as the indentation depth increases, getting closer to the hardness from conventional micro hardness tests which found the hardness of the parent to be is 2.2 GPa for a 300Kg force. These indentations are on the order of hundreds of microns across, much wider than

typical nanoindentation impressions. The hardness and modulus data are tabulated in Table 6, there is a clear statistical difference between the hardness at the surface and that recorded for higher indentation depths.

There is still no absolute correlation between the nanoindentation and micro hardness result due to the effect of pileup on the nanoindentation hardness. Nanoindentation hardness is calculated from an approximation of the contact area at peak load based on the penetration depth. Depth sensing indenters can only account for depth moved from the initial contact surface. In metallic materials, plastically deformed material displaced from the indentation crater builds up around the indenter above the initial contact surface and helps to support the indenter load. The contribution of this material to the load support is not accounted for in standard technique used to determine the hardness. This leads to an underestimation in the contact area and an overestimation in the calculated hardness [44, 45].

There are several techniques developed to determine the contact area accurately using post indentation microscopy and these have been used to establish a greater correlation with conventional hardness test results [131]. These were not used in this study in order to allow a more reasonable comparison with the nanoindentation hardness measured at elevated temperature. When tests are performed at $650^{o}C$ the indentations are held at temperature for a long time after the impression has been made. During this time stresses in the plastically deformed region relax as a result of the thermal treatment, so that much of the deformation is recovered before it would be possible to image the indent. Therefore more accurate comparisons can be made by performing nanoindentation experiments to the same contact depth at room and elevated temperatures.
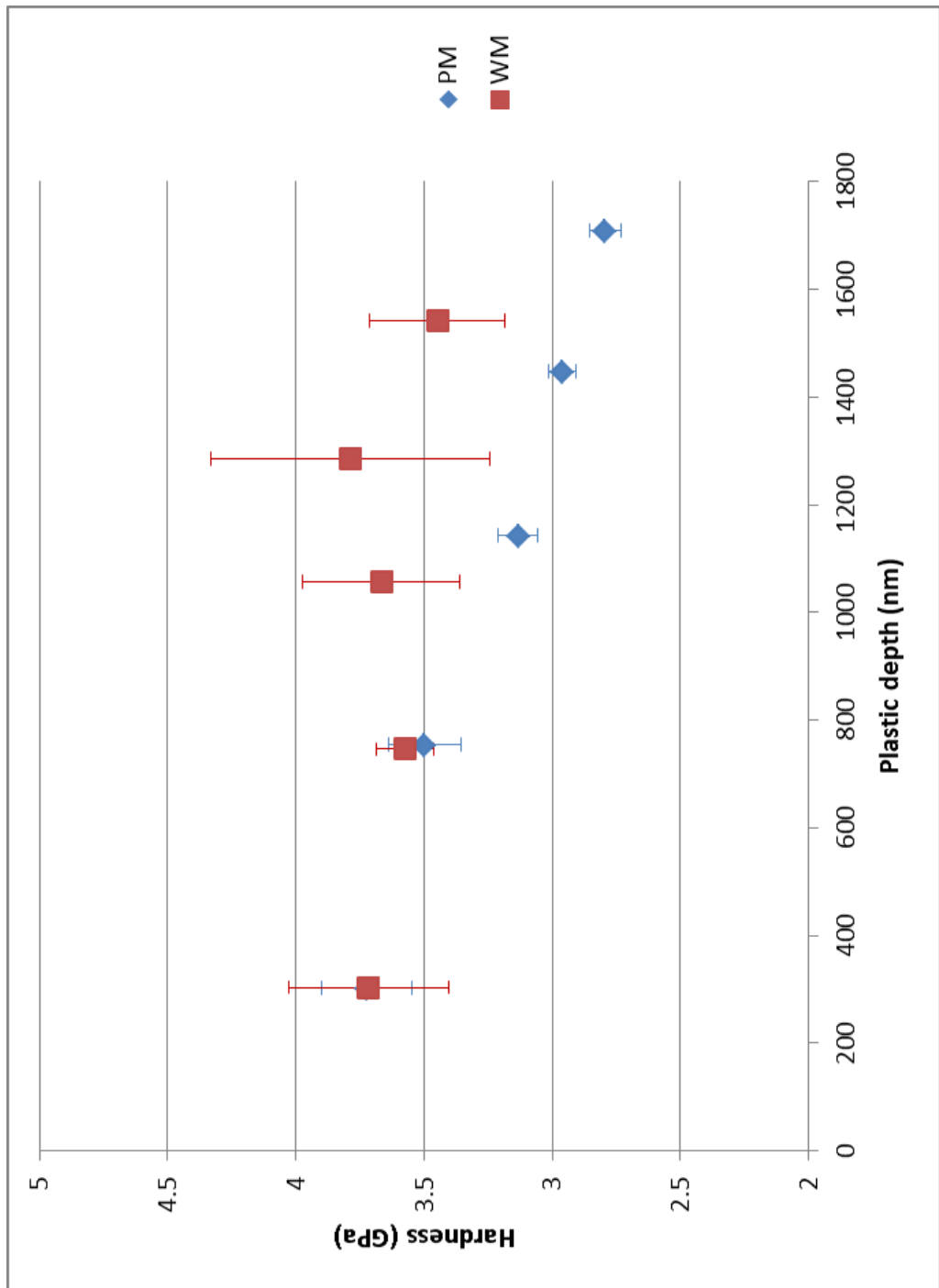
Figure 26: P91 room temperature hardness

In order to assess the change in material properties across the heat affected zone, it was important to examine the homogeneity of the parent material. Large variations in the mechanical properties of the parent material, particularly the hardness, would make it difficult to distinguish between the unaffected material and the heat affected zone. In order to examine this 10 x 10 indentation grids were made on a sample of the bulk parent material. The indentations in the grid, made to 150mN maximum load, were placed 30μm apart in both y and z axis. Once analysed, these data can be viewed in the NanoTest software as a property map to look for variations on hardness and elastic modulus. The software takes the mechanical properties calculated for each indentation and extrapolates between points in order to create a contour map of the sample properties.
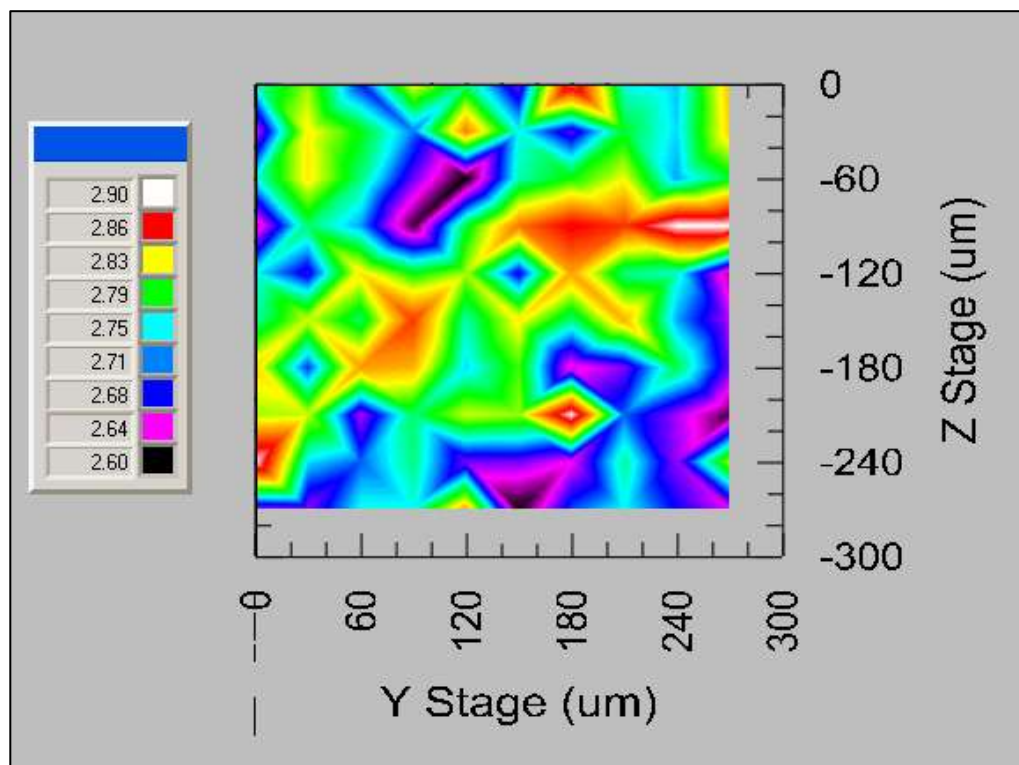
Figure 27: P91 PM hardness map

The hardness results from a 150mN grid on a parent material sample are shown in Figure 27. The mean hardness for the 100 indentations was 2.73 ± 0.08 GPa, this is in line with the hardness and deviation found in the previous experimental results. The map shows that there are no regional variations of

65

hardness within the 300μm grid. The hardness varies around the grid but there are no regions where the hardness is distinctly different from the surrounding material. The indentations with higher hardness may indicate where the indentations have found carbides on the sample surface although the variation could equally be due to regional variations in the surface roughness affecting the initial indenter contact.

Figure 28 shows the modulus map of the same region of the sample, again the variation in the modulus value is the same as those calculated from previous indentations made in a smaller regions of the sample. The mean reduced modulus for the 100 indentations shown in Figure 28 is 225 ± 17 GPa.
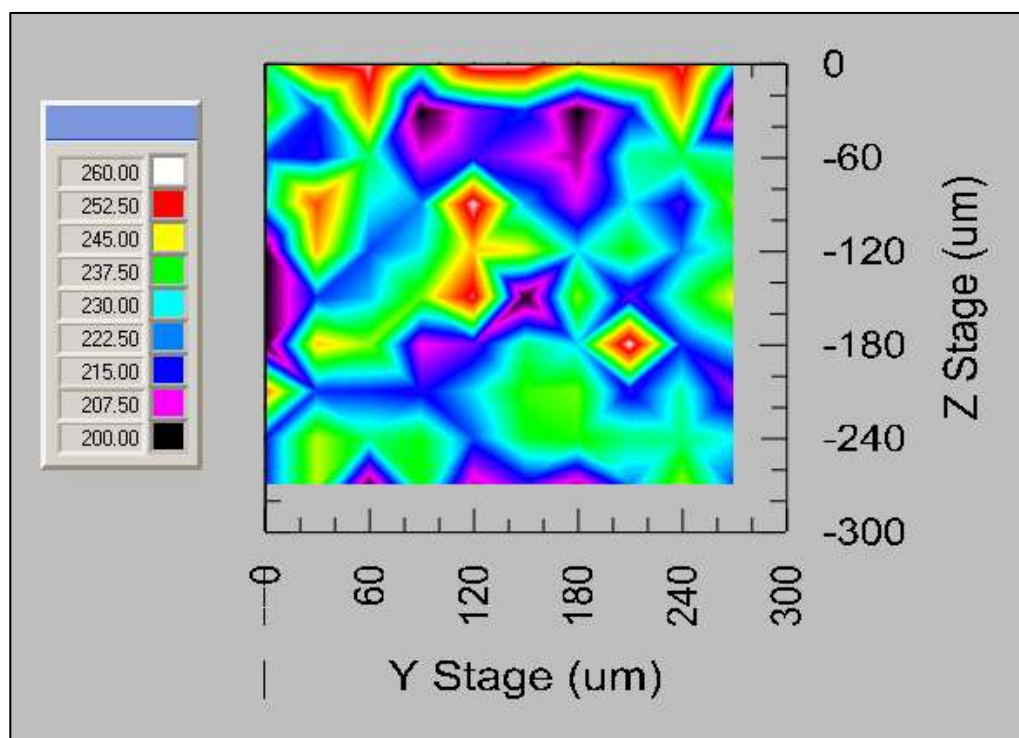
Figure 28: P91 PM modulus map

It has been shown that the heat treatment during welding leads to variation of the grain sizes in the heat affected zone of the parent material [117, 132]. The difference in grain size affects the hardness of these regions and the gradient of the hardness at room temperature has been assessed in previous

studies [133]. Indentations were made around the boundary between the parent and weld in order to look at the mechanical properties of the HAZ. Similar to the maps on the parent material, indentations were made 30μm apart in a 10x10 grid in order to build up a 300x300 μm image of the sample properties around the fusion line. The results are shown in Figure 29, the weld material is on the right hand side of the grid. There is a clear change in the hardness along the fusion line, this lower hardness in the heat affected zone agrees with previous research which reported a drop in the hardness through the small grained region of the heat affected zone followed by a gradual increase until the hardness returns to the level of the bulk of the parent material. The start of this can be seen in Figure 29, the region of the heat affected zone at the fusion line has a slightly higher hardness. The hardness then drops rapidly as denoted by the black and purple shaded areas. Typically the heat affected zone extends several millimetres from the fusion line so this image represents only a small section of the affected region. Nonetheless the test is sufficient to indicate that nanoindentation is sufficiently sensitive to detect the property changes across the heat affected zone.

Typically it is expected that changes in the grain size in a material which lead to a change in the hardness have little or no effect on the stiffness. This is confirmed by the modulus results shown in Figure 30 from the same 300μm by 300μm grid of indentations that was used to generate Figure 29. The results show the same variation observed in both the parent and weld material, the average reduced modulus is 267 ± 14 GPa. The modulus values are spread randomly across the grid with no clear regions where the modulus is different from the surrounding material.
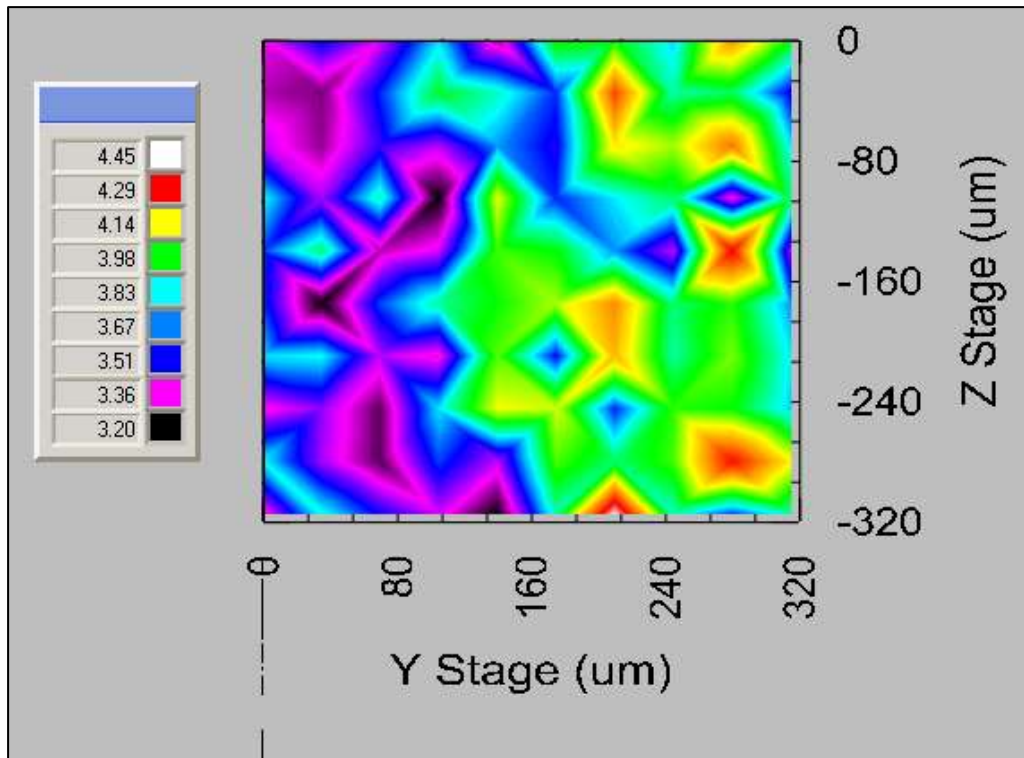
Figure 29: P91 HAZ hardness map
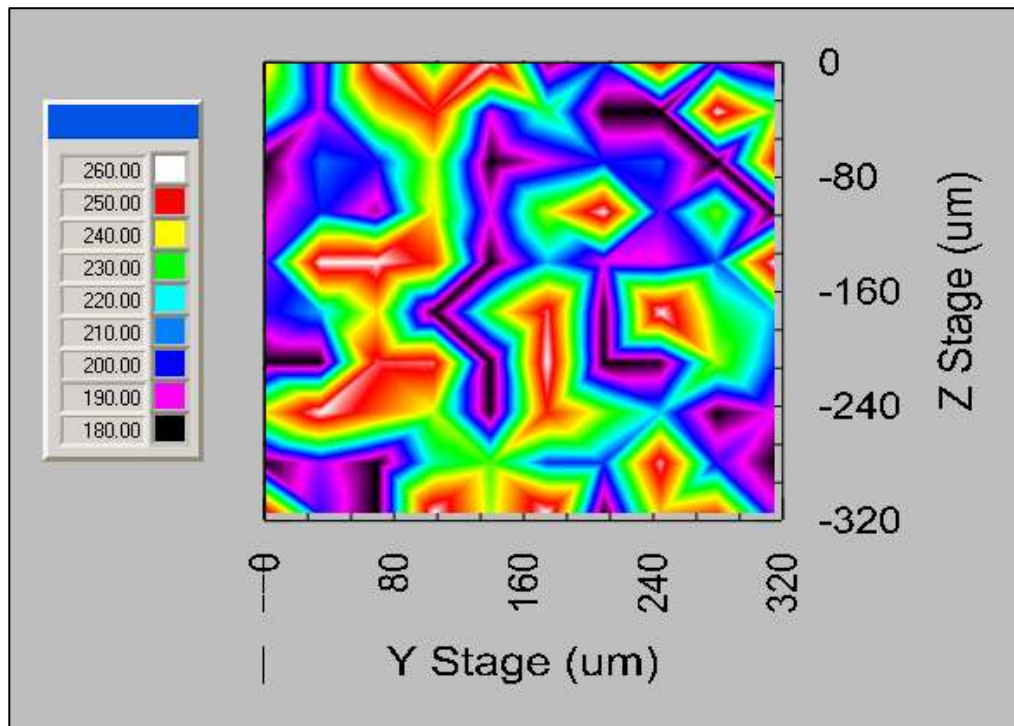
Figure 30: P91 HAZ modulus map

4.2.2 Elevated temperature measurements

The key interest in this study is the properties of P91 at the temperatures it will experience during its operation in power plants. Experiments were performed at 650°C in order to evaluate the hardness, Young's modulus and creep properties at this temperature. Figure 31 shows the hardness profile of the sample as a function of depth. The temperature ramp to 650°C takes around six and a half hours with a similar amount of time to stabilise once the test temperature has been reached. As a result any work hardening introduced into the surface by polishing anneals out so that there is no longer depth dependence to the hardness. There is still a slight increase in hardness for the shallower indents but this is due to the effect of pileup on the indentation data.

The Young's modulus of the sample was also evaluated from the 650°C indentation data, the results of this analysis are shown in Figure 32. As at room temperature there is no depth dependence in the Young's modulus value for either the parent or weld materials. There is however a difference between the modulus calculated for the weld and parent using conventional Oliver and Pharr analysis and in both cases the modulus is higher than the 110GPa determined by ultrasonic methods reported in other sources [13]. Several sources have reported that conventional Oliver and Pharr analysis can be inaccurate when analysing materials exhibiting viscous behaviour [20, 134, 135]. The effect for viscous recovery on the data is to artificially stiffen the indentation response leading to high Young's modulus data like those seen in Figure 32. This effect is investigated more thoroughly in Chapter 5. The steel data was therefore re-analysed using the creep compliance technique [134] in order to remove the effects of viscoelastic recovery on the data analysis, see Section 5.3 for details.
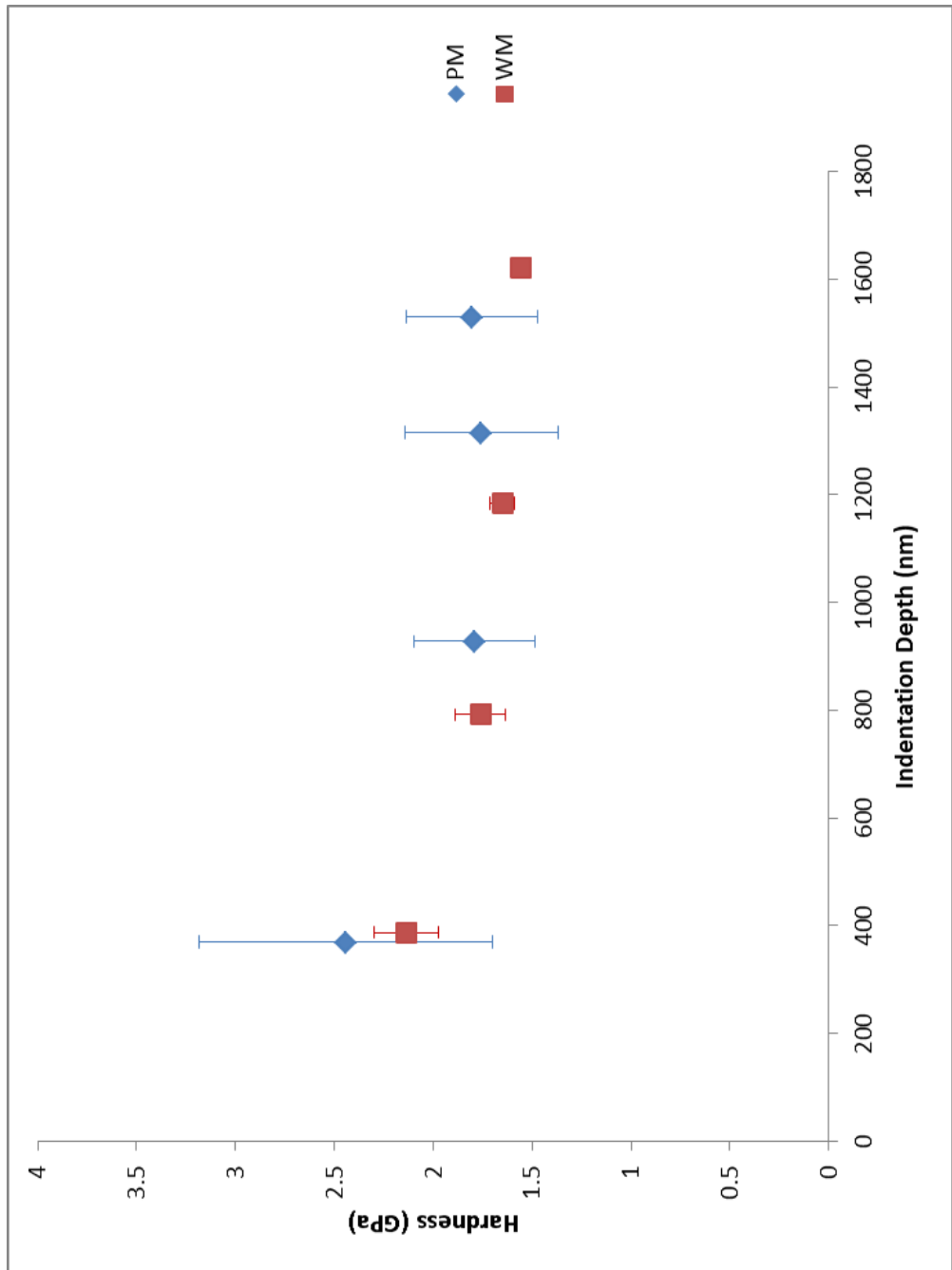
Figure 31: P91 650^oC hardness

The results of the reanalysis are shown in Figure 33, the effect of the correction is to reduce the modulus value for both parent and weld material. With the correction there is no statistically significant difference between the parent and weld properties, this is consistent with previously reported results which state that the parent and weld have the same modulus[3]. In addition the corrected modulus is also around 110GPa in line with previously reported results. Tabulated results for the hardness and modulus of both the parent and weld material are shown in Table 7. There is no statistically significant variation of the hardness with depth apart from the shallowest indentations. This is not a work hardening effect as after 8 hours at 650°C this will have annealed out. Instead the apparent higher hardness is simply due to an increased surface roughness effect for these shallower indentations.

Table 7: P91 steel 650°C nanoindentation results

	Load (mN)	Plastic Depth (nm)	Hardness (GPa)	Young's Modulus (GPa)	Creep compliance Young's modulus (GPa)
PM	10	370 ± 63	2.44 ± 0.74	137 ± 48	124 ± 40
	40	927 ± 86	1.79 ± 0.31	155 ± 28	117 ± 17
	75	1315 ± 158	1.76 ± 0.39	145 ± 18	109 ± 14
	100	1530 ± 149	1.81 ± 0.33	155 ± 20	113 ± 12
WM	10	389 ± 5	2.14 ± 0.16	207 ± 36	140 ± 20
	30	792 ± 32	1.76 ± 0.13	179 ± 26	113 ± 15
	60	1184 ± 23	1.65 ± 0.06	176 ± 19	107 ± 7
	100	1620 ± 25	1.56 ± 0.05	177 ± 15	101 ± 6
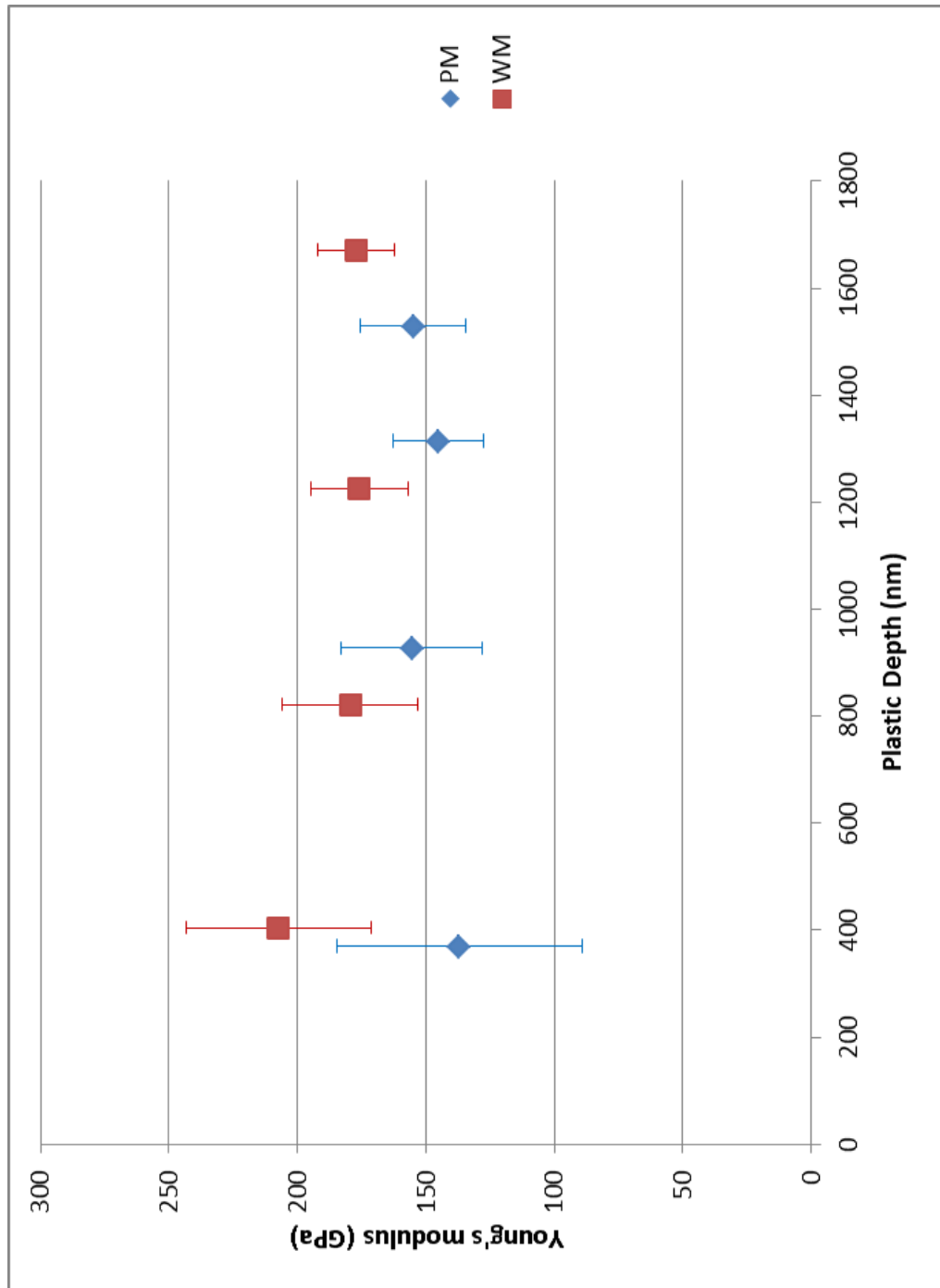
Figure 32: P91 650°C Young's modulus
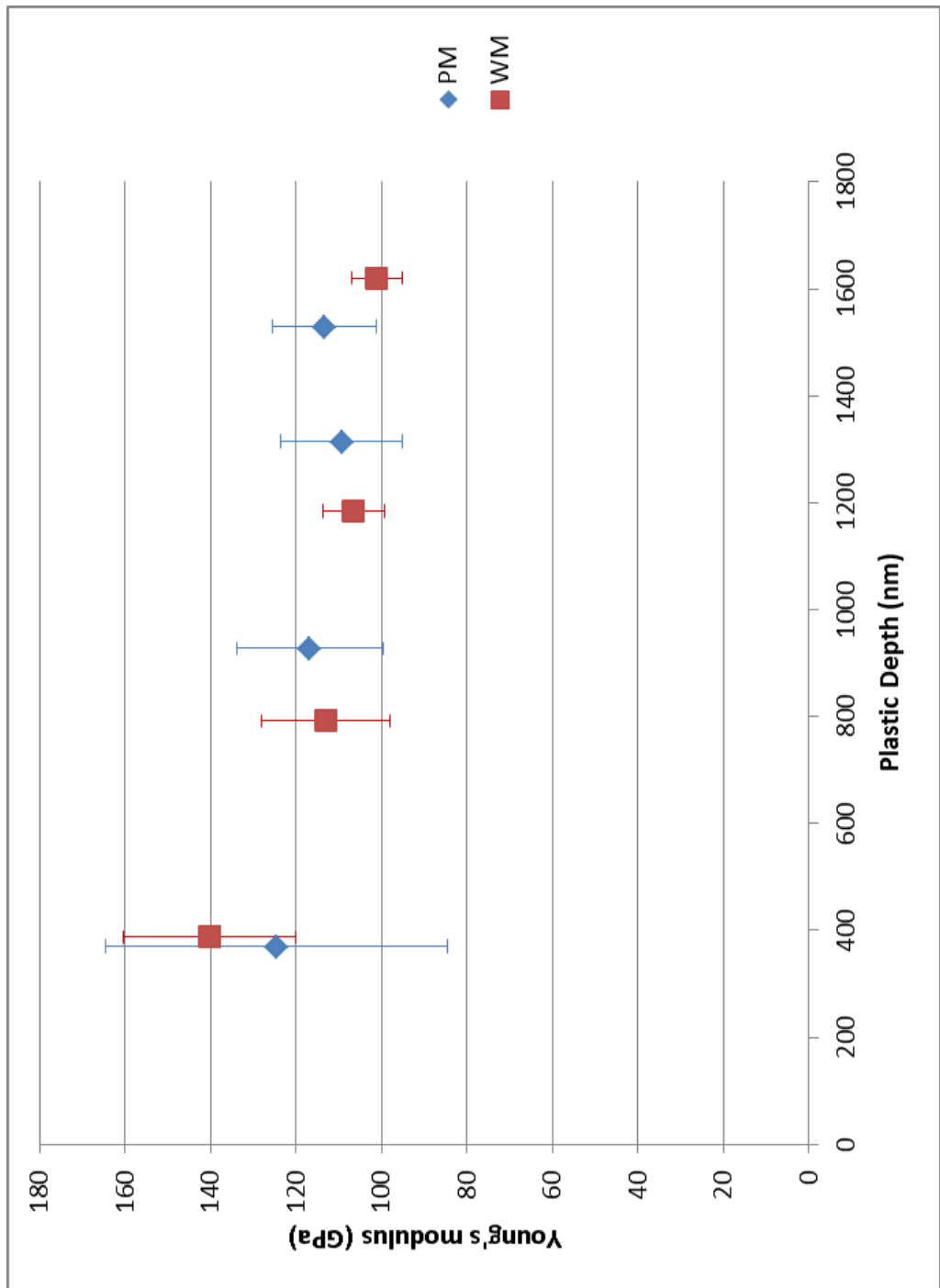
Figure 33: P91 650°C Young's modulus corrected with the creep compliance method

Literature values of creep stress exponents from uniaxial creep testing at 650°C for the parent and weld material are 8.46 and 7.22 respectively [3]. Table 8 shows the results of nanoindentation creep testing which ranks the materials exactly the same as the conventional testing. Additionally the stress exponents are very close to the values calculated from uniaxial creep tests. Creep test indentations were made to high loads in order to keep the contact area large enough to encompass several grains. Microstructural evaluations of aged P91 have found a sub grain size of around 500nm [117]. Indentations made with a Berkovich indenter are approximately 7 times wider than they are deep, Therefore the indentations in this study, which were around 1.5µm deep, would cover a surface area of around 10µm and so will encompass several sub-grains. Variations in the creep exponent are due to the effect on the stress field as it crosses the grain boundary, this leads to variation in the measured creep strain, similar effects have also been observed in impression creep testing [120, 136].

Table 8: Creep stress exponents calculated by nanoindentation

Material	Load (mN)	Stress exponent
Parent	100	8.95 ± 0.47
	200	7.89 ± 0.41
Weld	100	7.49 ± 0.45
	200	7.44 ± 0.35

In conventional uniaxial creep testing a very strict stress regime is used, tests are performed at sub-yield stress levels [11]. The literature values stated were from uniaxial tests performed at a constant stresses in a range from 60-100 MPa, therefore additional consideration is needed in interpreting the results from nanoindentation creep testing. There are two main considerations which must be understood in order to evaluate the accuracy of this empirical technique. The correlation between the representative stress and strain used

in the analysis, and the true stress beneath the pyramidal indenter and the validity of the assumption that the constant load dwell data can be treated as secondary creep.

Dimensional analysis of the equations used to find an effective strain rate has found that this is an effective and verifiable characterisation of the strain rate during the dwell period [137]. What is less clear is the physical significance of the effective stress calculated using Tabors methodology [91]. There is an existing analytical technique used to evaluate the stresses beneath a sharp indenter [118].This has been incorporated in commercial software Oliver and Pharr for coatings (SIO, Ummanz,DE). Using this software it was possible to assess how the representative stress relates to the stress that the majority of the material under the indenter is experiencing.

Typical effective stress at the end of the dwell period on the parent and weld material are shown in Table 9. The approximations are typically in the order of Giga Pascals, well outside the range of stresses used in conventional testing. In fact stresses at this level would be expected to drive rapid failure in the material and would certainly drive creep behaviour different to those observed in conventional creep tests as they are well above the yield stress of the P91 parent and weld material which is around 800MPa at room temperature [132] falling to around 400MPa at 650°C [12].

Table 9: Representative indentation stress values

Material	Load (mN)	Representative stress at end of 300s dwell period (GPa)
PM	100	1.19 ± 0.06
	200	1.16 ± 0.06
WM	100	1.11 ± 0.02
	200	1.20 ± 0.02

The OPfC software was used on parent and weld material to calculate the stress field under the indenter at the end of the dwell period. An explanation of the operation of the software is given in section 3.4.3. The results of the evaluations are shown in Figures 34, 35 and 36. These indicate that the effective stress calculated is greater than even the maximum stress beneath the indenter. Only a small volume of material is experiencing the maximum stress, the majority of the material in the stress field is actually under much lower stresses than the material at the point of peak stress.

Figure 34 shows the typical von Mises stress distribution beneath a 100mN indentation creep test on the parent material. The maximum stress is around 650MPa, much lower than the representative stress evaluated using Tabor's method and much lower than the yield stress of the parent material. This maximum stress is also much higher than the stress that the majority of the material is experiencing, most of the material in the stress field is experiencing stresses of 300MPa or lower. The plots on the left hand side of Figure 43 show the variation in stress along the axes shown in the right hand stress distribution. They show that only a small part of the indented region experiences the maximum stress with the stress rapidly diminishing so that the average stress experienced is significantly lower.
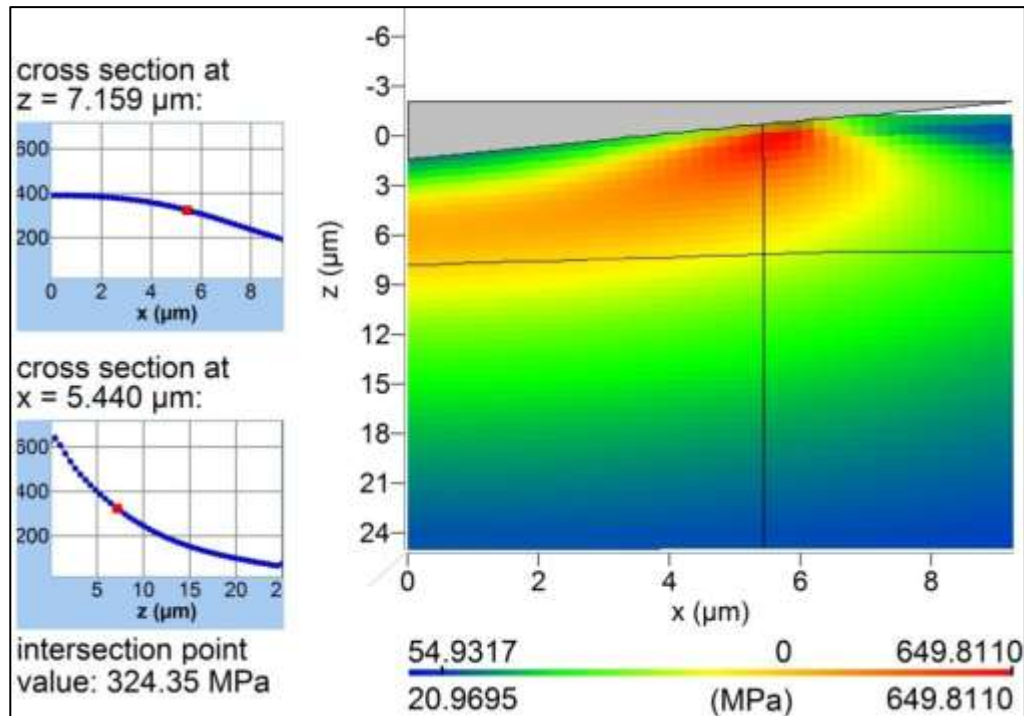
Figure 34: 100mN P91 PM creep test stress field at the end of the dwell period

Figure 35 shows a similar stress plot for the 200mN creep indentation on the parent material. Here the maximum stress is significantly higher than in the 100mN tests, at around 990MPa, meaning that large volumes of material are experiencing stresses much higher than their yield stress. This would explain why the creep exponents calculated for these tests are low compared to both the 100mnN indentation creep tests and the literature uniaxial creep data as the deformation is no longer dominated by the same mechanism as the stress regime observed in the previous test.
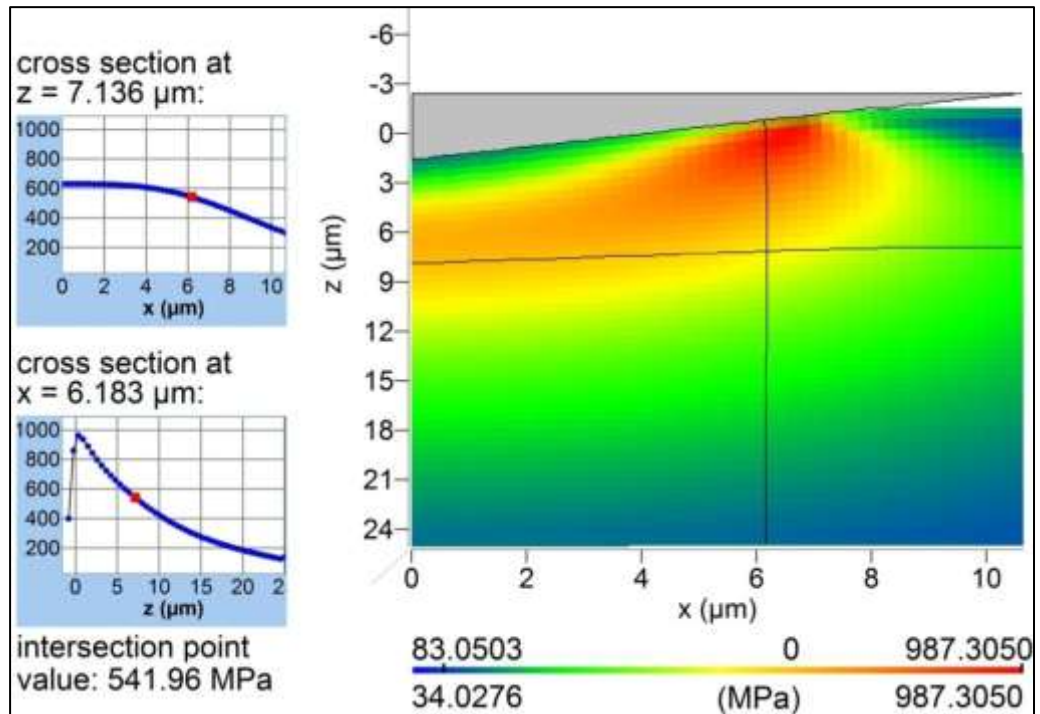
Figure 35: 200mN P91 PM indentation creep test stress field at the end of the dwell period

The stress field for a 200mN creep test on the weld material is shown in Figure 36, a much higher creep rate is observed in tests on the weld material, therefore there is a much greater degree of stress relaxation. The result of this is that the maximum stress is significantly lower than the equivalent 200mN maximum load creep test on the parent material. Even at this higher load the weld material experiences stresses below the yield stress. Therefore there is much better correlation between the 100mN and 200mN test results on the weld material.
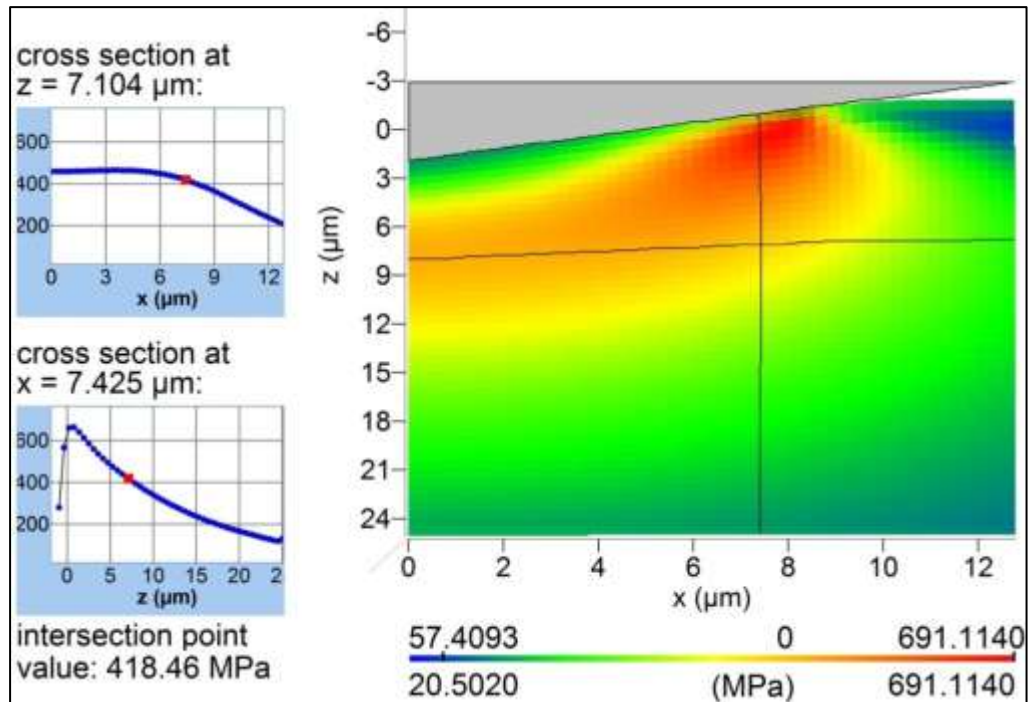
Figure 36: 200mN P91 WM indentation creep test stress field at the end of the dwell period

Another question over the creep exponents derived from nanoindentation creep data is related to the validity of the assumption that the steady state indentation dwell data can be treated as indicative of the secondary creep behaviour of the material. The problem is that, unlike conventional creep tests where the stresses are constant, during the constant load dwell the indentation depth is continuously increasing therefore new material is continuously entering the stress field. This material will undergo primary creep so that the steady state dwell data is actually a combination of primary and secondary creep. This has been presented as the probable cause of the variability in the creep exponents calculated in some materials as primary creep exponents are known to be much more variable than secondary creep stress exponents [138]. This may have contributed to the variability seen in the nanoindentation creep test results.

Despite this uncertainty, several sources have reported nanoindentation creep exponent determination at room temperature which correlates well with conventional test results. In general the materials to which this

technique has been successfully applied are those which have relatively low melting temperatures. These materials show a highly viscous indentation response and therefore a quite high creep rate under load. At room temperature most metals show very low creep rates under this regime so it is likely that the secondary creep rate is not sufficient to be distinct from the primary creep due to additional material entering the stress field. As the testing on the P91 parent and weld material was performed at 650°C approximately 45% of the melting temperatures of P91, the creep rates were relatively high. It was therefore assumed as in previous studies that the steady state indentation creep data was dominated by secondary creep.

The oxide layer that forms during testing could also potentially affect the creep rates during the indentation dwell as the oxide is expected to have very different creep properties to the steel. As with the hardness the thickness of the oxide at the time experiments were performed has not been assessed therefore it is difficult to quantify any potential influence on results.

4.3 Summary

Nanoindentation experiments have been used to examine the mechanical properties of P91 steel and weld material at both room temperature and a temperature they could experience in their standard operating conditions. The results agree well with previous studies on these materials. Further to this an investigation of the ability of nanoindentation creep testing to characterise these materials and the steps needed to interpret these results has been made. This has shown that the sensitivity of creep indentation experiments is sufficient to distinguish between the P91 parent and weld materials. The results of these evaluations are also consistent with creep exponents found from conventional uniaxial creep tests

This result is unexpected given the different apparent stress conditions in uniaxial and nanoindentation creep testing. More detailed analysis of the data from the indentation creep tests has shown that nanoindentation hardness is not equivalent to even the maximum stress during the creep hold. The change

in hardness during the hold at peak load has been shown to be an accurate analogue for stress relaxation. Determinations of the stress field during the creep test have shown that the actual stresses are much lower than those predicted by the hardness analogue. This could contribute to the calculated nanoindentation creep exponents being the same as those calculated from sub yield stress creep tests. It is still not clear though what the influence of primary creep on the recorded data is. There must be some influence as new material is entering the stress field throughout the creep hold

Experimental time at 650°C was limited by the ability of the purge to slow the rate of oxidation of the steel. After the ramp to experiment temperature and stabilisation time the sample had already been at elevated temperature for around 11 hours, therefore the amount of experiments that could be performed before a thick oxide layer was formed on the sample surface was limited to around 50 indentations. Any potential effect of the oxide on the mechanical properties or creep behaviour is difficult to determine. At the end of testing there was a visible discolouration of the sample surface indicating an oxide layer at least a few hundred nanometres thick. An oxide layer this thick is likely to have affected the properties determined by nanoindentation as even the high load experiments only reached a maximum depth of around 2μm.

It is unclear though the rate at which this oxide layer formed as the sample was at temperature for around forty hours in total with testing beginning after around 14-16 hours. A hard oxide scale may explain the slightly higher hardness observed in the shallow 10mN indentations performed on both parent and weld materials. This effect is not seen in the deeper indentations though suggesting that at this time the oxide layer was not that thick. Although not done in this work, in order to evaluate the oxide formation fully samples could be heated to 650°C within the purged chamber and left at temperature for different durations. Microscopy could then be used to determine the thickness of the oxide layer after different times. This would allow more reliable evaluation of any potential oxide influence on the

experimental results. The amount of time at temperature could be extended by improving the purge to further slow the oxidation of the steel, or by using an indentation system housed in a vacuum chamber to prevent oxidation.

Chapter 5 - Correcting time dependent displacements in nanoindentation analysis

5.1 Introduction

Data from the P91 steel at elevated temperature showed higher than expected Young's modulus. In order to understand potential causes for this, a study was made of known limitations of nanoindentation analysis applied to materials which undergo time dependent deformation under load i.e viscoelastic materials.

One of the limitations of the nanoindentation technique is the inability of conventional analysis to identify and correct time dependent depth changes in the collected data [137, 139-141]. The term time dependent depth change applies to any measured change in the recorded depth which is not directly influenced by a change in applied load. These time dependent depth changes are observed in materials which exhibit viscous behaviour, most commonly they are reported in testing on polymeric materials [135, 139, 142-144]. Viscous behaviour has also been reported when examining the properties of power law creeping metals [134, 141].

In the context of this thesis' main goal to characterise steels at elevated temperatures, further investigation of potential influence of the visco-plastic deformation under load on the calculated results was needed. The effect on creeping materials is of particular relevance to this thesis as metallic materials exhibit creep behaviour at elevated temperatures. It is generally accepted that the main effect of time dependency in the recorded depth data is on the Young's modulus calculated using the standard Oliver and Pharr methodology [144, 145].

Methods have been developed in order to correct the errors in calculated modulus associated with time dependent depth changes. One common approach is to use constitutive models to approximate the behaviour of the

material under load. In these models the material is represented by combinations of linear springs and viscoelastic dampers represented schematically by dashpots. Sources have used models containing different combinations of these constitutive components in order to represent the behaviour of viscous materials under load [137, 143, 146-148]. The majority use a three element Zener model as shown in Figure 37, this model is intended to represent a standard linear viscoelastic solid. The model consists of a linear spring in series with a Kelvin-Voigt model, springs are described by their moduli E and dashpots by their viscosity η. There is however no unifying model which accurately describes the behaviour of all viscous material. Models are therefore typically designed to describe the indentation behaviour of a specific material. Some authors have elected to use different 3 element models or increase the number of elements used to represent the viscous behaviour of the material depending on the complexity of the system being represented[135].
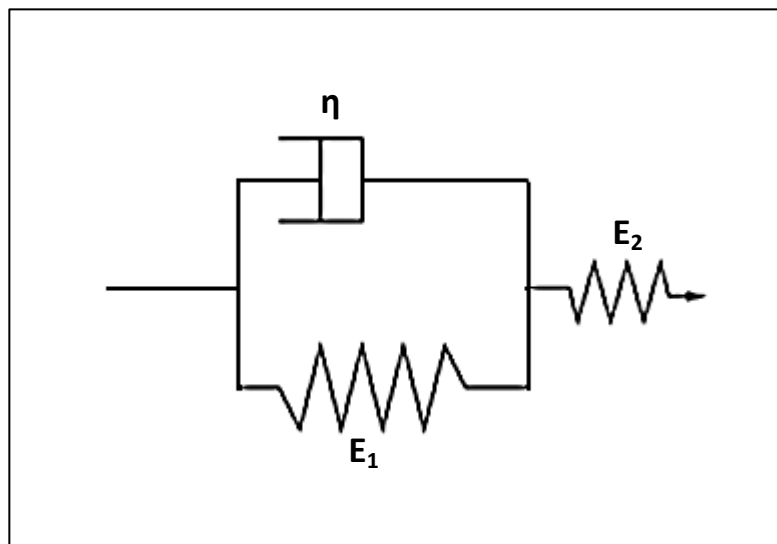
Figure 37: Standard linear viscoelastic solid model

In addition to the analytical analysis techniques developed to correct time dependent depth changes, several authors have applied techniques based on

empirical observations to correct to the data[134]. These empirical corrections have been employed successfully to a range of polymeric materials and carry the benefit that they does not require FE modelling or other advanced analysis tool allowing rapid determination of material properties.

In order to evaluate the influence of time dependent depth changes on conventional nanoindentation analysis results, experiments were performed on a range of samples including polymeric materials and metallic materials at elevated temperatures. This same data was then reanalysed using two techniques designed to correct the influence of time dependent depth changes on depth sensing indentation results. The first of these techniques is an empirical method which has been previously used in the analysis of both polymeric materials at room temperature and metallic samples at elevated temperatures [134]. The second is a new analytical method developed by the Saxonian institute of surface mechanics (Ummanz, Germany) and incorporated in their commercially available "Oliver and Pharr for coatings" software. This analytical solution uses a similar approach as conventional analysis but modifies several aspects in order to account for the time dependent behaviour. This chapter presents the results from the three analysis techniques and evaluates the ability of the correction techniques to eliminate the influence of time dependent behaviour on the results.

In order to allow thorough evaluations of the corrections for viscous materials, experiments were performed on polyamide 66, polycarbonate as well as P91 steel weld and parent material. The polyamide and polycarbonate were expected to exhibit visco-elastic behaviour at room temperature and so were tested only at ambient temperatures. The steel samples were tested at elevated temperatures in order to assess the effect of creep on the collected data. The P91 steel was tested at 650°C as this is the standard operating temperature used in power transmission applications and its properties at this temperature are of particular interest to materials engineers.

Correcting time dependent displacements in nanoidentation analysis

The polyamide 66 samples were made from beads of the base material which were heated and then pressed between two glass plates in order to give the flat surface needed for nanoindentation. The polycarbonate sample was cut from an extrusion moulded sheet and was therefore nominally flat. The gold sample was a 24 carat jeweller's sample and the steel sample was cut from a welded pipe, exact details for this sample are given in section 2.4.1. The gold and steel samples were mechanically polished using graded polishing cloths and finished using a 1μm diamond wheel. The gold sample was then annealed at $600^{o}C$ for 4 hours and allowed to cool slowly. This was done so that any grain growth due to heating occurred before the sample was taken to temperature. It was not possible to anneal the steel sample in the same way due to the effect that any sample oxidation would have on the nanoindentation data (see section 3.3.2).

Standard nanoindentation calibration and data collection protocols were used as outlined in Chapter 3. One commonly used technique for minimising the influence of time dependent depth changes is to use very high unloading rates during data collection. In order to assess this technique, different unloading rates were used in order to see the effect of time dependent depth changes on the collected data for each sample. The experimental parameters used for testing the three samples are shown in Table 10.

Table 10: Experimental parameters for materials with time dependent properties

Sample	Test Temperature (^{o}C)	Max Load (mN)	Unload rate (mN/s)	Thermal drift (s)	Dwell period (s)	Poisson's ratio
PC	22	1	0.1	120	30	0.3
PA 66	22	5	0.5,0.25	120	30	0.35
P91 Steel	650	100	10.0	120	40	0.3

5.2 Conventional Corrections

Early studies on nanoindentation data noted the influence of time dependent deformation during the dwell period on the gradient of the initial unloading data and the subsequent effect on the calculated modulus. In these studies at room temperature holds of different lengths were utilised in order to allow sufficient relaxation time before unloading [111]. The results of the P91 steel in the previous chapter were from tests with a 40s dwell at peak load. When analysed this data returned moduli which were higher than expected suggesting that creep was affecting the slope of the unloading data. In order to see if this was the case much longer dwell periods were used to allow a greater degree of relaxation before unloading.

Figure 38 shows representative curves from experiments to a 100mN maximum load on the P91 parent material at 650$^\text{o}$C with 40s and 300s dwell periods. As expected there is a larger depth increase in the 300s dwell due to continuous creep deformation under load. The data from the 300s dwell looks obviously different from the 30s dwell data. Apart from the obvious larger depth increase in the dwell there is a clear difference in the slope of the initial unloading data.

The qualitative assessment is confirmed by the analysis results as shown in Table 11. The 40s dwell period data gives higher moduli than expected for the parent and weld material. The modulus of both materials has previously been reported as 110GPa, analysis of the creep rates at the end of the dwell data gives some indication as to the cause of this. Both the parent and the weld material have creep rates over 2nm/s at the end of the 40s dwell, even though this would be expected to diminish rapidly as the load was removed it will still have an effect on the initial unloading data. The higher creep rate seen in the weld material explains why its modulus is apparently higher than the parent.
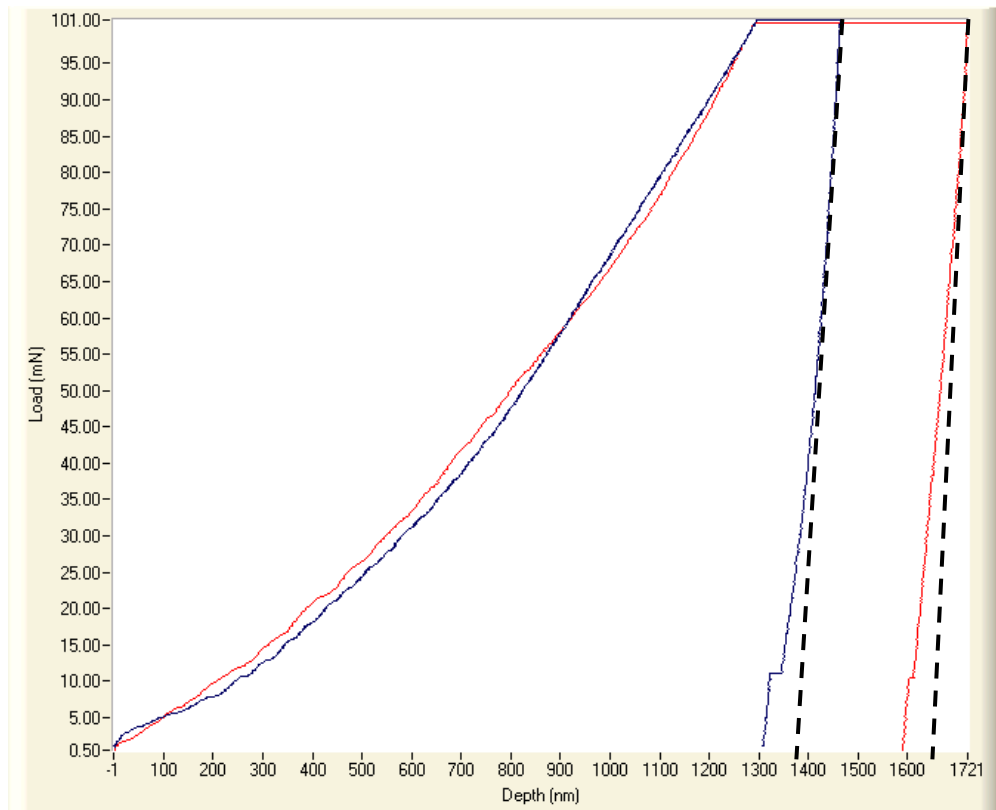
Figure 38: P91 indentation data at 650°C with 30s and 300s dwell

The creep rate at the end of the dwell was assessed by looking at the deformation rate in the last 5 seconds of the dwell period. For both materials the creep rate at the end of the longer dwell period is much lower than the shorter dwell period tests. This has a clear effect on the calculated modulus, the parent material modulus is now in line with previously reported data. Similarly the value for the weld material is now much closer to previous results although there is still some difference between the two materials possibly due to the higher creep rate observed in the 300s dwell weld data still affecting the analysis.

Table 11: P91 long dwell period data

Material	Dwell period duration (s)	Reduced modulus (GPa)	Young's modulus (GPa)	Creep rate at end of dwell (nm/s)
PM	40	140 ± 15	157 ± 21	2.03
	300	104 ± 2	109 ± 2	0.48
WM	40	157 ± 10	179 ± 15	2.55
	300	119 ± 8	128 ± 11	0.65

5.3 Creep compliance correction

Given the limitations on available test time due to sample oxidation there are many benefits to correcting shorter dwell period data rather than using a longer dwell period, because a larger number of tests can be performed in the test window. One technique which has been developed for this reason is the creep compliance correction. This technique was developed to correct visco-elastic effects on polymer results but has also been used successfully to correct creep effects in high temperature experiments on metals [134]. This is possible as, although the physical mechanism is different, visco-elasticity for polymers instead of visco-plastic creep, the effect on nanoindentation data is the same. In both cases it is the effect of viscous deformation on the first few seconds of unloading data which influences the result. Therefore often technques developed to correct viscous effects in polymers at room temperature can be applied to correcting data from creeping metals at elevated temperatures.

Correcting time dependent displacements in nanoindentation analysis

5.3.1 Creep compliance correction methodology

The creep compliance correction is an empirical correction which treats time
dependent depth changes as an additional component in the contact
compliance [134, 139]. The problem is treated as a two element Maxwell
model, in this regime the true compliance, $C_{elastic}$, is a combination of the
measured sample compliance, $C_{apparent}$, and the so called creep compliance,
C_{creep}.

$$C_{elastic} = C_{apparent} + C_{creep}$$

Equation 12

$C_{apparent}$ can be found directly from the nanoindentation unloading data. C_{creep}
is calculated using data from the dwell at peak load and Equation 13.

$$C_{creep} = \frac{dh}{dP} = \frac{dh}{dt} \cdot \frac{1}{\frac{dP}{dt}} = \frac{\dot{h}_{creep}}{\dot{P}_{creep}}$$

Equation 13

dh/dt is the depth change with time at constant load and is determined from
the slope of the dwell data. The dwell data from the indentations was
exported and the loading rate dependent data at the start of the dwell period
was removed. The gradient of the remaining data was used as the depth
change at constant load, dh/dt, for that indentation. The portion of data

which was removed is highlighted in Figure 39. *dP/dt* is taken to be the same as the experimental unloading rate.
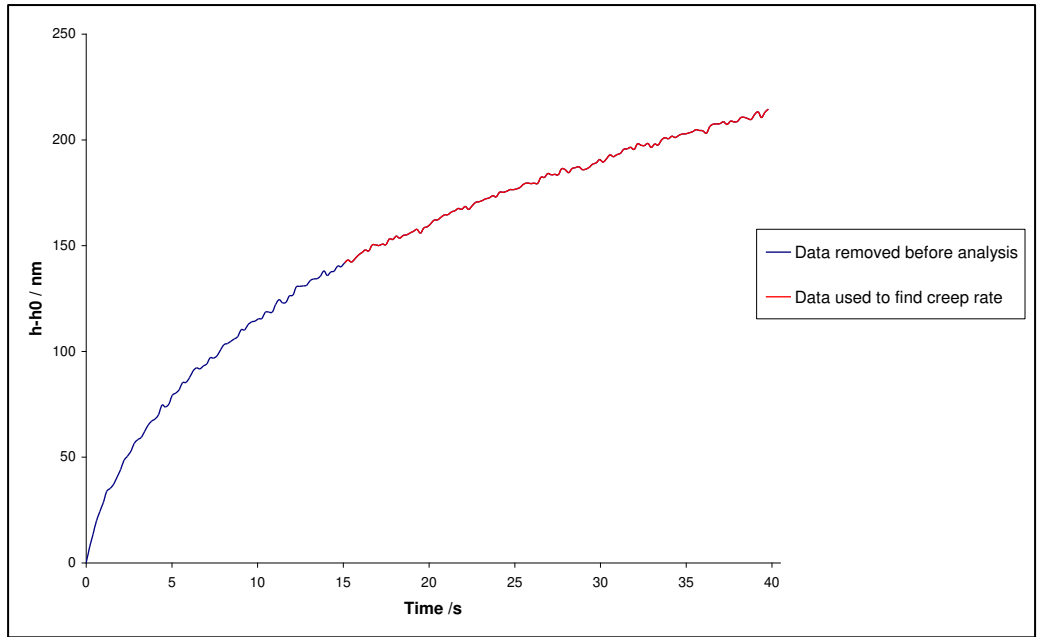
Figure 39: Dwell data used to find change of depth at constant load for creep compliance correction

By combining equations 12 and 13 to form Equation 14 it is possible to evaluate the Young's modulus of the sample corrected for time dependent effects.

$$C_{apparent} = \sqrt{\frac{\pi}{A}} \frac{1}{2} \left[\frac{1 - v^2}{E} + \frac{1 - v_i^2}{E_i} \right] - \frac{\dot{h}_{creep}}{\dot{P}_{creep}}$$

Equation 14

In practice the data was first analysed using the conventional Oliver and Pharr analysis as outlined in section 3.2.3. The results of this analysis, specifically the contact area and contact compliance were taken and entered into a spreadsheet for later use in Equation 14 as *A* and *C_apparent* respectively. Equation 14 has been taken directly from the Sawant and Tin paper [134], it

91

does not include the correction factor β from Equation 5. In order to maintain some consistency between the creep compliance and standard Oliver and Pharr analysis in this study, the beta factor has been added to the creep compliance calculation. Therefore the Young's modulus corrected by the creep compliance methodology is given by Equation 15.

$$E = \frac{1 - v^2}{\left[\left(2\beta \sqrt{\frac{A}{\pi}} \left(C_{apparent} + C_{creep} \right) \right) - \frac{1 - v_i^2}{E_i} \right]}$$

Equation 15

5.3.2 Creep compliance correction results

5.3.2.1 Creep compliance correction for polymeric materials

Polyamide 66 has its glass transition around 50°C therefore we would expect to see a degree of viscoelastic behaviour even at room temperature (~23°C). Conventional Oliver and Pharr analysis of the data indicates that there is a slight unloading rate dependency in the recorded results. The fitting coefficients from conventional analysis indicate the viscoelastic behaviour of the material may be affecting the conventional fit the unloading data and therefore the results, further discussion of this effect on fitting coefficients can be found in section 5.3.3.

Table 12: Polymer Young's modulus

Material	Unloading Rate mN/s	Oliver and Pharr Young's modulus GPa	Creep compliance Young's modulus GPa
PA 66	0.5	3.43 ± 0.16	3.43 ± 0.16
	0.25	3.48 ± 0.16	3.10 ± 0.15
PC	20	2.37 ± 0.05	2.00 ± 0.04

Table 12 shows the analysis results for the polymeric samples both with and without the creep compliance correction. In the literature the results of DMA testing of polyamide are reported as around 18% lower ~2.8GPa than the results from conventional indentation analysis [149]. This can be assumed to be due to a combination of the influence of viscoelasticity on the nanoindentation results and the so called confinement effect observed in nanoindentation results on several polymers. There is also the possibility that the hot pressing process used to fabricate the polyamide sample has affected the properties of the sample. The creep compliance correction does not alter the 0.5mN/s unloading period results but does make a correction to the 0.167mN/s unloading data as seen in Table 12. This is because the creep compliance correction assumes that the magnitude of correction needed is proportional to the creep rate at peak load and scales the correction with respect to the unloading rate. Therefore the creep compliance correction assumes a much greater unloading rate dependency than was experimentally

observed a significantly larger correction is therefore made to the slower unloaded data.

Literature results for polycarbonate report the modulus in the range 2- 3GPa so the results from the conventional analysis of the polycarbonate data in Table 12 are around the range that we would expect. Correction of the data using the creep compliance reduces the modulus by around 19%.

5.3.2.2 Creep compliance correction for P91 steel

Table 13 shows the Young's modulus of the P91 steel sample analysed using the conventional Oliver and Pharr and the creep compliance analysis techniques. The literature Young's modulus for P91 steel at 650°C is 110GPa [13]. As the mechanical properties of the parent and weld material are carefully matched no differences were expected in the Young's modulus. When the nanoindentation data was analysed using conventional Oliver and Pharr analysis, there was a 20GPa difference between the Young's modulus calculated for the parent and weld material. In addition to this, the stiffness of both samples is much higher than literature results for this material. The differences in the modulus when analysed using the conventional analysis techniques can be attributed to the different strain rates in the two materials during experiments. As noted in section 5.3.1 the weld sample the strain rate just prior to unloading is significantly higher in the weld material than the parent materials. This creep rate is what affects the gradient of the initial unloading slope (critical to the conventional analysis method), therefore explaining why the weld material is more affected.

Table 13: P91 steel creep compliance Young's modulus

Material	Unloading Rate mN/s	Oliver and Pharr Young's modulus /GPa	Creep Compliance Young's modulus GPa
PM	10	157 ± 13	113 ± 7
WM	10	177 ± 9	101 ± 2

When the P91 data is corrected using the creep compliance correction, the Young's modulus is reduced significantly for both parent and weld materials. This brings the values into line with the literature results, again suggesting that the viscous deformation during the dwell is affecting the unloading data. The correction is greater for the weld material due to the higher strain rate at peak load compared to the parent material. The strain rate at the end of the dwell period is 0.00260 ± 0.00017 s^{-1} for the weld material compared to 0.00167 ± 0.00016 s^{-1} for the parent material. This is consistent with behaviour reported from conventional creep testing which reports higher strain rates from the weld material compared to the parent when both materials are under equivalent loading conditions [3]. There is still however a difference between the creep compliance modulus for the parent and weld materials. It is likely in this case that the high creep rate observed in the weld material data has led to an over correction so that the calculated modulus is lower than both the corrected parent material values and the literature modulus of P91 steel.

5.4 Time dependent effective indenter

The final analysis technique used in this study was developed by Dr N. Schwarzer of the Saxonian Institute of Surface Mechanics (Ummanz,

Germany). The correction method was built into commercially available software "Oliver and Pharr for Coatings", OPfC, and was given to the University of Nottingham in order to assess its performance in correcting time dependent depth changes on a variety of samples. As with the creep compliance method this technique was designed to correct the influence of viscoelastic deformation on polymer data.

5.4.1 Time dependent effective indenter method

The technique builds on to the concept of the effective indenter [150] , this concept was developed in order to explain the power law fitting coefficients found in typical nanoindentation experiments. As stated in chapter 2 sample stiffness is found from a power law fit to the unloading data of the form shown in Equation 16.

$$P = \alpha(h - h_0)^m$$

Equation 16

Where P is indentation load, h is the indentation depth, h_0 the depth at the start of unloading and α and *m* are fitting coefficients. This fit is based on principles established by surface contact calculations made by Sneddon [113]. In these calculations the fitting coefficient *m* is dependent on the indenter geometry and should be 2 for conical/Berkovich indentation (Berkovich indenter contact is approximated to be the same as that for a conical probe) and 1 for flat punch indentation. In practice however, power law fitting coefficients for Berkovich indentation were found to be in the range 1.2- 1.4 [46], relating to an indenter geometry of a paraboloid of revolution.

Pharr and Bolshakov explained this using their concept of an effectively shaped indenter [150]. This considers the effect of the plastic deformation of the surface that occurs during loading, on the elastic recovery of the surface as the load is removed. The deformed surface will recover elastically when the load is removed. However the plastically deformed material will cause the surface to recover non-uniformly. This explained the breakdown of Sneddon's solution as the unloading surface will not conform to the indenter geometry. This adds additional complexity to the contact mechanics involved in indentation. Pharr simplified this problem by treating the unloading surface as flat and instead modifying the shape of the indenter to account for the elastic recovery of the deformed region.

The concept is explained schematically in Figure 40. During loading the indented region conforms perfectly to indenter geometry as shown in Figure 40(a). When the load is removed, elastic recovery of the surface means that the geometry of the indented surface no longer conforms to the indenter geometry as shown in Figure 40(b). This problem is complex but can be replaced with the much simpler problem of an arbitrarily shaped "effective" indenter geometry in contact with a flat surface.
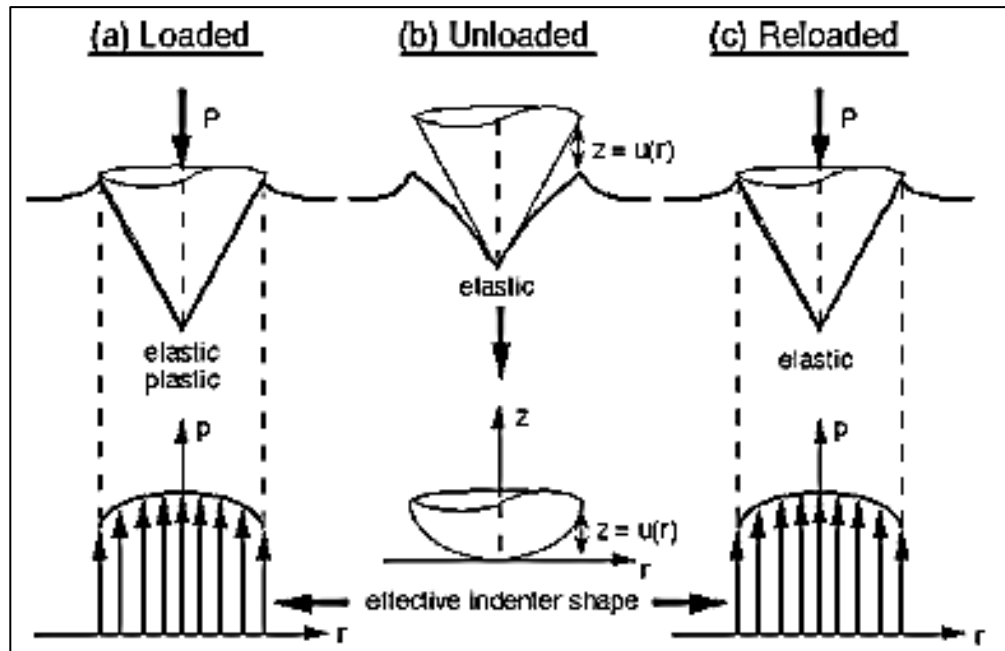
Figure 40: Figures demonstrating the effective indenter concept from Pharr and Bolshakov[150]

The effective indenter geometry can be described by the formula *z = u(r)*, where *u(r)* is the distance between the indenter and the elastically recovered unloaded surface as shown in the top part of Figure 40(b) and *r* is the radial distance from the central point of the contact. Finite element simulations found that the effective indenter geometry could be approximated by Equation 17, where *B* is a fitting constant and the coefficient *n* is dependent on the material tested.

$$z = Br^n$$

Equation 17

The coefficient *n* was found to relate to the power law fitting coefficient *m* as shown in Equation 18. Typical n coefficients were found in the range 2-6, corresponding to *m* coefficients in the range 1.2-1.5. *n* coefficients at the lower end of the range correspond to an effective indenter with the shape of

a paraboloid of revolution thus explaining experimentally observed fitting coefficients.

$$m = 1 + \frac{1}{n}$$

Equation 18

The time dependent effective indenter builds on the concept of the effective indenter geometry by considering the effect that time dependent depth changes would have on the effective indenter geometry. This means that during unloading the change in the shape of the deformed surface is now time dependent and not just load dependent. In order to properly describe the contact the effective indenter concept is extended into a time dependent effective indenter (TDEI). This analytical approach to the problem reduces the need for complex FE modelling by simplifying the problem.

The TDEI approach is built into the standard OPfC software and works in a similar way to that outlined in section 3.4.3. Load, depth and time data from nanoindentation experiments are imported into the OPfC software. The software then performs two fits to the unloading data. The first determines the shape of the time dependent effective indenter and the necessary time dependent fitting co-efficients m(t). The exact nature and derivation of this fit is proprietary and cannot be included in this thesis. The effective indenter fit is then used to find the Young's modulus of the sample. The Young's modulus is given in the form of a relaxation modulus as shown in Equation 19. This is consistent with solutions for the indentation behaviour of viscoelastic materials as derived by dimensional analysis.

$$E(t) = E0 + E1\exp(-t/\tau_R)$$

Equation 19

99

Where $\tau_R = \eta/E1$ is the relaxation time, with η the coefficient of viscosity represented by the dashpot in the three element constitutive model (see Figure 41). This model assumes a different standard linear viscoelastic material model to the one shown in Figure 37. In this model the material is assumed to behave as a Maxwell model in parallel with a linear spring. This model represents the superposition of the solid and fluid behaviour observed in viscous materials [151]
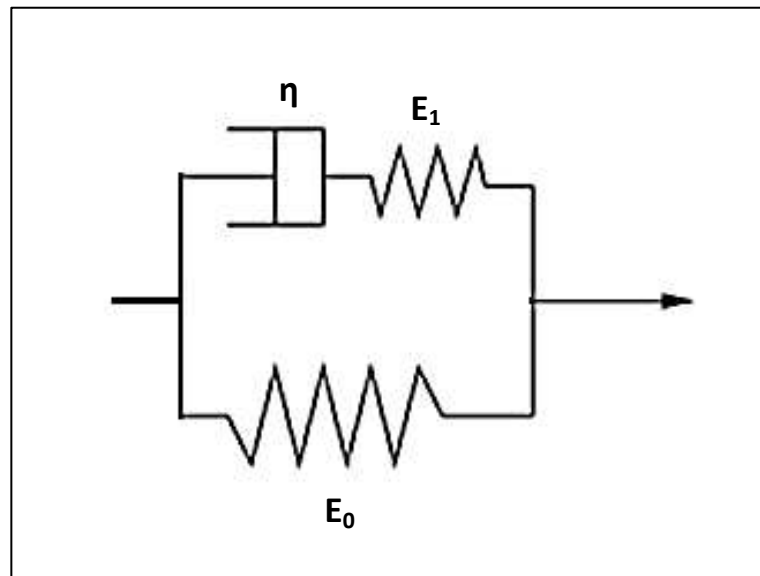
Figure 41: Standard linear viscoelastic material model used in TDEI analysis

The elastic modulus from the OPfC software is expressed in terms of a relaxation modulus. This reflects the fact that stresses will relax during the indentation changing the apparent mechanical response [143]. The overall effect of this is best evaluated by examining the two limiting cases for this equation. As t→0 i.e. for an infinitely fast experiment there is no time for stresses to relax during the indentation therefore the indentation response is the combination of the solid and fluid springs, E(t)=E0+E1. As t→∞ i.e for an

infinitely slow indentation the fluid component of the model goes to zero and the modulus is the same as a linear spring, E(t)=E0.

As previously stated this technique was initially developed to allow more accurate analysis of polymeric indentation data. For this reason the form of the output from the software is a relaxation modulus. This is only relevant for viscoelastic materials where the effect of the viscous recovery is expected to last the duration of the unloading period. For viscous deformation as observed in creeping metals at high temperature the similarity is the effect on the slope of the initial unloading data. Experimentally these very different deformation mechanisms will have a similar effect on the nanoindentation unloading data. In the case of the creeping metal this effect will disappear rapidly as the load is removed so care is needed when interpreting the results of this analysis applied to creep.

5.4.2 Time dependent effective indenter results

5.4.2.1 Polymeric materials

In order to give a single modulus value to compare to conventional analysis results a relaxation time of 10 seconds was selected. Analysed data is tabulated in Table 14. Correction of the polyamide nanoindentation results in this study using the time dependent effective indenter lower the modulus by around 27% compared to the standard analysis. As the data is corrected using a fit to the unloading data it does not introduce any artificial unloading rate dependency so that the corrected modulus is the same, within experimental error for both unloading rates studied. In addition to this Table 15 shows the corrected fit to the unloading as a result of the time dependent effective indenter correction. With the time dependent behaviour of the material accounted for the fit is now more representative of the contact between the

indenter and sample. The fitting co-efficient m(t) are now in the range more typical for indentation contact 1.2-1.5.

Table 14: Polymeric time dependent effective indenter results

Material	E0	E1	η	E(t)
PA 66	2.37 ± 0.20	2.34 ± 0.18	53 ± 12	2.50 ± 0.12
	2.49 ± 0.17	2.66 ± 0.13	41 ± 7	2.54 ± 0.15
PC	1.46 ± 0.03	1.50 ± 0.02	154 ± 8	2.29 ± 0.06

For Polycarbonate the conventional power law fitting coefficients are >2 and therefore outside the range of physical indentation contact. This again indicates that the viscoelastic behaviour is affecting the conventional indentation analysis. Correction using the time dependent effective indenter analysis drops the modulus by around 14% and the time dependent fitting confidents are now more representative of indentation contact.

Table 15: Polyamide fitting coefficients

Material	Unloading Rate mN/s	Conventional Oliver and Pharr fitting coefficient	TDEI fitting coefficient
PA 66	0.5	1.91 ± 0.01	1.34 ± 0.01
	0.25	1.89 ± 0.01	1.40 ± 0.01
PC	20	2.014 ± 0.007	1.453 ± 0.004

The degree of correction is less for the polycarbonate than the polyamide 66, this is as expected as the glass transition temperature of polycarbonate is

around 150°C. The degree of viscous deformation expected in polymeric materials is related to the proximity to the glass transition temperature. Therefore it is expected that the influence of viscoelastic deformation on conventional indentation analysis and therefore the degree of correction required should be greater for the polyamide 66.

The SIO software also has the capability to examine stresses in experiments using sharp indenters. Figure 42 shows the stress distribution from a 5mN indentation on the polyamide 66 sample at peak load, the z axis in the plot is the indenter axis. The plot represents the stress field for half of the indented region, the stress field is assumed to be symmetrical about the indentation axis. The indenter is represented by the grey triangle at the top of the plot. The x axis is the direction perpendicular to the indentation axis. The stress distribution shown in the von Mises stress evaluated at different points in a connected mesh in the indented region. The peak von Mises stress at the start of the dwell period is ~155MPa with the stress field extending around 15µm into the sample.

Figure 43 shows the stress field from the same indentation at the end of the 60s dwell period. The peak von Mises stress has fallen to ~120 MPa and pervades ~10µm into the sample. In polymeric materials most of the stress relaxation is due to viscoelastic deformation which continues during unloading.
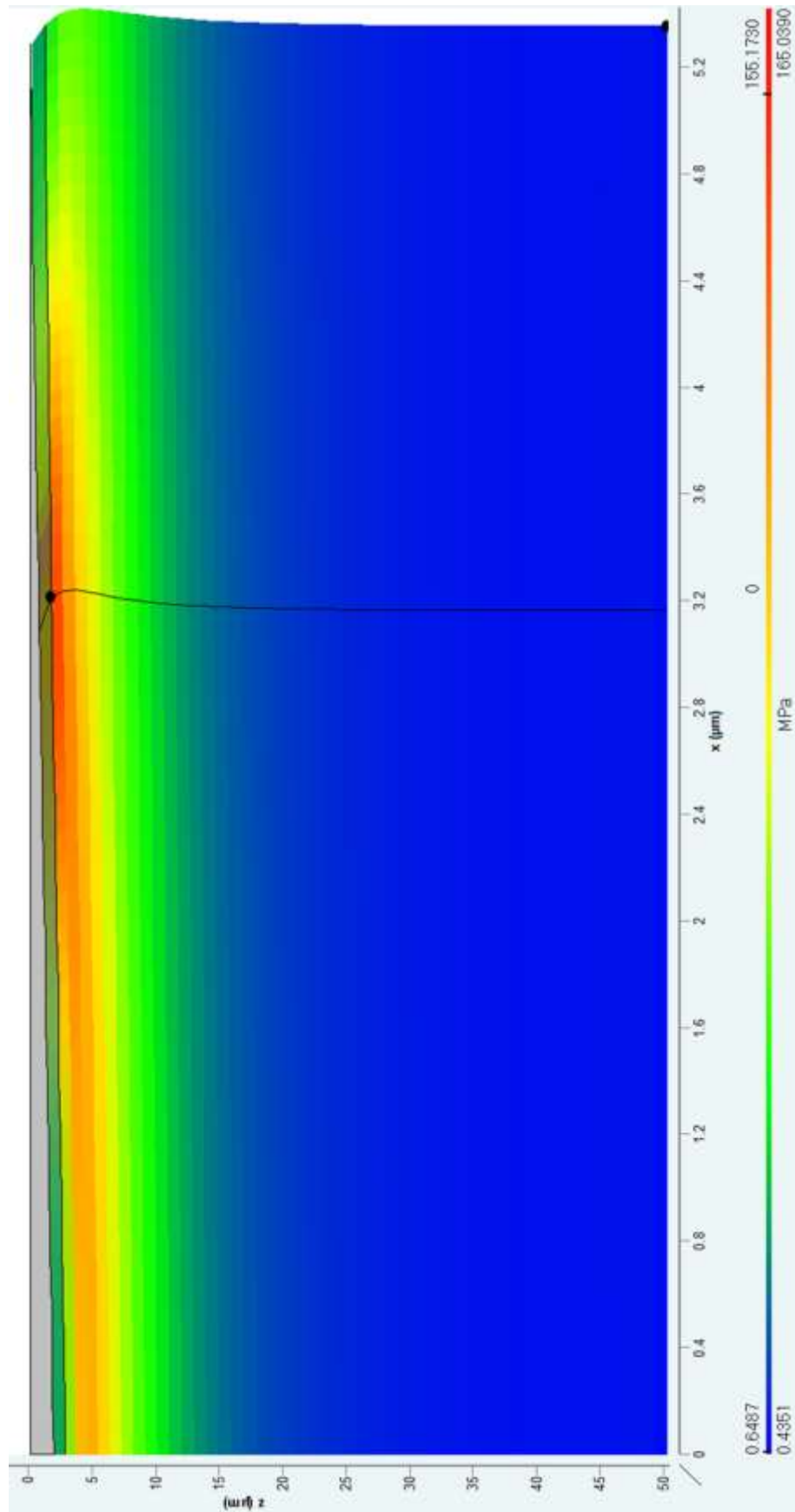
Figure 42: Stress distribution in PA66 at peak load
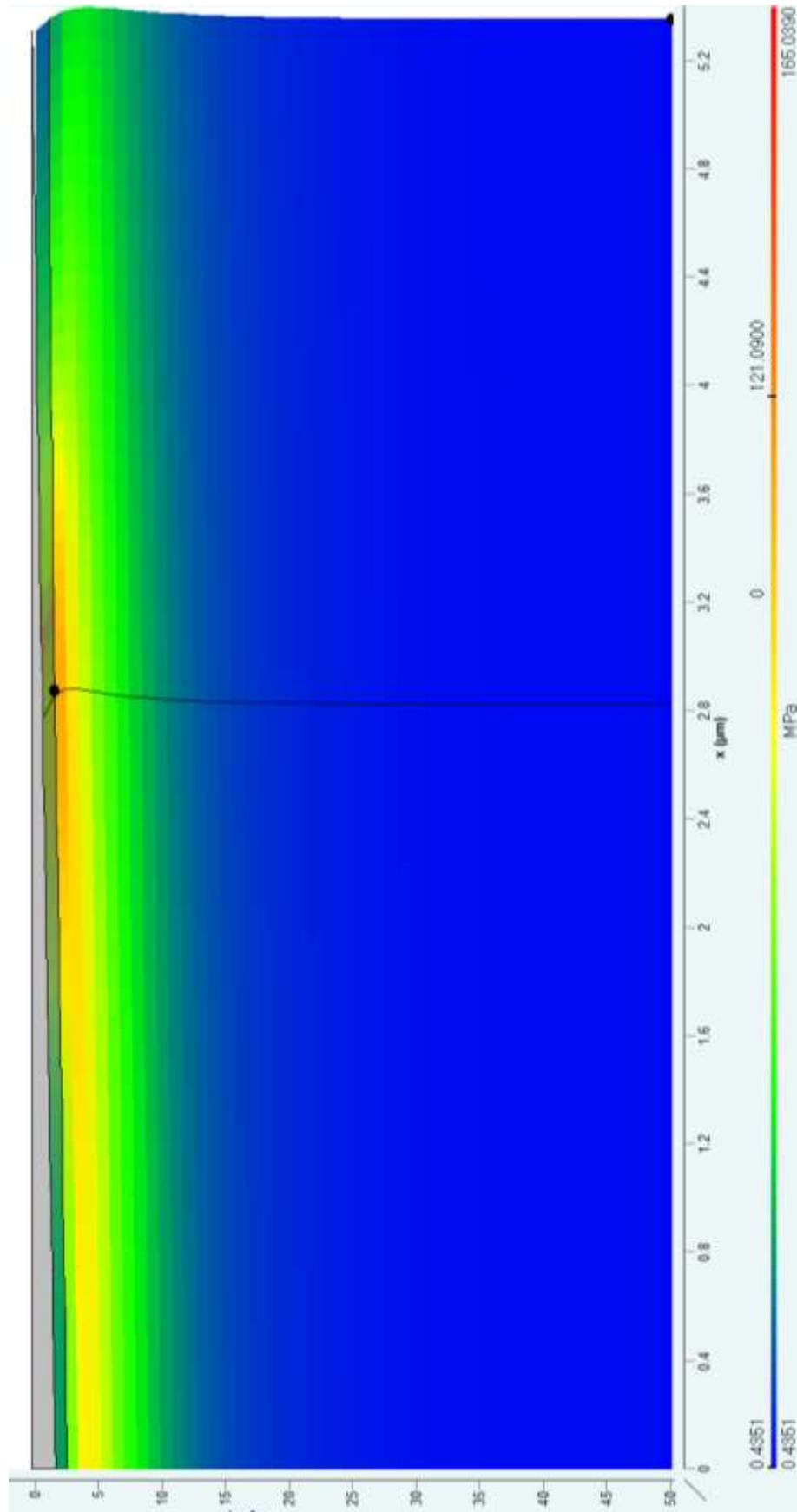
Figure 43: Stress distribution in PA66 at the end of the dwell period

5.4.2.2 P91 Steel

Table 16 shows the fitting coefficients for the conventional fit to the P91 parent and weld data, the fitting coefficients for both samples are outside the physical range relating to the contact in nanoindentation testing (1.2<m<1.5). In fact in both samples over 90% of the fitting coefficients from the conventional analysis are greater than 2. This suggests that time dependent depth changes are having a large effect on the validity of the conventional fit to the unloading data.

Table 16: P91 steel fitting coefficients

Material	Unloading Rate mN/s	Conventional Oliver and Pharr fitting coefficient	TDEI fitting coefficient
PM	10	2.50 ± 0.06	1.12 ± 0.01
WM	10	2.66 ± 0.08	1.23 ± 0.02

The time dependent effective indenter analysis similarly corrects the artificially elevated Young's modulus bringing the calculated values in line with those predicted by previous measurements using other techniques. Critically when analysed using the time dependent effective indenter technique both the parent and weld material return the same modulus.

In addition to this the corrected fit to the data now has fitting coefficients which are much more repeatable and all within the physical limits expected for conventional nanoindentation contact. This indicates that the time dependent effective indenter fit is a much more valid fit to the unloading data for materials exhibiting time dependent behaviour.

Table 17: P91 Time dependent effective indenter results

Material	E0 GPa	E1 GPa	η	E(t) GPa
PM	1 11 ± 5	147 ± 30	19 ± 3	111 ± 5
WM	117 ± 11	136 ± 24	10 ± 4	117 ±11

Figure 44 shows the von Mises stress distribution on P91 parent material at peak load for a 200mN indentation. The maximum stress is ~1.08GPa with the stress field extending ~17µm into the sample. The indentation depth in this case was ~1.5µm so the stress field in the P91 parent extends approximately 11 times deeper than the indent depth.

Figure 45 shows the stress distribution at the end of the 30s hold period on P91 parent material. By the end of the dwell period the peak stress has fallen to just 700MPa with the field extending 12µm into the sample. In the steel the viscous deformation mechanism differs from the polymeric materials tested as the depth change at peak load is due to creep and there is very little viscoelastic recovery during the unloading period.
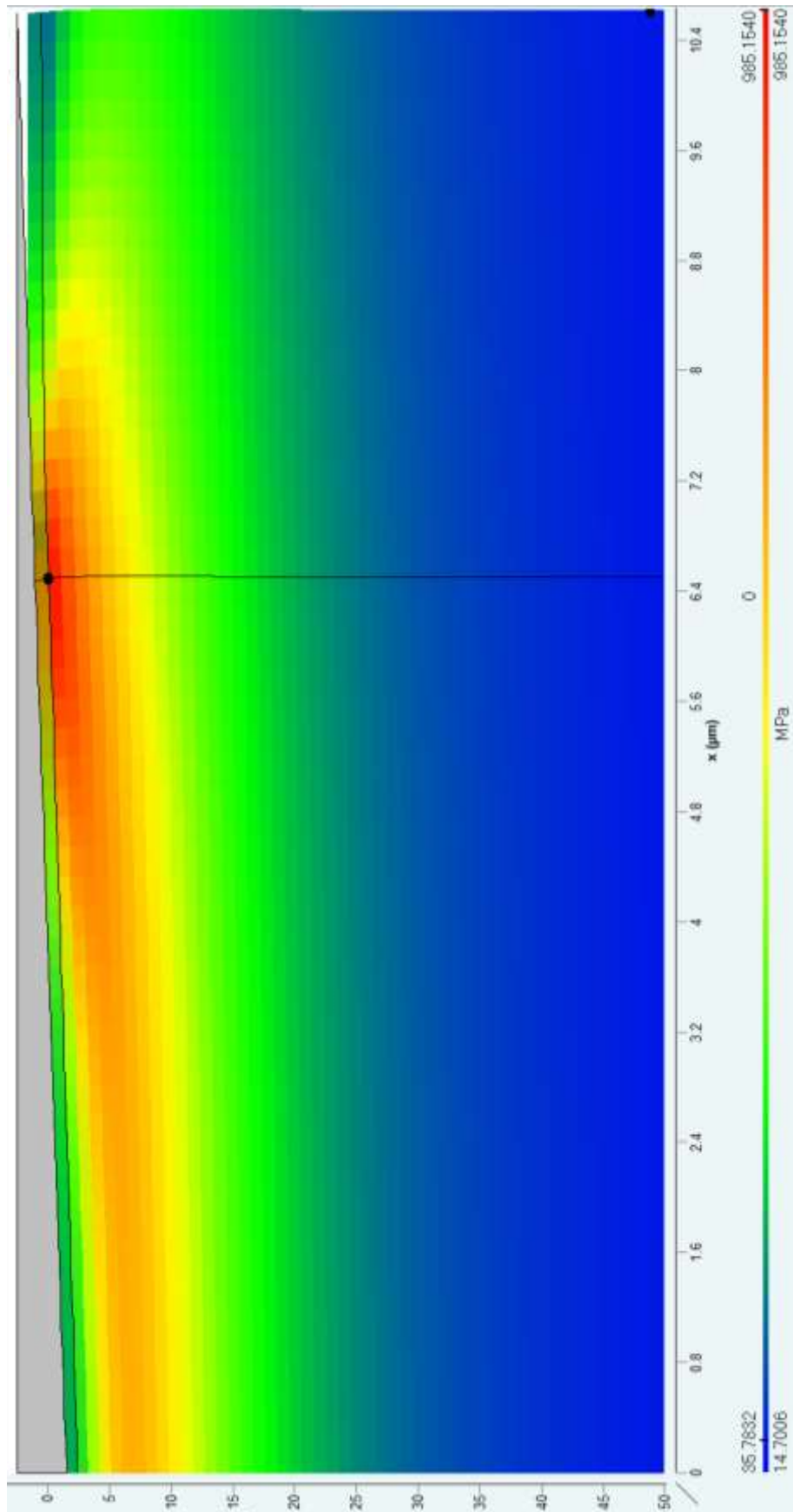
Figure 44: P91 stress distribution at the beginning of the dwell period
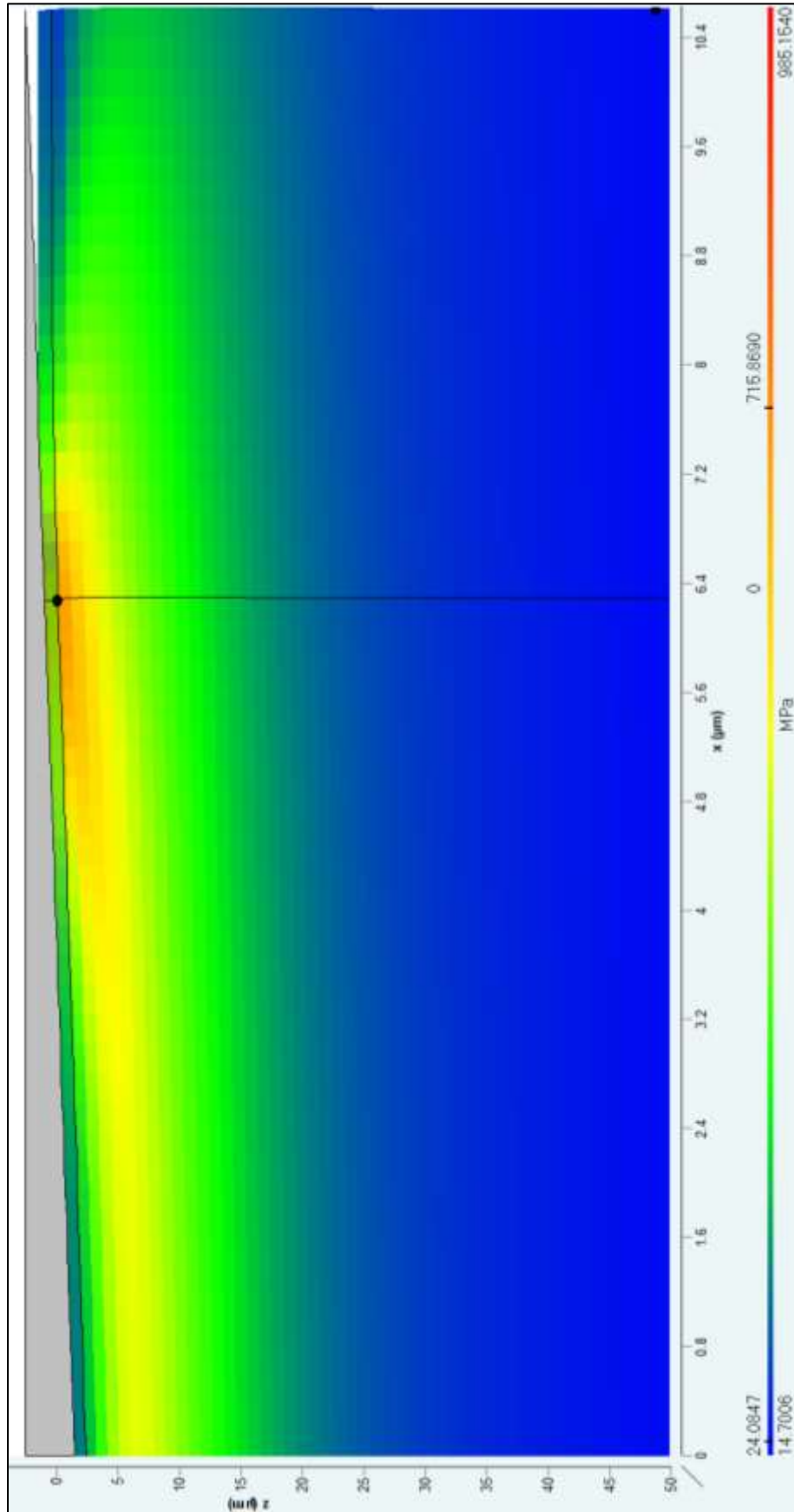
Figure 45: P91 650°C stress distribution at the end of the dwell

Unlike the polymer samples the results for the P91 steel are dominated by the E0 term in the linear viscoelastic solid model. This is due to the higher η, coefficient of viscoscity values seen in these results. This is expected as the viscous deformation of this material decays rapidly as the load is removed and there is very little viscoelasticity as reflected by the short relaxation time for this material. The key benefit for examination of viscous metals is that the more accurate fit to the unloading data gives much more reliable modulus values by removing the influence of the high creep rate at the end of the dwell.

5.5 Summary

Three different analysis techniques have been used to evaluate the Young's modulus of sample expected to exhibit a degree of viscous behaviour. The influence of the viscous behaviour on the fit to the unloading data has been examined. Conventional techniques utilising long dwell periods have been used to allow the viscous deformation rate to relax sufficiently before unloading. This approach is successful but requires very long dwell periods to allow sufficient relaxation. For this reason other techniques which have been developed to correct unloading data affected by viscous deformation were studied.

Firstly the application of the existing empirical creep compliance correction technique to correct the effects to time dependent deformation has been examined. This correction assumes that the creep rate during unloading and therefore its influence of the calculated modulus is the same as the creep rate at the end of the dwell period at peak load. It does not take into account the fact that the creep rate will change as the stresses are reduced during unloading. As a result the creep compliance correction tends to over correct the modulus as seen for the P91 parent material or as in the polyamide 66 sample overestimate the unloading rate dependency in the analysis results.

Correcting time dependent displacements in nanoidentation analysis

Secondly the time dependent effective indenter correction which uses a fit to the experimental unloading data to correct the time dependent effects has been examined. The correction is therefore responsive to the change in creep rate as a result of the reduced stresses during unloading. As a result the correction made to the data gives the same modulus value regardless of unloading rate so no additional rate dependency is introduced to the data. The fitting procedure is also robust enough to be applied to creeping materials where the deformation rate drops rapidly once the load is removed. In this case the key is the improved fit to the unloading data which compensates for the effect on the initial unloading data without over correcting. As P91 is not viscoelastic attempting to determine the properties in the form of a relaxation modulus has little relevance. This is confirmed as there is virtually no contribution from the second spring in the three element model to the modulus. The very fast relaxation time seen in these results confirm that the time problem is due to high creep rates at the end of the dwell affecting the initial unloading slope. An effect which quickly disappears as the load is removed.

Chapter 6 - Nanoindentation characterisation of P92 steel

6.1 Introduction

Following on from the characterisation of the P91 weld material it was decided to attempt to use nanoindentation to characterise another power station grade steel in order to try to identify if this technique could be practical for more general use focusing on one of the next generation of power station materials. This was worthwhile given that this technique has been shown to give variable results from one material to the next when compared with conventional uniaxial data [98]. Testing on P91 steel showed a higher degree of correlation than expected therefore, in order to assess the general applicability of the technique, a material with known creep behaviour different to P91 was needed. The material selected for testing was P92 steel (ASME P92). P92 is a relatively new development in the search for high creep resistant steel having a higher long term creep rupture strength than P91 steel [12].

6.2 Results

All error bars are ±2 standard error unless stated.

6.2.1 Room Temperature characterisation

As with the P91 steel experiments on P92 began with a room temperature characterisation of the parent and weld material in order to provide a reference point for the high temperature nanoindentation measurements. Experimental parameters selected were exactly as used for the experiments on P91, i.e. 20s load/unload and a 20s dwell at peak load.

Table 18: P92 room temperature nanoindentation results

	Hardness GPa	Reduced modulus GPa	Young's modulus GPa
PM	3.69 ± 0.07	218 ± 3	246 ± 4
WM	4.21 ± 0.11	233 ± 6	267 ± 9

The results of the room temperature experiments are shown in Table 18. As for the P91 steel, the parent and weld of the P92 have exactly the same modulus. Interestingly, again the Young's modulus is higher than values previously reported for P92 steel. The hardness of the P92 weld is higher than the parent as it was for P91, this is expected as the weld has been found to be overmatched to the parent [152] [153]. As previously discussed the hardness values are slightly higher than literature measurements made using Vickers hardness testers. This is due to the inability of depth sensing indentation to account from the material displaced by the indenter piled up above the initial contact surface which is still supporting some of the applied load.

Post indentation SEM imaging confirms the presence of this piled up material. Figure 46 shows an indentation in the P92 parent material, an indentation on a material that does not pile up should be a regular shape with flat edges following the geometry of the Berkovich indenter. The indentation in the figure has apparent irregular edges due to the piled up material, the highlighted region of the figure shows material along the edge of the indentation which is raised above the initial surface.

113
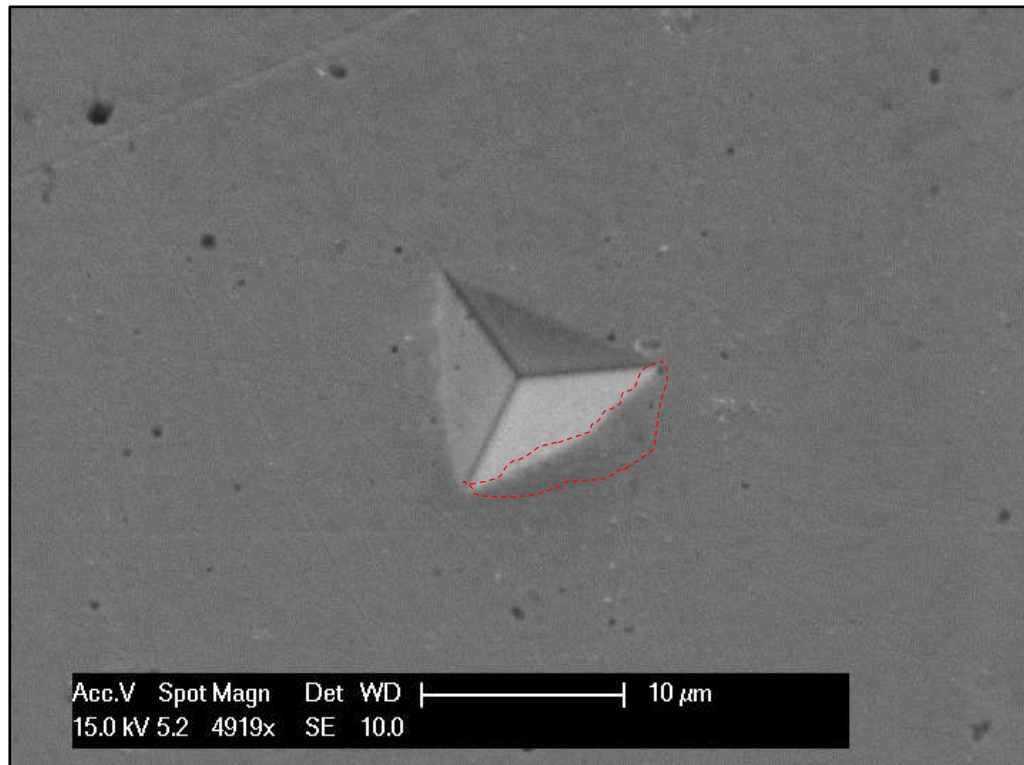
Figure 46: SEM image of a room temperature indentation in P92 parent material

As stated, tests on bulk parent and weld material have previously been performed using macro scale measurement techniques. One of the benefits of nanoindentation is the potential to find the mechanical property determinations with a very small pitch between measurement positions. This was utilised in order to look at the change in mechanical properties as a result of the change in parent material grain size through the heat affected zone of a weld cross section. As the location of the fusion line of the HAZ samples had been accurately located it was possible to place lines of indentations on a much finer pitch than conventional micro-scale tests. An example of this kind of experiment is shown in Figure 47, in the example the pitch of the indentations is around 50µm.
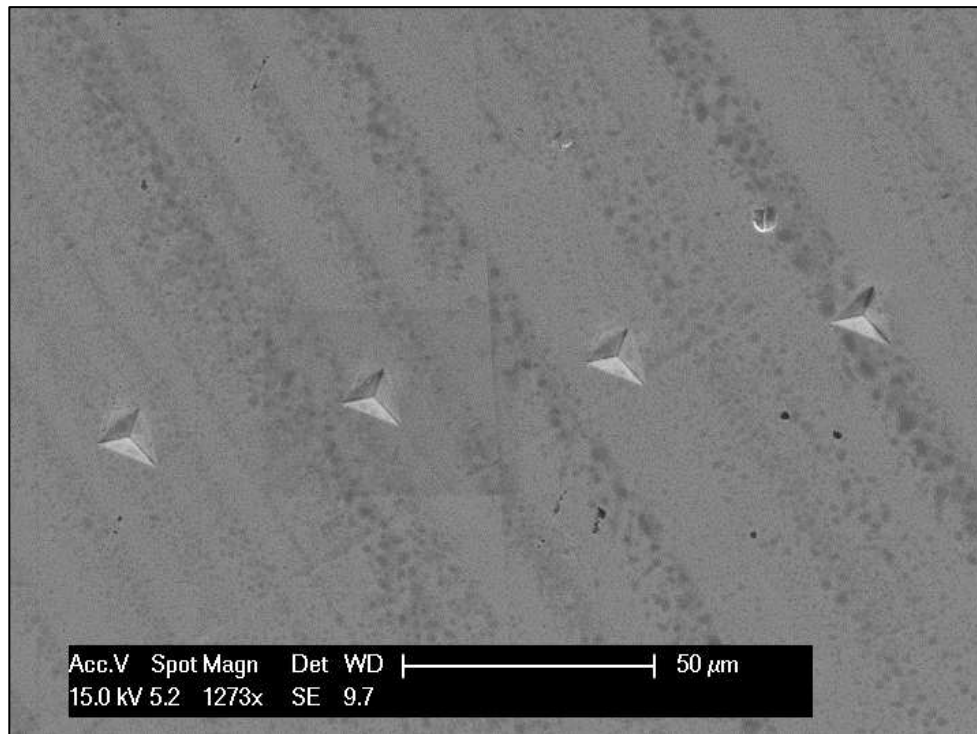
Figure 47: SEM image of a line of indentations across P92 HAZ

The hardness results from a line of indentations at 50 μm intervals across the HAZ are shown in Figure 48 the position of the fusion line is highlighted by the dotted line in the figure. As expected the change in grain size as a result of heating during welding leads to a change in the hardness across the heat affected zone. The change in the properties of the parent start approximately 3mm from the fusion line, after this point the hardness drops corresponding to the increase in the grain size for the large grained region of the HAZ closer to the fusion line, the hardness increases as the HAZ becomes finer grained and the hardness increases. The region of higher hardness on the left hand side of the figure corresponds to the weld material which, as previously mentioned is overmatched to the parent material. This change in hardness with microstructure is consistent with those previously reported in literature for P92 steel heat affected zones [154, 155].
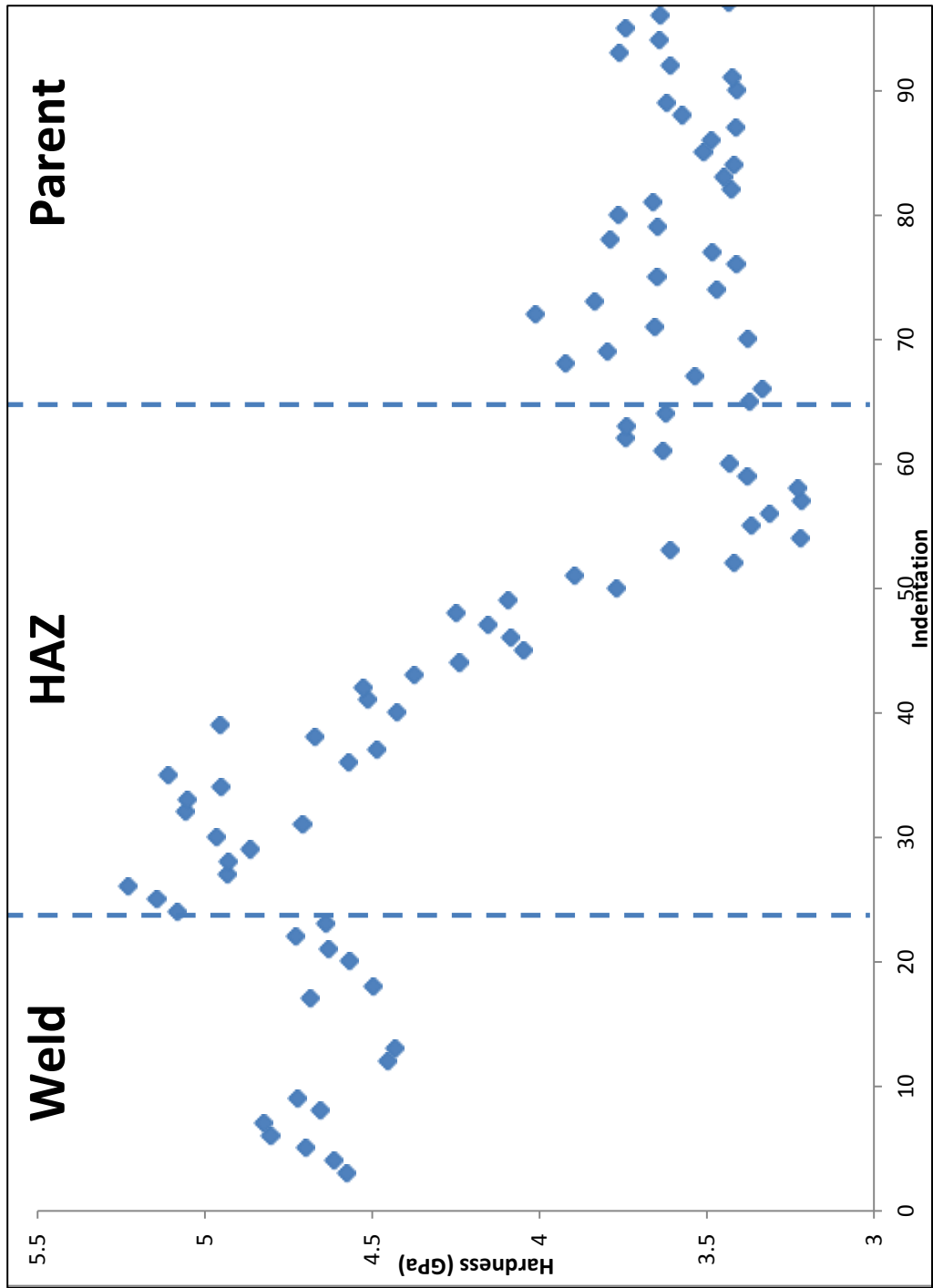
Figure 48: Room temperature P92 HAZ hardness

Figure 49 shows the reduced modulus determined from the same set of indentations across the HAZ. As expected the change in grain structure has no effect on the stiffness of the material, the average of the reduced modulus over the measured region is 231 ± 3 GPa the same as the value from the bulk parent and weld material.
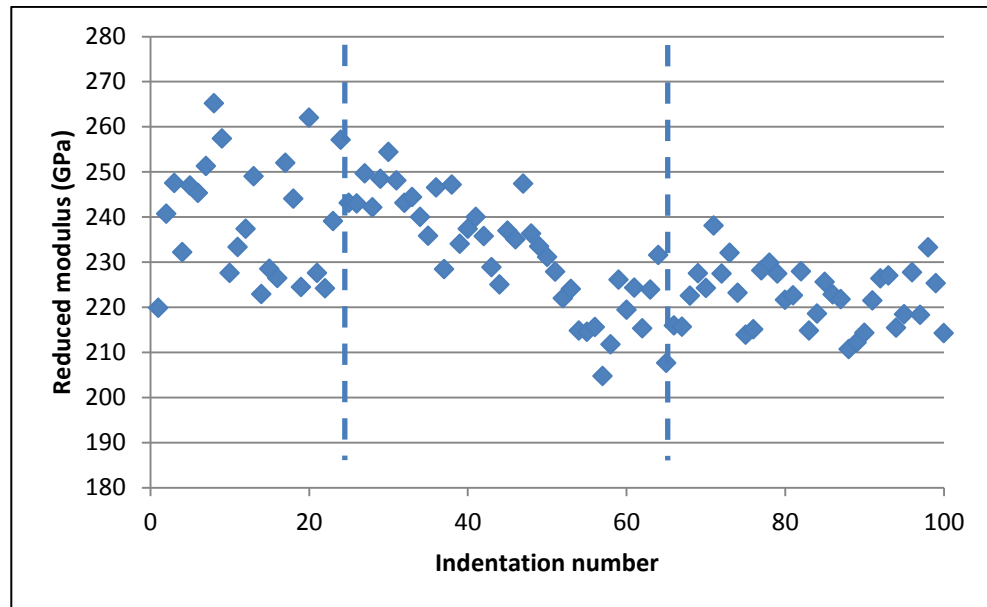
Figure 49: Room temperature P92 HAZ modulus

6.2.2 P92 Characterisation at 675°C

Similar to the process followed at room temperature, characterisation at elevated temperature began with finding the properties of the bulk materials. Experimental parameters selected were the same as used at room temperature, 20s load/unload etc. However in order to allow the creep rate to slow sufficiently to minimise the effect on the unloading data, a 300s hold at peak load was used. The results of this testing at 675°C are shown in Table 19, in order to check that sufficient peak load relaxation time had been allowed the data was analysed using the creep compliance correction method detailed in section 5.3.2. As described in section 5.3.1 the most commonly used method for indentation of creeping materials is to use a longer hold period. In this case 300s appears to be sufficient as, unlike the P91 steel, the correction only makes around 7% difference to the modulus in the most

117

extreme case. This is for the 100mN data where the creep rate at the end of the dwell period was typically around 0.5nm/s. As the difference was less than the standard deviation of the measurement no further corrections were applied to the P92 data. The standard treatment of using long dwell periods was deemed to be sufficient in this case. The hardness found by nanoindentation is in line with results from conventional hot hardness testing which report a hot hardness of around 0.9GPa at 675°C [153].

Table 19: P92 High temperature properties

	Load mN	Hardness GPa	Reduced modulus GPa	Young's Modulus GPa	Creep Compliance Modulus GPa
PM	100	0.86 ± 0.09	94 ± 8	97 ± 10	94 ± 9
	50	0.92± 0.15	108 ± 11	115 ± 13	107 ± 11

Measurements were also made to characterise the heat affected zone at 675°C. Again this was done by making lines of indentations across the HAZ. Indentations were placed 100 μm apart. Following the experiments room temperature SEM was used to confirm the position of the indentations. The image in Figure 50 shows a line of indentations made at 675°C across the heat affected zone of a P92 weld.
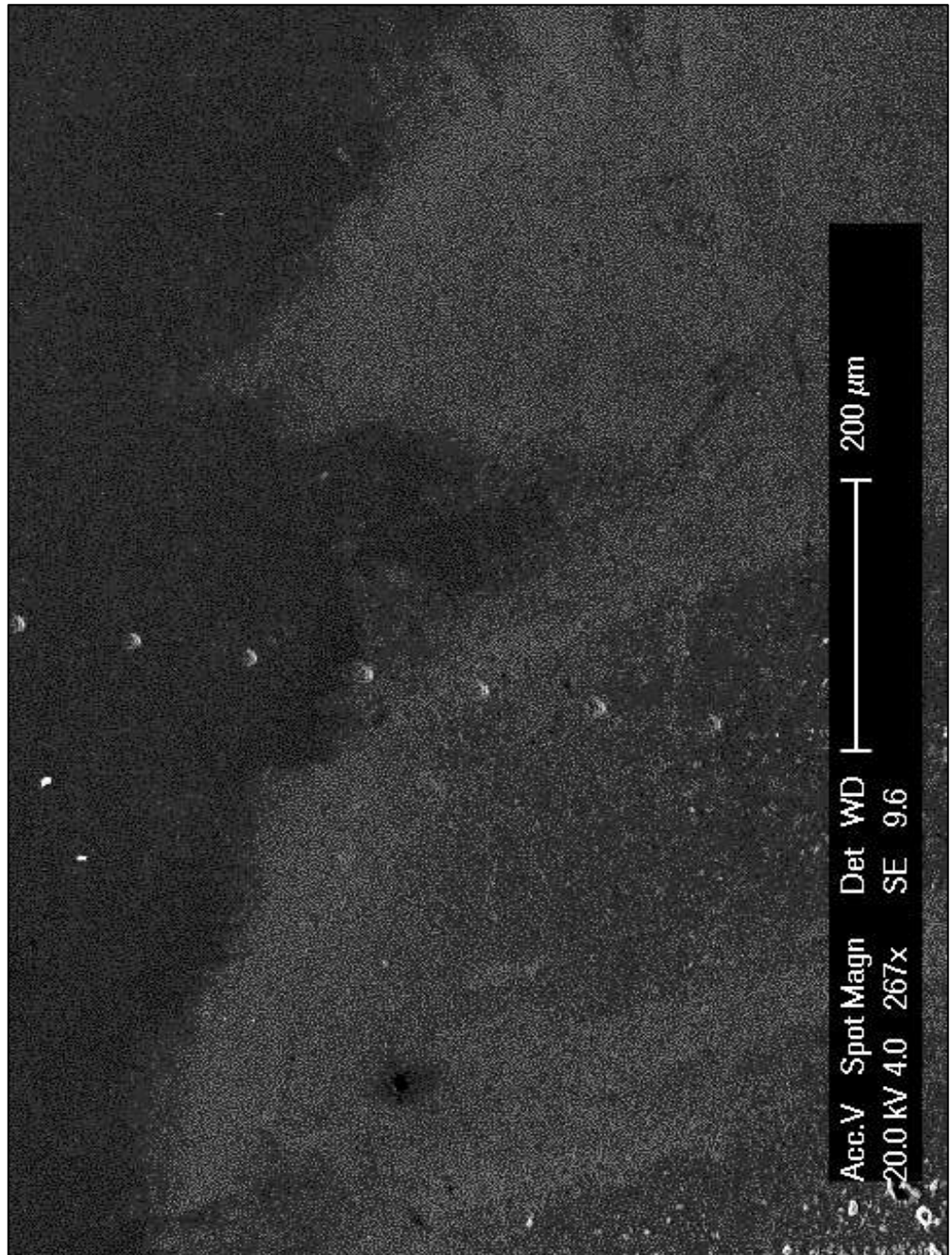
Figure 50: P92 indentations across HAZ post 675°C testing

Nanoindentation characterisation of P92 steel

One of the aims of using SEM to examine the samples post test was to examine closely the microstructures characterised by each indentation. However as mentioned in the methodology section, the,environmental chamber is only capable of reaching oxygen levels slow enough to slow the rate of sample oxidation not stop it completely. Therefore by the time the sample has been heated, tested then cooled, quite a significant oxide layer had formed on the sample surface making micrstructural characterisation difficult. P92 steel is designed to be oxidation resistant so only a thin oxide layer forms, however it is sufficient to hide the microstructure and any attempt to remove the oxide will also remove the residual indentation crater. Typical sample oxidation is shown in Figure 51 at two magnifications,at 9143x magnification it is possible to see the classic iron oxide formations around the indentation sites.
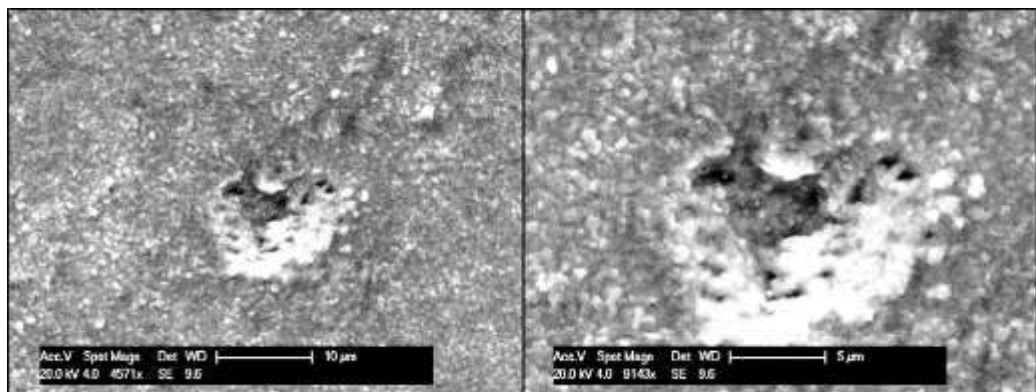
Figure 51: P92 Indentation oxidation post testing at 675°C

Despite the obvious oxidation after the sample had been tested at 675°C, there is no obvious oxide layer effect on the indentation data. Typical indentation curves from the heat affected zone are shown in Figure 52. As described in the methodology section 3.3.1, if there was a significant oxide layer we would expect to see a rapid depth increase at the start of the loading curve. This indicates that much of the oxidation occurred after the indentation experiments had been completed or that the oxide layer was too brittle to affect the nanoindentation data. However, as with the P91 it is possible that

120

the oxide layer is having a more subtle effect on material properties and again further examination of the oxidation rate could be used to more accurately evaluate this. The three curves shown are from different locations through the HAZ, the different indentation depths are indicative of the change in hardness as a result of the changing microstructure.
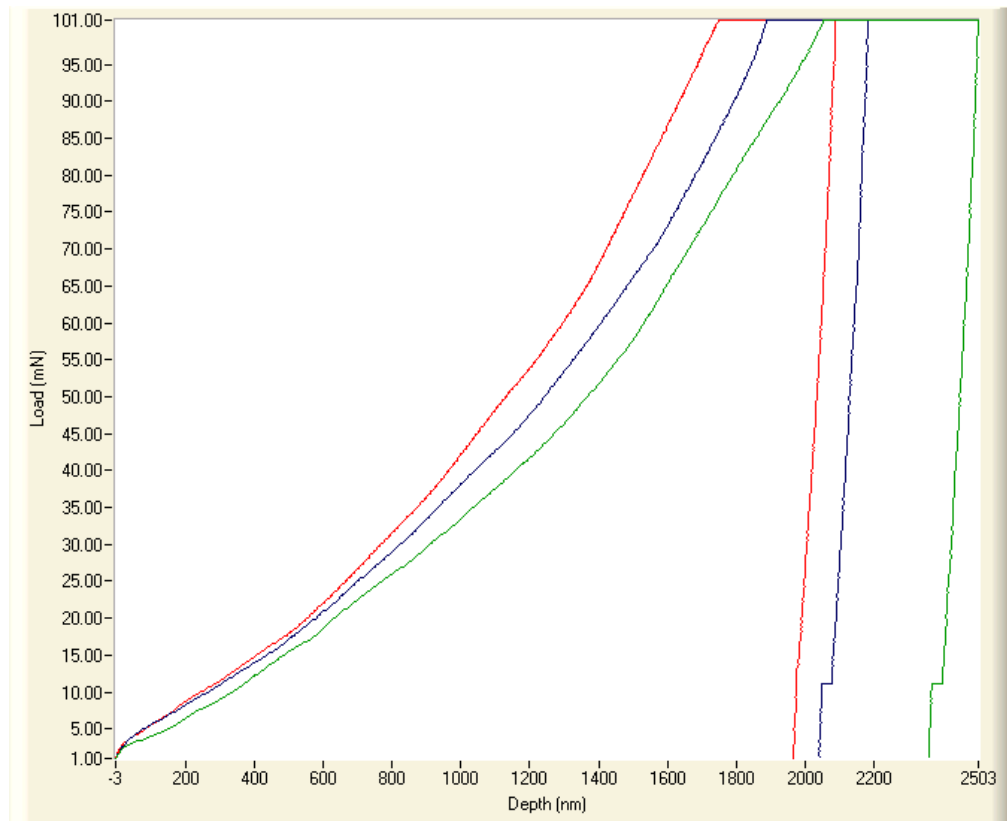
Figure 52: Typical P92 HAZ indentation data at 675°C

Modulus results from the indentations made across the HAZ are shown in Figure 53. As with the room temperature experiments, the change in microstructure through the heat affected zone has no effect on the calculated modulus. The average modulus value across the HAZ was 104 ± 14 GPa in line with the values calculated for the bulk parent material sample at 675°C.
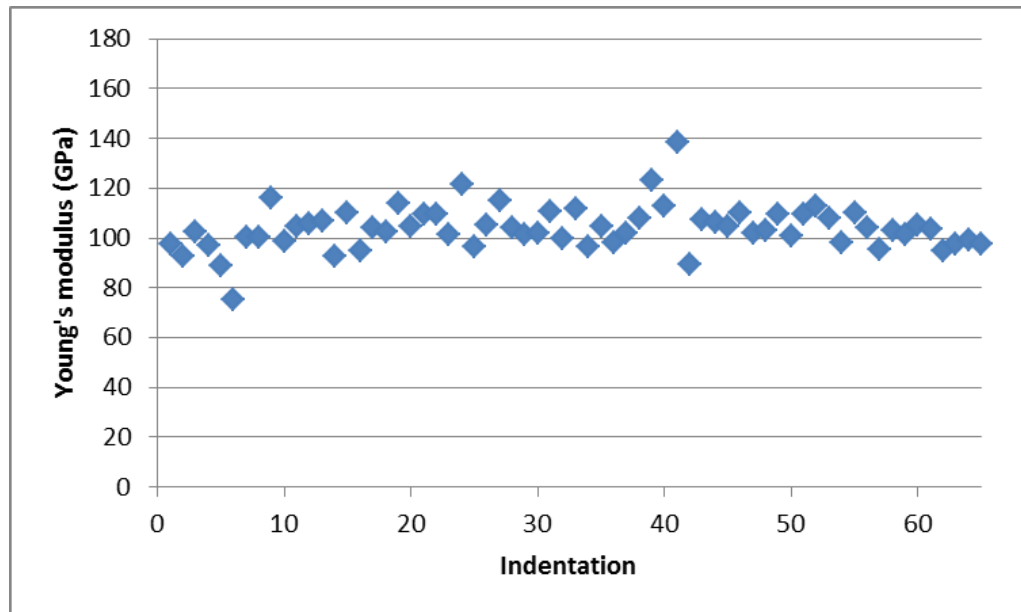
Figure 53: P92 Young's modulus across HAZ at 675°C

Figure 54 shows the hardness measurements for the same data analysed in Figure 53. As at room temperature, there is a drop in the hardness moving away from the heat affected zone. At 675°C though the difference between the hardness of the unaffected parent material and the least hard region of the heat affected zone is significantly less than at room temperature. This is reasonable as the welded section will reach high temperatures during welding [8]. Therefore any additional heat treatment i.e. heating to 675°C would not be expected to have any additional effect on the microstructure of this region.
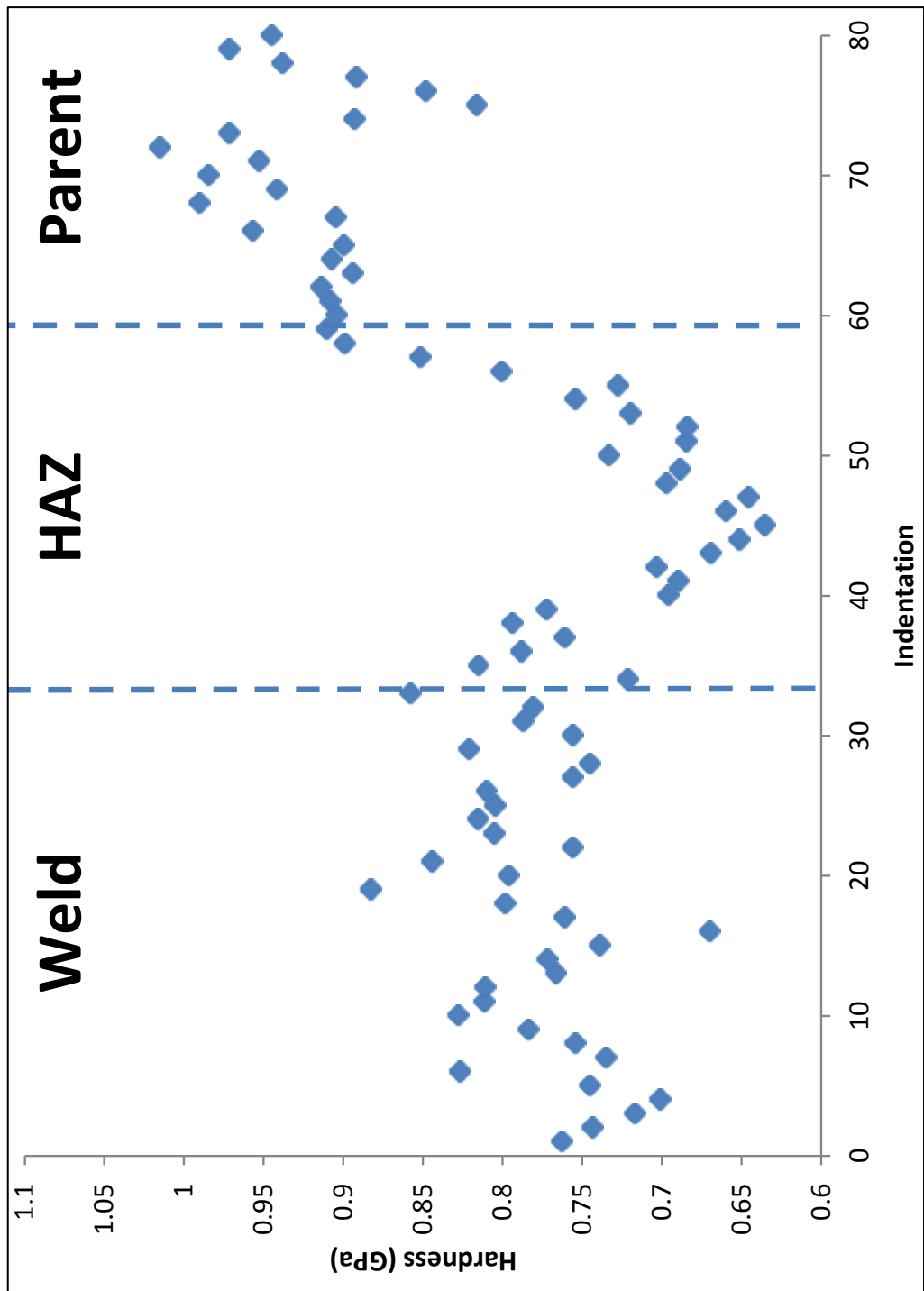
Figure 54: P92 HAZ hardness at 675°C

6.2.3 Nanoindentation creep testing

Figure 55 shows a typical set of creep stress and strain data from the parent material at 675°C. As stated in the methodology section, the creep stress exponent is taken to be the gradient of a fit to this stress strain data. The nanoindentation creep analysis method generates many stress strain data from a single creep hold but can be sensitive to slight thermal fluctuations in the raw data. This can be seen in the data in Figure 55 in the ringed section. These data do not represent any one particular time in the test when the creep rate was low but rather isolated measurements for which this was the case most likely as a result of thermal fluctuations. The benefit of the generation of so many data from a single curve is that these data have little effect on the overall measurement.
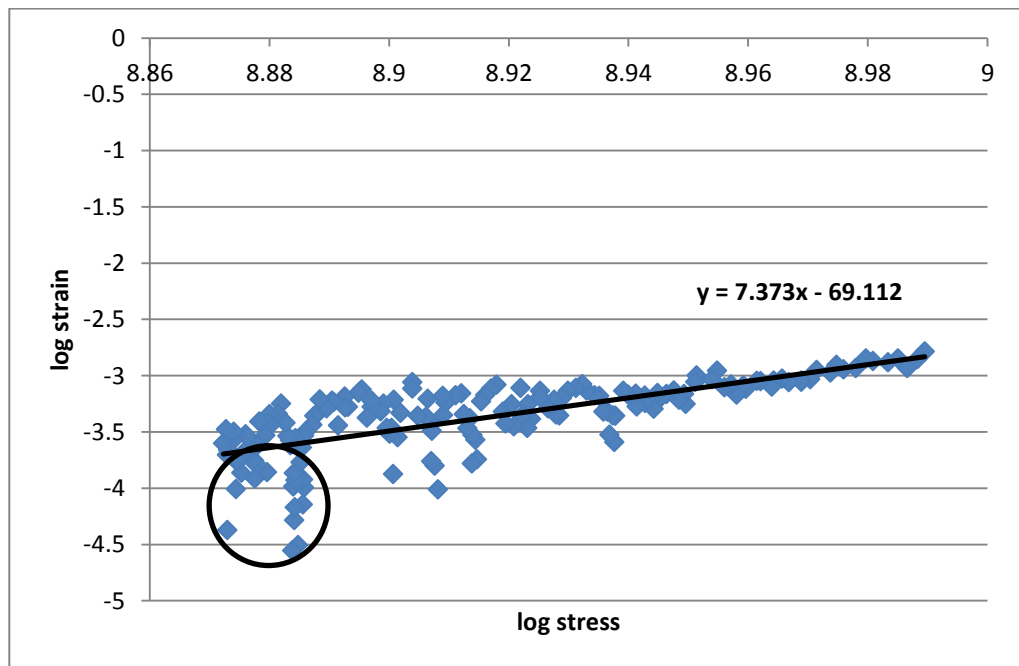
Figure 55: Typical 100mN P92 nanoindentation creep test stress strain data

Table 20 shows the creep exponents from indentation creep measurements in the bulk parent material sample. There is no significant difference between the stress exponents calculated at each indentation load. Both agree with previous determinations of the stress exponent from uniaxial creep data from testing at 675°C which report a creep exponent 0f 7.659 [8].

Table 20: P92 parent material indentation creep stress exponents at 675°C

Material	Test Load	Stress exponent
PM	50	7.9 ± 0.5
	100	7.3 ± 0.7

The yield stress for P92 steel would be expected to be as P91 steel since the dislocation density is roughly the same (~7x10^{14}m^2)[12]. As with the creep data the indentation creep test data was analysed using the SIO software in order to evaluate the stresses under the indenter at peak load [118]. Figure 56 shows the stress distribution at the start of the dwell period for a creep test on the P92 parent material at 50mN maximum load. For this test the maximum stress was 225MPa, which is around the yield stress of the P92. On the left hand side of the image are two plots which show the stress level on axes centering on the point of maximum stress. As with tests on the P91 steel, the majority of the material in the stress field is at much lower stress and therefore on average the indented volume is within the stress level of conventional uniaxial creep tests.

Previous testing on P92 at 650°C indicates that there is a threshold stress above which the deformation mechanism changes. Below 110MPa the creep stress exponent was reported as 6 rising to 16 above this threshold [156]. The results of the indentation creep test indicate that the bulk of the material is at stress lower than 110MPa, this is confirmed by the modelling software which indicates the bulk of the material is at stresses below 110MPa, suggesting that it is this material which dominates the indentation creep measurements.
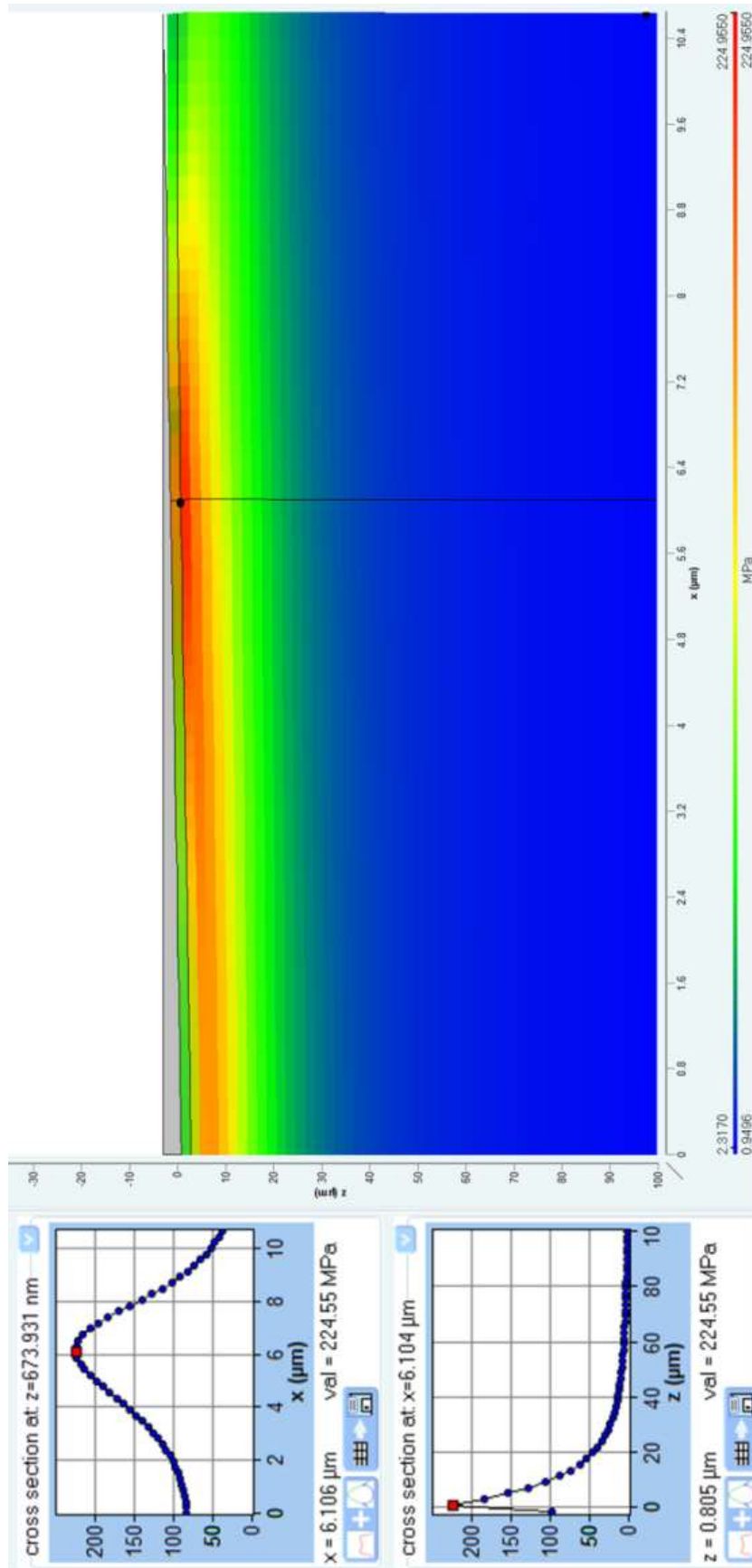
Figure 56: P92 PM 50mN nanoindentation creep stress

The mean sub grain size of P92 is similar to that of P91 at 0.35-0.42 µm with a grain size around 10-15 µm. The 50 mN creep tests which went to an average depth of around 1.5 µm with a width of approximately 11 µm, could therefore fall within a single grain. In P92 the key factor limiting the creep rate is the grain size of the sub grains and the $M_{23}C_6$ carbides which form at the grain boundary. Therefore due to the indentation creep experiments covering many subgrains it was assumed that this could be considered equivalent to the behaviour observed in larger scale tests. The same is true of the 100 mN tests which went to an average depth around 2.3 µm, meaning an impression width around 16 µm.

As expected the increased indentation load leads to higher stresses during the creep hold. An evaluation of these stresses is shown in Figure 57. Again a cross section has been taken of the plot with axes centred on the point of peak stress. The peak stress in the test shown was around 320MPa. However as with all indentation creep tests, the stress field is complex with a high peak stress rapidly falling to lower levels. As a result the stresses experienced by the bulk of material in the affected region are much lower. It also important to note again that these stresses are likely to be overestimates as one of the simplifying assumptions of the model is that there is no piled up material supporting load, which is not the case in indentation on most metals.
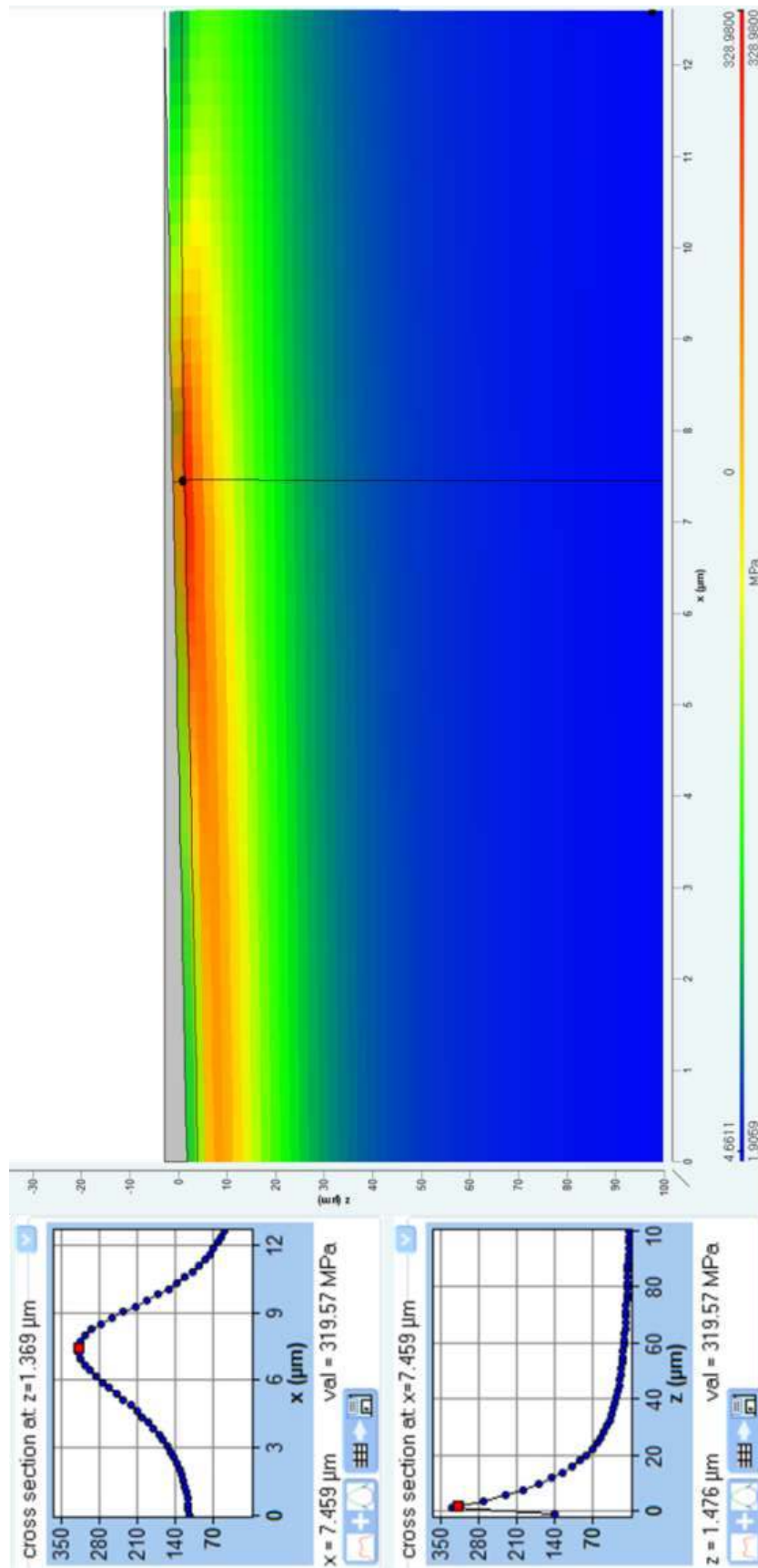
Figure 57: P92 PM 100mN nanoindentation creep test stress

Nanoindentation characterisation of P92 steel

Tests on the parent material were run to establish whether the indentation creep technique could again replicate results of conventional uniaxial tests. The main focus was to establish whether indentation creep testing could be used to characterise the change in creep behaviour across the heat affected zone. In order to do this, lines of creep test experiments were performed starting from the fusion line moving into the heat affected zone. Indentations were placed 100 µm in order to cover as much of the heat affected zone as possible before the oxide layer on the sample started to affect results.

A typical set of indentation creep exponents from across the heat affected zone is shown in Figure 58. The dotted line in the figure shows the position of the fusion line confirmed by post testing microscopy. The load used in these experiments was 100mN. Data from indentations with a thermal drift greater than 0.3nm/s have been removed from the plot as this level of drift affects the calculated creep exponent despite the correction sometimes returning negative exponents. There is a significant degree of scatter in the measurements making it difficult to identify trends in the data as seen in the hardness measurements. Interestingly though the creep exponents calculated from the data from the heat affected zone are all lower than the values found for the unaffected parent material. There are some indentations with stress exponents higher than the general trend, these may be erroneous measurements or may be due to some part of the microstructure but as post indentation microstructural characterisation was not possible it is difficult to be sure. The lack of microscopy makes it difficult to identify changes in creep behaviour across the fine grained and coarse grained region of the heat affected zone. The average creep exponent measurement across the full measured region of the heat affected zone is 4.4 ± 0.7 indicating a different deformation mechanism to the parent material.
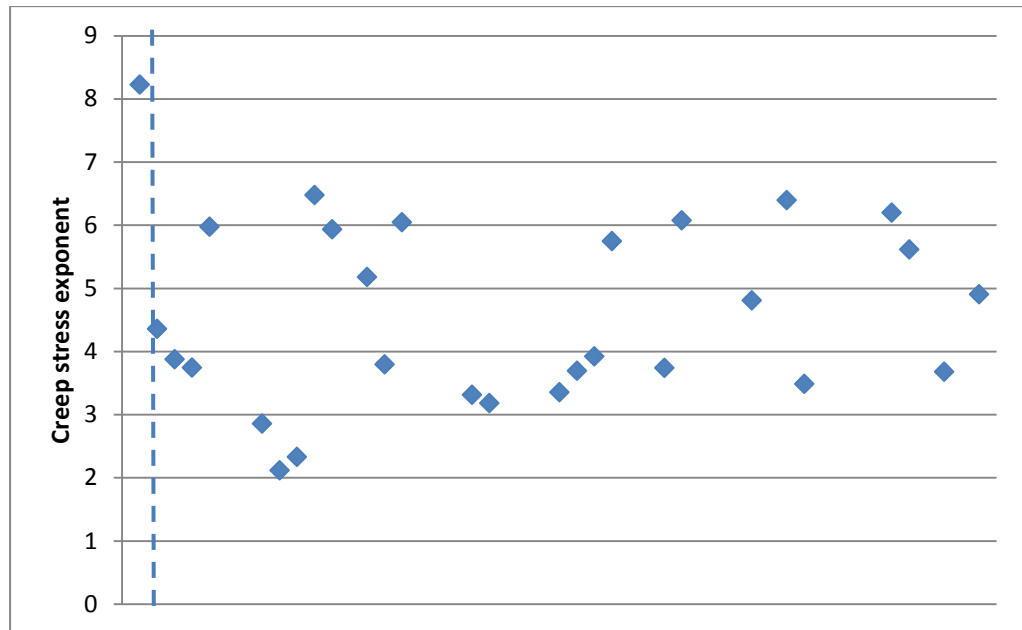
Figure 58: Indentation creep stress exponents from experiments across P92 HAZ at 675°C

In conventional creep tests the deformation mechanisms are dependent on both the test temperature and the applied stress [11]. As the test temperature was the same in tests on the parent and heat affected zone careful examination of the stresses in these tests was made in order to ensure that the tests were comparable. Figure 59 shows the stress field from a typical indentation creep test in the heat affected zone. The maximum stress in the parent material tests was around 300 MPa and this is also the case for the heat affected zone. Also, as with all indentation creep tests, the stress experienced by the bulk of the material in the field is significantly lower. The gradient in the stress field between the untreated parent and heat affected zone is again similar. This all suggests that the tests were performed under comparable temperature and stress states and so the differences are true indications of differences in the material properties as a result of differences in structure.
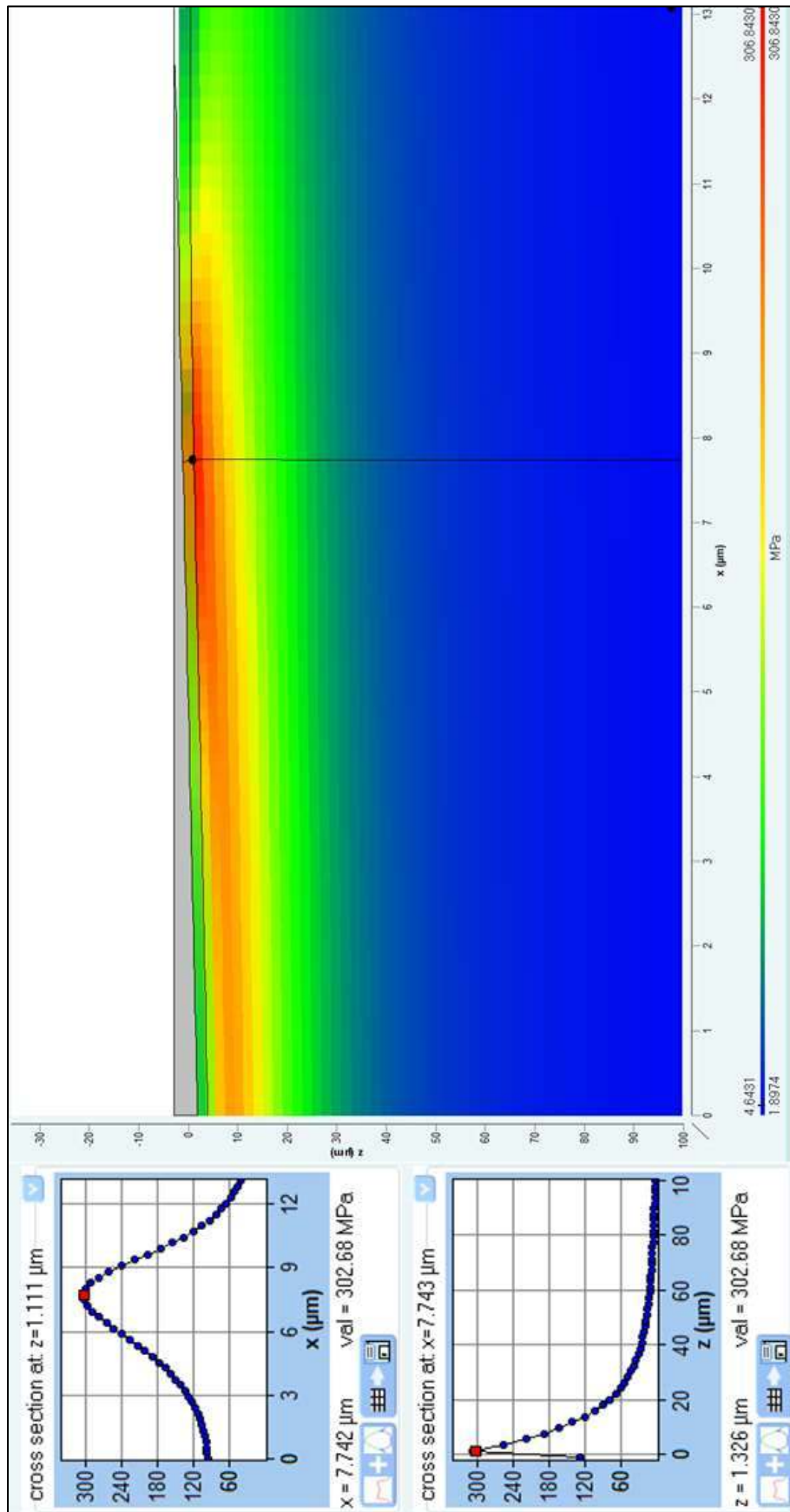
Figure 59: P92 HAZ 100mN creep test stress distribution

These indentation creep measurements are inconsistent with results from uniaxial tests on the same materials which report stress exponents at similar levels to the parent [152]. Although, as mentioned is Chapter 1, these tests are made on bar samples which contain the heat affected zone structure and as such are not strictly focused on the heat affected zone properties in the same way as the indentation creep experiments are. One of the more targeted experimental techniques developed to look at this type of material is impression creep testing.

Impression creep tests were performed at the University of Nottingham by David Tanner on samples of parent and weld material as well as a sample of the heat affected zone. Experiments were performed at stresses between 70 and 100MPa at a test temperature of 675°C using a rectangular probe. To find the creep stress exponent the displacement rate under load at each stress is monitored and converted to an equivalent uniaxial strain rate using an FE fit. These data are then plotted on log axes and it is a fit to this data which gives the creep stress exponents similar to nanoindentation creep data.

Typical data from these tests are shown in Figure 60. The data from the parent and weld materials have an obvious trend with R^2>0.96 for the fits it both cases. The results of these tests also agree well with stress exponents determined by conventional uniaxial tensile testing. The results of testing on the heat affected zone material are less clearly defined. The data from these tests shows a much less defined linear trend than the data from the bulk material tests. Repeated tests on heat affected zone samples show a similar degree of variability as the tests shown below indicating that this is likely due to the sample behaviour and not an experimental issue. This ties in with observations of the variability in the creep exponents calculated form nanoindentation creep data. Despite the degree of variability in the data from the HAZ all data from impression creep tests indicate that the stress exponent for this material is significantly lower than the parent and weld materials.
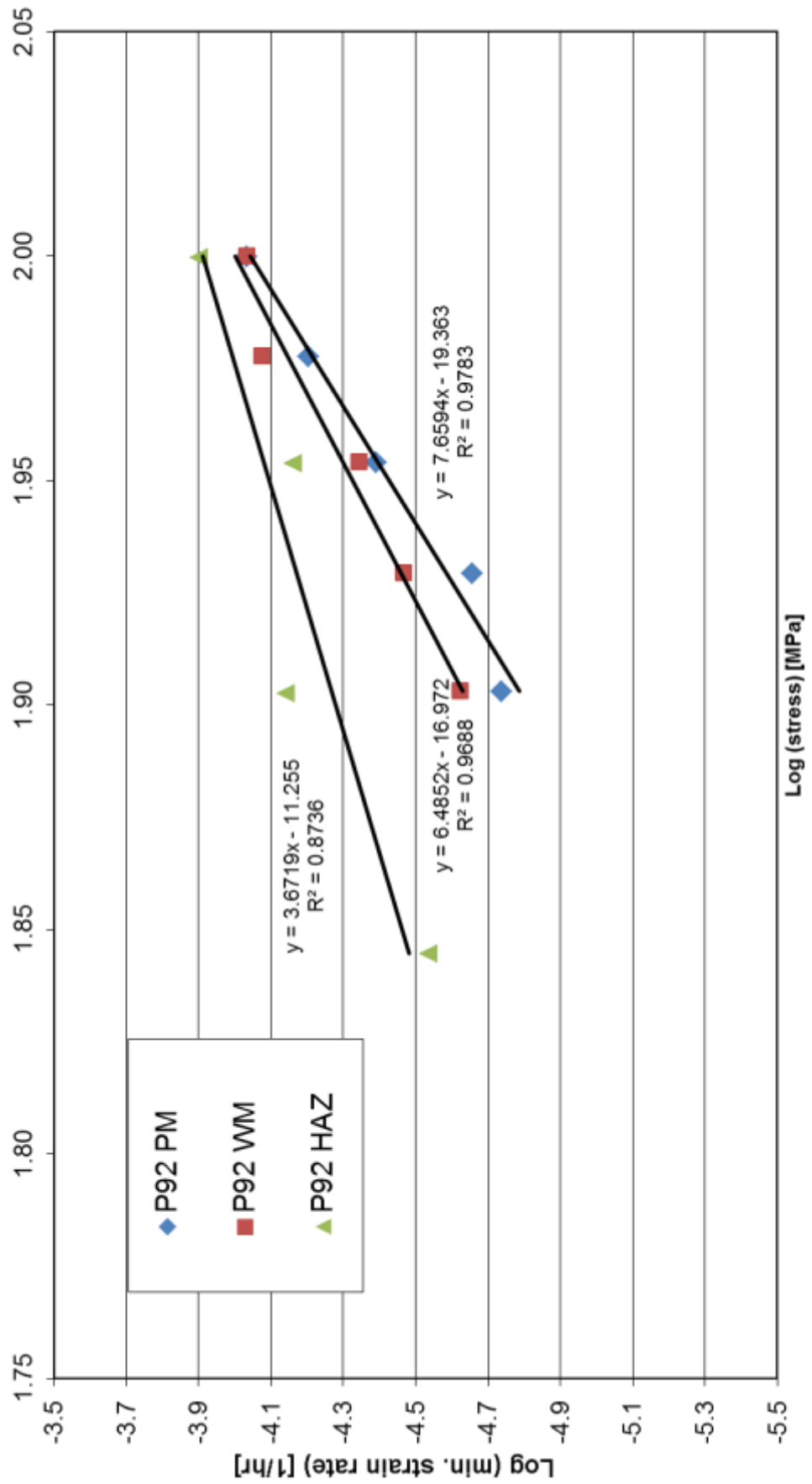
Figure 60: Typical P92 stess exponents from impression creep data at 675°C

There is therefore agreement between the indentation creep results and impression creep test data. Both of these techniques have been developed to examine the creep behaviour of small volumes of material. The results from both small volume creep measurements correlate well with the results of uniaxial tests of bulk materials indicating that the techniques are themselves reliable. Therefore this discrepancy between uniaxial test data and small volume creep test data can be assumed to be due to the insensitivity of the large volume test to the creep deformation of the heat affected zone relative to that of the bulk material. Uniaxial testing can identify the weak points within the heat affected zone structure [16] but cannot identify clearly the differences in creep behaviour which lead to these failures. Impression creep testing and nanoindentation creep testing of these materials allow testing to focus on the heat affected zone giving properties specifically for that region. Both techniques indicate that the deformation mechanism in the heat affected zone is different form the weld and parent materials.

6.3 Summary

Indentation creep testing has been used to characterise both the mechanical properties and creep behaviour of P92 steel. The hardness and elastic modulus of the parent and weld material have been determined and found to be in line with previous measurements. Nanoindentation has also been used to map the change in hardness across the heat affected zone highlighting the change in hardness through the coarse and fine grained regions. Nanoindentation creep experiments were also performed on the parent material and heat affected zone samples. Nanoindentation creep measurements on the parent again gave comparable results to conventional uniaxial tensile tests. Tests on the heat affected zone indicate much lower creep stress exponents through this region than previous measurements would indicate. This is however consistent with impression creep measurements indicating that these results are a true indication of the creep

behaviour of the different structures of material through the heat affected zone.

Chapter 7 – Discussion

The goal of this thesis was to establish whether high temperature nanoindentation could be used as a practical tool in the characterisation of materials for power generation applications. In order to answer this question investigations have been made to determine the best data collection method in order to minimise any thermal fluctuations during measurements. Analyses have also been made of the data treatments used to determine the mechanical and creep properties of materials in elevated temperature nanoindentation.

7.1 High temperature nanoindentation methodology

At the start of the project a purging chamber was designed to house the NanoTest in order to allow testing in an Argon environment. This was done to slow the rate of oxidation of steel samples in order to allow experiments to be run before the oxide layer started to affect nanoindentation measurements.

Following on from this experiments were performed using the two most commonly used temperature control methods. These methods are used to ensure there is thermal equilibrium between sample and indenter in indentation experiments for elevated temperature tests. The key difference between the techniques used is the use of heated indenters instead of long pre-indent contact stabilisations. Experiments on fused silica and gold highlight the limitations of using contact thermal stabilisation.

Thermal modelling indicates that after 8 hours in contact the unheated indenter has reached thermal equilibrium with the sample. The equilibrium temperature is however significantly lower than the body of the sample. This leads to uncertainty regarding the true test temperature for these tests. Another result of this is a temperature gradient from the point of contact into

the body of the sample. The effect is more dramatic on conductive samples due to the formation of a steeper temperature gradient.

The practical implications of this were explored by performing experiments on the two samples at elevated temperatures. The temperature gradient leads to heat transfer as soon as the indenter starts to move into the surface leading to much higher thermal drift than observed in room temperature measurements. As predicted by modelling the effect was more extreme for the tests on gold than fused silica, this is due to the higher thermal conductivity of the gold sample. This technique limits the maximum test temperature for all materials and is unusable for conductive samples even at relatively low temperatures.

For experiments using a heated indenter, a technique based on a methodology developed by the University of Cambridge was used in order to ensure the indenter temperature was matched to the surface. Using this technique it was possible to achieve thermal drift rates equivalent to room temperature measurements. These drift rates were achievable regardless of the conductivity of the material tested and at much higher temperatures. This means that the technique can be widely applied to materials for a variety of high temperature applications. Additionally, with the use of sample surface thermocouples it is possible to ensure the accuracy of the test temperature (within the bounds of the accuracy of the thermocouple).

7.2 Correction of time dependent depth changes in nanoindentation analysis

A number of techniques have been examined which were developed to minimise the influence of time dependent deformation on the analysis of nanoindentation data. This was done to investigate whether higher than expected moduli for $650^{\circ}C$ measurements on P91 steel could be due to viscous deformation. Experimental techniques designed to minimise the effect on the collected data have been examined as well as a technique

designed to correct the data prior to analysis. A new analysis technique building on the Oliver and Pharr analysis method has also been evaluated. This technique, developed by the Saxonian Instutute of Surface mechanics, was designed to remove the effects of viscoelasticity observed in room temperature nanoindentation on polymers. Therefore a study was made of the application of this technique to the viscous deformation seen in metals at elevated temperatures.

The conventional experimental technique to minimise the effects of viscous deformation on indentation unloading data is to include a long dwell at peak load to allow stresses to relax before unloading. This was utilised to examine the P91 parent and weld materials at 650°C, a 300s dwell was used to allow stress relaxation. This has the effect of significantly lowering the elastic modulus calculated from the data compared to tests with shorter dwell periods. Analysis of data from tests with 30s hold return a significantly higher modulus than has previously been reported in the literature. These results also indicate different moduli for the parent and weld material where it is expected the moduli should be the same. Critically the longer creep hold tests return moduli in line with those previously reported and indicate the modulus of the parent and weld are the same. This suggests the hypothesis that the high moduli from previous tests were due to the effect of viscous deformation on the initial unloading data is correct. Further tests on P91 and P92 steel and weld at elevated temperatures used longer dwell periods to minimise this affect.

Although experimental design has been shown to be effective in resolving this problem there were still benefits to investigating correction methods to analyse affected data. Initially this was investigated as a way of utilising data from experiments performed with shorter dwell periods but the correction techniques have also been used to try to identify any effect of viscous deformation on high temperature indentation data. There is also the possibility of maximising the number of tests which could be performed before oxidation effects become an issue.

Discussion

The creep compliance correction uses data from the dwell period in order to estimate the contribution of the creep rate at the end of the dwell to the initial unloading rate. This is then used to make a correction to the analysed data removing the effect of the loading rate. The creep compliance correction was applied to data from the P91 parent and weld collected at 650$^\text{o}$C with a 30s hold period. With the creep compliance correction applied the analysis of this data returns moduli in line with those reported in literature. However similar analysis of room temperature data from viscoelastic polymers indicates that the creep compliance method may overestimate the correction needed. This is due to the correction being made based on the creep rate at peak load where in actuality the creep rate will drop very rapidly as the load is removed.

Finally, a new analysis technique developed to remove the effect of viscoelastic deformation from nanoindentation analysis has been evaluated. This analysis, developed at Saxonian Institute of Surface Mechanics (Ummanz,DE), builds on the concept of the effective indenter. The key advance is the development of a fit to the unloading data which allows for the time dependent deformation seen in viscous materials. Nanoindentation data from polymers and from steel at elevated temperatures analysed with using the standard Oliver and Pharr method, return power law fitting coefficients which are outside the physical limits of the geometry of the contact (m>2). This indicates that the fit is not suitable for experiments where there is viscous deformation of the surface under load. When analysed with the "time dependent effective indenter" analysis the fitting co-efficients for all materials falls within the physical limits (1<m<2). This also has the effect of correcting the modulus so that, for the steel parent and weld material, the modulus results are the same and around the values previously reported in literature. Interestingly these results are much closer to those found from the long hold period tests indicating that, unlike the creep compliance correction, there is no over correction of the data. This is due to this solution not being correction based on the evaluation of the creep rate at a single point. Instead the

analysis routine is improved by the implementation of an improved fit to the actual nanoindentation unloading data.

7.3 Determination of the mechanical properties of P91 and P92 steel at elevated temperatures

Experiments were performed to characterise the hardness and Young's modulus of samples of the parent material, weld and heat affected zone from P91 and P92 welds. Where possible this data has been compared to results from conventional tests on the same materials.

Initially experiments were performed on samples of P91 PM, WM and HAZ in order to determine whether results were comparable to previous tests. Results of experiments at room temperature are comparable, although work hardening of the surface due to polishing does lead to some depth dependence in the hardness measurements. Nanoindentation is also shown to be sensitive enough to detect the changes in hardness expected through the changing microstructure of the heat affected zone. Experiments are also presented which show the properties of P91 at its maximum operating temperature 650$^{\mathrm{o}}$C. Results from experiments at 650$^{\mathrm{o}}$C also show good correlation with hot hardness measurements from literature. As discussed in section 7.2 the moduli determined at this temperature do not appear to relate to previous measurements. This is due to the effect of viscous deformation on the indentation unloading and is corrected by taking this deformation into account.

Following on from this similar experiments were performed on the samples of P92 PM, WM and HAZ. Results from tests on the bulk parent and weld samples at room temperature again match with data from conventional characterisation techniques. In addition to tests on bulk samples results from lines of indentations made across the heat affected zone are presented. These show that there is a hardness drop across the heat affected zone relating to the structures of the fine grained and coarse grained regions. This matches

results from previous tests which report a hardness change through the HAZ structures. Modulus values calculated from the same indentations show no change through the HAZ as modulus is not typically affected by differences in microstructure.

For the P92 high temperature experiments were performed at 675°C again around the maximum operating temperature for this material. Longer hold periods at peak load used in these experiments minimised the influence of viscous deformation on the unloading data. As results the modulus of the parent and weld determined at this temperature match and are in line with conventional measurements without the need for additional corrections. Lines of indentations across the heat affected zone again show no deviation in modulus. Hardness plots of the same data show a hardness drop through the HAZ. The difference between the parent properties and the minimum hardness in the heat affected zone is however much less than at room temperature. This indicates that the structure of the heat affected zone is much more thermally stable than the heat affected zone. This is likely due to the structure having been formed at higher temperatures than the current test temperature.

7.4 Nanoindentation creep testing of P91 and P92 steel

Nanoindentation creep experiments using a pyramidal probe were performed on P91 and P92 steel at 650°C and 675°C respectively. This data was used to determine creep stress exponents which relate to the creep deformation mechanism. These tests were initially performed to evaluate the technique to see if results from P91 and P92 could be related to those from conventional uniaxial tests. Critical to this is an understanding of the true stress condition underneath the Berkovich probe. It is also necessary to determine the extent to primary creep on the steady state indentation dwell data. This is because, unlike conventional tests, the indentation depth in constantly changing. Therefore new material is continually entering the stress field and undergoing primary creep. Strain rates in primary creep are typically much higher than in

secondary creep so this can have a large effect on the calculated creep exponents.

Nanoindentation creep experiments on P91 parent and weld gave creep stress exponents which show good correlation with those determined by uniaxial tensile testing. In order to attempt to understand this correlation a more detailed analysis of the stresses under the indenter was made. This analysis shows that, although the peak stress is higher than conventional uniaxial test stresses, the bulk of the material in the stress field is at stress equivalent to those used in uniaxial tests. Tests at different loads were used in order to evaluate the effect of different stress states on the results. The higher test load has little effect on the creep exponent calculated for the weld material but for the parent material there does appear to be some dependence on load. Examination of the stress field shows that this is due to a large volume of the parent being close to its yield stress in the higher load test. This data shows less good correlation with the uniaxial data, this is expected as uniaxial tests are carried out at sub yield stresses in order to allow gradual creep damage to develop instead of driving plastic deformation with high stresses.

There is however, some variability in the exponents calculated from the nanoindentation tests. This is often assumed to be due to the influence of primary creep on the collected data. As mentioned previously when the indenter is held at constant load new material is entering the stress field continually and undergoing primary creep. Therefore, using this technique it is impossible to avoid this effect. The assumption made is that, if the secondary creep rate is high enough then the influence of this primary creep is minimal. There is also potential that any oxide layer formed on the sample is affecting the recorded creep rates. An oxide would contribute to the creep behaviour of the sample and more work is needed in order to evaluate any potential oxide effect.

After it had been shown that the nanoindentation creep method was able to determine differences in creep behaviour of P91 parent and weld material,

similar experiments on P92 were performed to assess whether the technique could be extended to other similar materials. These tests were performed at 675°C at loads intended to keep the stresses during the test below the yield stress. Evaluation of the stress fields under load confirmed that the bulk of the affected material experienced sub yield stresses. For P92 the stress exponents from the nanoindentation creep tests again correlate reasonably well with uniaxial tests at the same temperature. As the results from the P92 bulk materials were as expected attempts were made to determine the change in creep exponents across the heat affected zone of a weld. The results from these tests indicate that the creep exponent for the heat affected zone is lower than those of the parent and weld material. This is contrary to results of conventional uniaxial tensile testing of HAZ samples which typically report higher stress exponents than the parent and weld. The results are however similar to data from impression creep experiments on a P92 heat affected zone. A potential explanation for this correlation is due the fact that impression creep and nanoindentation creep tests target only the materials in the heat affected zone. Uniaxial tests use samples containing parent, weld and heat affected zone. Therefore results from these tests are the composite reaction of the weldment to the applied stress where, in smaller scale tests the measured creep rates relate solely to the material in the smaller test region.

Chapter 8 – Conclusions and Further work

8.1 Conclusions

The focus of this thesis is to examine the use of high temperature nanoindentation for the characterisation of P91 and P92 steel at their operating temperatures. A summary of the main conclusions that have been drawn from this work are summarised in this section.

- Room temperature nanoindentation measurements have been made on bulk samples of P91 and P92 parent and weld material. Nanoindentation has been shown to have sufficient sensitivity to identify the differences in mechanical properties of these materials.

- For the heat affected zone nanoindentation allows tests to be performed at a scale which allows the mechanical properties of the different structures to be characterised. This has been used to examine the hardness change through the fine and coarse grained region of the HAZ.

- An investigation of the most commonly used high temperature nanoindentation techniques has shown that in order to obtain the most thermally stable condition for high temperature indentation experiments, heated indenters are a necessity.

- Elevated temperature nanoindentation has been successfully used to characterise the mechanical properties of P91 and P92 steel. The results of these tests show excellent agreement with results of conventional tests at the same temperatures.

- Elevated temperature nanoindentation experiments have also characterised the change in hardness across the heat affected zone of a P92 weld at 675°C. This provides reliable hardness measurements on a much finer pitch than is possible using conventional techniques giving valuable information about the effect of the HAZ structure on the material properties.

- Nanoindentation creep testing has been used to find power law creep stress exponents. These results show some correlation with uniaxial tensile tests. Tests performed on P91 were able to distinguish between the creep behaviour of parent and weld material.

- Nanoindentation creep testing across the heat affected zone of a P92 welded section indicate that the creep behaviour of this region is different to that indicated by conventional testing. These results have be shown to have more in common with results from other small scale creep tests. This is an interesting correlation and indicates that nanoindentation creep testing has potential for assessing the change in creep behaviour through the heat affected zone microstructures.

8.2 Further work

The purging chamber used in this study was sufficient to slow the rate of oxidation of the steel samples. This allowed a sufficient test window for hardness and modulus determinations as well as enough time to perform creep tests with a creep hold of 5 minutes. This is a relatively short time period from which to try and determine the secondary creep behaviour of a material. Longer duration tests could give more reliable results although, in order to allow longer duration tests, improvements would have to be made to the purge. Even with the best possible purge it is unlikely that the oxygen level would be much lower than one part per thousand. In order to achieve

sufficiently low oxygen levels an instrument housed in a vacuum chamber would be needed. This would allow tests to be performed in an oxygen free environment allowing much longer duration tests without the oxide affecting measurements.

Related to this, as discussed at several points in the body of this thesis more work could be done in order to try to evaluate potential oxide layer influences on the results from the current experimental hardware. By heating several samples to their target temperature (650°C for P91, 675°C for P92) within the purging chamber and leaving them for different durations before cooling rapidly, it would be possible to estimate the thickness of the oxide layer at different times during testing. This information could then be used to make a more accurate assessment of the likelihood that the oxide layer is affecting the measured mechanical properties or creep rates.

As mentioned nanoindentation tests show an interesting correlation correlation with impression creep data which could be explored further. Impression creep experiments are typically performed using flat punches. This removes the ambiguity introduced by the complex stress field generated in creep tests with sharp indenters. Therefore this study could be extended by performing nanoindentation creep tests with different indenter geometries. In nanoindentation small asperities on the flat face of the indenter can affect the geometry of the contact. In impression creep testing the impression depth and therefore contact area are much larger than in nanoindentation therefore the effect of asperities is minimal. In nanoindentation tests the effect can be much greater leading to areas of the contact with higher stresses than the bulk. In order to avoid these spherical indenters could be used in preference to punches. The stress field under a spherical probe would be much more uniform than for a sharp indenter allowing easier assessment of the relationship between nanoindentation creep data and data from impression creep tests.

Conclusions and Further work

The work presented in this thesis focuses on just one technique used to determine nanoindentation creep behaviour. There are several other techniques which can be used to gather data in order to evaluate creep behaviour. Of particular relevance is the so called load relaxation test, in this instead of holding at constant load the experiment is held at a constant depth starting at peak load. The drop in applied load with time can then be monitored as stresses relax and it is this data which is then used to evaluate the creep behaviour. This technique has the advantage that the test volume is kept constant, therefore it is the same material which is under test throughout the experiment so primary creep behaviour can be removed from the evaluation.

Bibliography

[1]   DuPont JN. Microstructural evolution and high temperature failure of ferritic to austenitic dissimilar welds. International Materials Reviews 2012;57.

[2]   Masuyama F. Creep degradation in welds of Mod.9Cr-1Mo steel. International Journal of Pressure Vessels and Piping 2006;83.

[3]   Hyde T, Sun W, Becker A, Williams J. Creep properties and failure assessment of new and fully repaired P91 pipe welds at 923 K. Proceedings of the Institution of Mechanical Engineers, Part L: Journal of Materials: Design and Applications 2004;218:211.

[4]   Ennis PJ, Czyrska-Filemonowicz A. Recent advances in creep-resistant steels for power plant applications. 2003.

[5]   Ogata T, Sakai T, Yaguchi M. Damage characterization of a P91 steel weldment under uniaxial and multiaxial creep. Materials Science and Engineering a-Structural Materials Properties Microstructure and Processing 2009;510-11.

[6]   Giroux PF, Dalle F, Sauzay M, Malaplate J, Fournier B, Gourgues-Lorenzon AF. Mechanical and microstructural stability of P92 steel under uniaxial tension at high temperature. Materials Science and Engineering a-Structural Materials Properties Microstructure and Processing 2010;527.

[7]   Giroux PF, Dalle F, Sauzay M, Perez G, Tournie I, Rabeau V, Malaplate J, Van Den Berghe T, Fournier B, Gourgues-Lorenzon AF. Mechanical and microstructural stability of P92 steel under uniaxial tension at high temperature. Materials at High Temperatures 2010;27.

[8]   Saber M, Tanner DWJ, Sun W, Hyde TH. Determination of creep and damage properties for P92 at 675 degrees C. Journal of Strain Analysis for Engineering Design 2011;46:842.

[9]   Yaghi AH, Hyde TH, Becker AA, Sun W. Numerical simulation of P91 pipe welding including the effects of solid-state phase transformation on residual stresses. Proceedings of the Institution of Mechanical Engineers Part L-Journal of Materials-Design and Applications 2007;221.

Bibliography

[10]   Ule B, Nagode A. A model based creep equation for 9Cr-1Mo-0.2V (P91 type) steel. Materials Science and Technology 2007;23.

[11]   Springer Handbook of Materials Measurement Methods: Springer, 2006.

[12]   Klueh RL. Elevated temperature ferritic and martensitic steels and their application to future nuclear reactors. International Materials Reviews 2005;50.

[13]   Eggeler G, Ramteke A, Coleman M, Chew B, Peter G, Burblies A, Hald J, Jefferey C, Rantala J, Dewitte M, Mohrmann R. ANALYSIS OF CREEP IN A WELDED P91 PRESSURE-VESSEL. International Journal of Pressure Vessels and Piping 1994;60:237.

[14]   Abd El-Azim ME, Nasreldin AM, Zies G, Klenk A. Microstructural instability of a welded joint in P91 steel during creep at 600 degrees C. Materials Science and Technology 2005;21.

[15]   Hyde TH, Sun W, Williams JA. Creep behaviour of parent, weld and HAZ materials of new, service-aged and repaired 1/2Cr1/2Mo1/4V: 2 1/4Cr1Mo pipe welds at 640 degrees C. Materials at High Temperatures 1999;16.

[16]   Francis JA, Cantin GMD, Mazur W, Bhadeshia HKDH. Effects of weld preheat temperature and heat input on type IV failure. Science and Technology of Welding and Joining 2009;14.

[17]   Chu SNG, Li JCM. IMPRESSION CREEP - NEW CREEP TEST. Journal of Materials Science 1977;12:2200.

[18]   Sastry DH. Impression creep technique--An overview. Materials Science and Engineering: A 2005;409:67.

[19]   Dorcakova F, Spakova J, Dusza J. Impression creep of MoSi(2). Kovove Materialy-Metallic Materials 2009;47:83.

[20]   Dutta I, Park C, Choi S. Impression creep characterization of rapidly cooled Sn-3.5Ag solders. Materials Science and Engineering a-Structural Materials Properties Microstructure and Processing 2004;379:401.

Bibliography

[21]   Mondal AK, Kumar S. Impression creep behaviour of magnesium alloy-based hybrid composites in the longitudinal direction. Composites Science and Technology 2008;68:3251.

[22]   Mondal AK, Kumar S. Impression creep behaviour of magnesium alloy-based hybrid composites in the transverse direction. Composites Science and Technology 2009;69:1592.

[23]   Sun W, Hyde TH, Brett SJ. Application of impression creep data in life assessment of power plant materials at high temperatures. Proceedings of the Institution of Mechanical Engineers, Part L: Journal of Materials: Design and Applications 2008;222:175.

[24]   Yang FQ, Li JCM. IMPRESSION CREEP BY AN ANNULAR PUNCH. Mechanics of Materials 1995;21:89.

[25]   Yan W, Wen S, Liu J, Yue Z. Determination of Creep Parameters of the Thermal Barrier Coatings Using an Impression Creep Test. Rare Metal Materials and Engineering 2010;39:1829.

[26]   Yan W, Wen S, Liu J, Yue Z. Comparison between impression creep and uni-axial tensile creep performed on nickel-based single crystal superalloys. Materials Science and Engineering a-Structural Materials Properties Microstructure and Processing 2010;527:1850.

[27]   Hyde TH, Sun W. Evaluation of conversion relationships for impression creep test at elevated temperatures. International Journal of Pressure Vessels and Piping 2009;86:757.

[28]   Hyde TH, Stoyanov M, Sun W, Hyde CJ. On the interpretation of results from small punch creep tests. Journal of Strain Analysis for Engineering Design 2010;45:141.

[29]   Sargent PM, Ashby MF. Indentation creep. Materials Science and Technology 1992;8:594.

[30]   Sun Y, Bell T, Zheng S. Finite element analysis of the critical ratio of coating thickness to indentation depth for coating property measurements by nanoindentation. Thin Solid Films 1995;258:198.

Bibliography

[31]   Chudoba T, Schwarzer N, Linss V, Richter F. Determination of mechanical properties of graded coatings using nanoindentation. Thin Solid Films 2004;469-470:239.

[32]   Fox-Rabinovich GS, Endrino JL, Beake BD, Aguirre MH, Veldhuis SC, Quinto DT, Bauer CE, Kovalev AI, Gray A. Effect of temperature of annealing below 900 °C on structure, properties and tool life of an AlTiN coating under various cutting conditions. Surface and Coatings Technology 2008;202:2985.

[33]   Maier P, Richter A, Faulkner RG, Ries R. Application of nanoindentation technique for structural characterisation of weld materials. Materials Characterization 2002;48:329.

[34]   Jang JI, Son D, Lee YH, Choi Y, Kwon D. Assessing welding residual stress in A335 P12 steel welds before and after stress-relaxation annealing through instrumented indentation technique. Scripta Materialia 2003;48.

[35]   Lan L, Qiu C, Zhao D. Analysis of the Hardness and Elastic Modulus Distribution in a High Strength Steel Welded Joint by Nanoindentation. Manufacturing Process Technology, Pts 1-5 2011;189-193.

[36]   Khrushchov MM, Berkovich ES. Methods of Determining the Hardness of Very Hard Materials: The Hardness of Diamond. Industrial Diamond Review 1951;11:42.

[37]   Pethicai JB, Hutchings R, Oliver WC. Hardness measurement at penetration depths as small as 20 nm. Philosophical Magazine A 1983;48:593

[38]   Loubet JL, Georges JM, Marchesini O, Meille G. Vickers Indentation Curves of Magnesium Oxide (MgO). Journal of Tribology 1984;106:43.

[39]   Newey D, Wilkins MA, Pollock HM. An ultra-low-load penetration hardness tester. Journal of Physics E: Scientific Instruments 1982;15:119.

[40]   Stone D, LaFontaine WR, Alexopoulos P, Wu T-W, Li C-Y. An investigation of hardness and adhesion of sputter-deposited aluminum on silicon by utilizing a continuous indentation test. Journal of Materials Research;3:141.

[41]   Doerner MF, Nix WD. A method for interpreting the data from depth-sensing indentation instruments. 1986;1:601.

Bibliography

[42]   Oliver W, Phar G. An improved technique for determining hardness and elastic modulus using load and displacement sensing indentation. Journal of Materials Research 1992;7:1564.

[43]   Bolshakov A, Pharr GM. Influences of pileup on the measurement of mechanical properties by load and depth sensing indentation techniques. Journal of Materials Research 1998;13:1049.

[44]   Chaudhri MM, Winter M. The load-bearing area of a hardness indentation. Journal of Physics D: Applied Physics 1988;21:370.

[45]   Bolshakov A, Pharr GM. Influences of pileup on the measurement of mechanical properties by load and depth sensing indentation techniques. Journal Name: Journal of Materials Research; Journal Volume: 13; Journal Issue: 4; Other Information: PBD: Apr 1998 1998:Medium: X; Size: pp. 1049.

[46]   Oliver WC, Pharr GM. Measurement of hardness and elastic modulus by instrumented indentation: Advances in understanding and refinements to methodology. Journal of Materials Research 2004;19:3.

[47]   Nix WD, Gao H. Indentation size effects in crystalline materials: A law for strain gradient plasticity. Journal of the Mechanics and Physics of Solids 1998;46:411.

[48]   Xue Z, Huang Y, Hwang KC, Li M. The Influence of Indenter Tip Radius on the Micro-Indentation Hardness. Journal of Engineering Materials and Technology 2002;124:371.

[49]   Qu S, Huang Y, Nix WD, Jiang H, Zhang F, Hwang KC. Indenter tip radius effect on the Nix Gao relation in micro- and nanoindentation hardness experiments. Journal of Materials Research 2004;19:3423.

[50]   Zhang F, Huang Y, Hwang K-C. The indenter tip radius effect in micro- and nanoindentation hardness experiments. Acta Mechanica Sinica 2006;22:1.

[51]   Huang Y, Zhang F, Hwang KC, Nix WD, Pharr GM, Feng G. A model of size effects in nano-indentation. Journal of the Mechanics and Physics of Solids 2006;54:1668.

[52]   Durst K, Goken M, Pharr GM. Indentation size effect in spherical and pyramidal indentations. Journal of Physics D: Applied Physics 2008;41:074005.

Bibliography

[53]   Bouzakis KD, Michailidis N, Hadjiyiannis S, Skordaris G, Erkens G. The effect of specimen roughness and indenter tip geometry on the determination accuracy of thin hard coatings stress-strain laws by nanoindentation. Materials Characterization 2002;49:149.

[54]   Qasmi M, Delobelle P. Influence of the average roughness Rms on the precision of the Young's modulus and hardness determination using nanoindentation technique with a Berkovich indenter. Surface and Coatings Technology 2006;201:1191.

[55]   Tsui T, Oliver W, Pharr G. Influences of stress on the measurement of mechanical properties using nanoindentation: Part I. Experimental studies in an aluminum alloy. Journal of Materials Research 1996;11:752.

[56]   Schwarzer N, Chudoba T, Pharr GM. On the evaluation of stresses in coated materials during nanoindentation with sharp indenters. Surface and Coatings Technology 2006;200:4220.

[57]   Saif MTA, Hui CY, Zehnder AT. Interface shear stresses induced by non-uniform heating of a film on a substrate. Thin Solid Films 1993;224:159.

[58]   Asif SAS, Pethica JB. Nanoindentation creep of single-crystal tungsten and gallium arsenide. 1997;76:1105

[59]   Bahr DF, Wilson DE, Crowson DA. Energy considerations regarding yield points during indentation. Journal of Materials Research 1999;14:2269.

[60]   Suzuki T, Ohmura T. Ultra-microindentation of silicon at elevated temperatures. 1996;74:1073

[61]   Beake BD, Smith JF. High-temperature nanoindentation testing of fused silica and other materials. 2002;82:2179

[62]   Beake BD, Goodes SR, Smith JF. Nanoscale materials testing under industrially relevant conditions: high-temperature nanoindentation testing. Z. Metallkd. 2003;94:1.

[63]   Kramer DE, Yoder KB, Gerberich WW. Surface constrained plasticity: Oxide rupture and the yield point process. 2001;81:2033

[64]   Lund AC, Hodge AM, Schuh CA. Incipient plasticity during nanoindentation at elevated temperatures. Applied Physics Letters 2004;85:1362.

Bibliography

[65]   Packard CE, Schroers J, Schuh CA. In situ measurements of surface tension-driven shape recovery in a metallic glass. Scripta Materialia 2009;60:1145.

[66]   Volinsky AA, Moody NR, Gerberich WW. Nanoindentation of Au and Pt/Cu thin films at elevated temperatures. Journal of Materials Research 2004;19:2650.

[67]   Hinz M, Kleiner A, Hild S, Marti O, Dürig U, Gotsmann B, Drechsler U, Albrecht TR, Vettiger P. Temperature dependent nano indentation of thin polymer films with the scanning force microscope. European Polymer Journal 2004;40:957.

[68]   Smith JF, Zheng S. High temperature nanoscale mechanical property measurements. Surface Engineering 2000;16:143.

[69]   Schuh CA, Packard CE, Lund AC. Nanoindentation and contact-mode imaging at high temperatures. J. Mater. Res. 2005;21:725.

[70]   Schuh CA, Mason JK, Lund AC. Quantitative insight into dislocation nucleation from high-temperature nanoindentation experiments. Nat Mater 2005;4:617.

[71]   Schuh CA, Lund AC, Nieh TG. New regime of homogeneous flow in the deformation map of metallic glasses: elevated temperature nanoindentation experiments and mechanistic modeling. Acta Materialia 2004;52:5879.

[72]   Trelewicz JR, Schuh CA. Hot nanoindentation of nanocrystalline Ni-W alloys. Scripta Materialia 2009;61:1056.

[73]   Ruffell S, Bradby JE, Williams JS, Munoz-Paniagua D, Tadayyon S, Coatsworth LL, Norton PR. Nanoindentation-induced phase transformations in silicon at elevated temperatures. Nanotechnology 2009;20:135603.

[74]   Giuliani F, Goruppa A, Lloyd SJ, Teer D, Clegg WJ. High Temperature Deformation of AlN/CrN Multilayers using Nanoindentation. Proc. Mat. Res. Soc. Symp., 2005.

[75]   Korte S, Clegg WJ. Micropillar compression of ceramics at elevated temperatures. Scripta Materialia 2009;60:807.

[76]   Vandeperre LJ, Giuliani F, Lloyd SJ, Clegg WJ. The hardness of silicon and germanium. Acta Materialia 2007;55:6307.

Bibliography

[77]   Xia J, Li CX, Dong H. Hot-stage nano-characterisations of an iron aluminide. Materials Science and Engineering A 2003;354:112.

[78]   Domnich V, Aratyn Y, Kriven WM, Gogotsi Y. Temperature dependence of silicon hardness: Experimental evidence of phase transformations, Reviews on Advanced Materials Science. Reviews on Advanced Materials Science 2008;17:33.

[79]   Gray A, Beake BD. Elevated temperature nanoindentation and viscoelastic behaviour of thin poly(ethylene terephthalate) films. Journal of Nanoscience and Nanotechnology 2007;7:2530.

[80]   Gray A, Orecchia D, Beake BD. Nanoindentation of Advanced Polymers Under Non-Ambient Conditions: Creep Modelling and Tan Delta. Journal of Nanoscience and Nanotechnology 2009;9:4514.

[81]   Zhang Y, Cheng Y-T, Grummon DS. Indentation stress dependence of the temperature range of microscopic superelastic behavior of nickel-titanium thin films. 2005;98:033505.

[82]   Richter A, Chen CL, Smith R, McGee E, Thomson RC, Kenny SD. Hot stage nanoindentation in multi-component Al-Ni-Si alloys: Experiment and simulation. Materials Science and Engineering: A 2008;494:367.

[83]   Thurn J, Cook RF. Simplified area function for sharp indenter tips in depth-sensing indentation. Journal of Materials Research 2002;17:1143.

[84]   Beake BD, Smith JF. Nano-impact testing--an effective tool for assessing the resistance of advanced wear-resistant coatings to fatigue failure and delamination. Surface and Coatings Technology 2004;188-189:594.

[85]   Fox-Rabinovich GS, Beake BD, Endrino JL, Veldhuis SC, Parkinson R, Shuster LS, Migranov MS. Effect of mechanical properties measured at room and elevated temperatures on the wear resistance of cutting tools with TiAlN and AlCrN coatings. Surface and Coatings Technology 2006;200:5738.

[86]   Fox-Rabinovich GS, Endrino JL, Beake BD, Aguirre MH, Veldhuis SC, Quinto DT, Bauer CE, Kovalev AI, Gray A. Effect of temperature of annealing below 900 °C on structure, properties and tool life of an AlTiN coating under various cutting conditions. Surface and Coatings Technology 2008;202:2985.

Bibliography

[87]   Fox-Rabinovich GS, Endrino JL, Beake BD, Kovalev AI, Veldhuis SC, Ning L, Fontaine F, Gray A. Impact of annealing on microstructure, properties and cutting performance of an AlTiN coating. Surface and Coatings Technology 2006;201:3524.

[88]   Fox-Rabinovich GS, Veldhuis SC, Dosbaeva GK, Yamamoto K, Kovalev AI, Wainstein DL, Gershman IS, Shuster LS, Beake BD. Nanocrystalline coating design for extreme applications based on the concept of complex adaptive behavior. Journal of Applied Physics 2008;103:083510.

[89]   Beake BD, Fox-Rabinovich GS, Veldhuis SC, Goodes SR. Coating optimisation for high speed machining with advanced nanomechanical test methods. Surface and Coatings Technology 2009;203:1919.

[90]   Beake BD, Smith JF, Gray A, Fox-Rabinovich GS, Veldhuis SC, Endrino JL. Investigating the correlation between nano-impact fracture resistance and hardness/modulus ratio from nanoindentation at 25-500 °C and the fracture resistance and lifetime of cutting tools with Ti1-xAlxN (x = 0.5 and 0.67) PVD coatings in milling operations. Surface and Coatings Technology 2007;201:4585.

[91]   Mulhearn TO, Tabor D. CREEP AND HARDNESS OF METALS - A PHYSICAL STUDY. Journal of the Institute of Metals 1960;89:7.

[92]   Mayo MJ, Nix WD. A MICRO-INDENTATION STUDY OF SUPERPLASTICITY IN PB, SN, AND SN-38 WT-PERCENT-PB. Acta Metallurgica 1988;36:2183.

[93]   Chen J, Bull SJ. The investigation of creep of electroplated Sn and Ni-Sn coating on copper at room temperature by nanoindentation. Surface & Coatings Technology 2009;203:1609.

[94]   Xu L, Pang JHL. Nanoindentation on SnAgCu lead-free solder joints and analysis. Journal of Electronic Materials 2006;35:2107.

[95]   Shibutani T, Yu Q, Shiratori M. A study of deformation mechanism during nanoindentation creep in tin-based solder balls. Journal of Electronic Packaging 2007;129:71.

Bibliography

[96]   Mahmudi R, Rezaee-Bazzaz A, Banaie-Fard HR. Investigation of stress exponent in the room-temperature creep of Sn-40Pb-2.5Sb solder alloy. Journal of Alloys and Compounds 2007;429:192.

[97]   Shen L, Cheong WCD, Foo YL, Chen Z. Nanoindentation creep of tin and aluminium: A comparative study between constant load and constant strain rate methods. Materials Science and Engineering a-Structural Materials Properties Microstructure and Processing 2012;532:505.

[98]   Goodall R, Clyne TW. A critical appraisal of the extraction of creep parameters from nanoindentation data obtained at room temperature. Acta Materialia 2006;54:5489.

[99]   Bower AF, Fleck NA, Needleman A, Ogbonna N. Indentation of a Power Law Creeping Solid. Proceedings of the Royal Society of London. Series A: Mathematical and Physical Sciences 1993;441:97.

[100]   Milhans J, Khaleel M, Sun X, Tehrani M, Al-Haik M, Garmestani H. Creep properties of solid oxide fuel cell glass-ceramic seal G18. Journal of Power Sources 2010;195:3631.

[101]   Milhans J, Li DS, Khaleel M, Sun X, Al-Haik MS, Harris A, Garmestani H. Mechanical properties of solid oxide fuel cell glass-ceramic seal at high temperatures. Journal of Power Sources 2011;196.

[102]   Bhakhri V, Klassen R. Investigation of high-temperature plastic deformation using instrumented microindentation tests. Part IThe deformation of three aluminum alloys at 473 K to 833 K. Journal of Materials Science 2006;41:2259.

[103]   Bhakhri V, Klassen R. Investigation of high-temperature plastic deformation using instrumented microindentation tests. Part II: The deformation of Al-based particulate reinforced composites at 473 K to 833 K. Journal of Materials Science 2006;41:2249.

[104]   Liu YC, Teo JWR, Tung SK, Lam KH. High-temperature creep and hardness of eutectic 80Au/20Sn solder. Journal of Alloys and Compounds 2008;448:340.

[105]   Yaghi AH, Hyde TH, Becker AA, Sun W, Hilson G, Simandjuntak S, Flewitt PEJ, Pavier MJ, Smith DJ. A Comparison Between Measured and

Bibliography

Modeled Residual Stresses in a Circumferentially Butt-Welded P91 Steel Pipe. Journal of Pressure Vessel Technology 2010;132:011206.

[106]   Hyde TH, Sun W, Yaghi AH, Leen SB. Some issues on structural integrity analysis of P91 welds in power plants subjected to high temperature creep*. Fatigue & Fracture of Engineering Materials & Structures 2009;32:926.

[107]   Aguado F, Baonza VG. Prediction of bulk modulus at high temperatures from longitudinal phonon frequencies: Application to diamond, c-BN, and 3C-SiC. Physical Review B 2006;73.

[108]   Hess P. The mechanical properties of various chemical vapor deposition diamond structures compared to the ideal single crystal. Journal of Applied Physics 2012;111.

[109]   Yamamoto Y, Imai T, Tanabe K, Tsuno T, Kumazawa Y, Fujimori N. The measurement of thermal properties of diamond. Diamond and Related Materials 1997;6:1057.

[110]   Edgar JH. Properties of Group III Nitrides. In: Edgar JH, editor. Properties of Group III Nitrides. London: Institution of Engineering and Technology, 1994. p.1.

[111]   Chudoba T, Richter F. Investigation of creep behaviour under load during indentation experiments and its influence on hardness and modulus results. Surface and Coatings Technology 2001;148:191.

[112]   Oliver W, Pharr G. An improved technique for determining hardness and elastic modulus using load and displacement sensing indentation. Journal of Materials Research 1992;7:1564.

[113]   Sneddon IN. The relation between load and penetration in the axisymmetric boussinesq problem for a punch of arbitrary profile. International Journal of Engineering Science 1965;3:47.

[114]   Lu Y, Jones D, Tandon G, Putthanarat S, Schoeppner G. High Temperature Nanoindentation of PMR-15 Polyimide. Experimental Mechanics 2009.

[115]   Everitt NM, Davies MI, Smith JF. High temperature nanoindentation - the importance of isothermal contact. Philosophical Magazine 2011;91:1221.

Bibliography

[116]   Yaghi AH, Hyde TH, Becker AA, Sun W, Hilson G, Simandjuntak S, Flewitt PEJ, Pavier MJ, Smith DJ. A Comparison Between Measured and Modeled Residual Stresses in a Circumferentially Butt-Welded P91 Steel Pipe. Journal of Pressure Vessel Technology-Transactions of the Asme 2010;132.

[117]   Cerri E, Evangelista E, Spigarelli S, Bianchi P. Evolution of microstructure in a modified 9Cr-1Mo steel during short term creep. Materials Science and Engineering a-Structural Materials Properties Microstructure and Processing 1998;245:285.

[118]   Schwarzer N, Pharr GM. On the evaluation of stresses during nanoindentation with sharp indenters. Thin Solid Films 2004;469-470:194.

[119]   Hyde TH, Sun W, Becker AA. Analysis of the impression creep test method using a rectangular indenter for determining the creep properties in welds. International Journal of Mechanical Sciences 1996;38:1089.

[120]   Sastry DH. Impression creep technique - An overview. Materials Science and Engineering a-Structural Materials Properties Microstructure and Processing 2005;409:67.

[121]   Li JCM. Impression creep and other localized tests. Materials Science and Engineering a-Structural Materials Properties Microstructure and Processing 2002;322:23.

[122]   Hyde TH, Yehia KA, Becker AA. Application of the reference stress method for interpreting impression creep test data. Materials at High Temperatures 1995;13:133.

[123]   Shibutani T, Yu Q, Shiratori M. Evaluation of diffusion creep in low melting point materials by nanoindentation creep test. Jsme International Journal Series a-Solid Mechanics and Material Engineering 2006;49:397.

[124]   Zhu XY, Liu XJ, Zeng F, Pan F. Room temperature nanoindentation creep of nanoscale Ag/Fe multilayers. Materials Letters 2010;64:53.

[125]   Chang SY, Lee YS, Chang TK. Nanomechanical response and creep behavior of electroless deposited copper films under nanoindentation test. Materials Science and Engineering a-Structural Materials Properties Microstructure and Processing 2006;423:52.

Bibliography

[126]   Cao ZH, Li PY, Meng XK. Nanoindentation creep behaviors of amorphous, tetragonal, and bcc Ta films. Materials Science and Engineering a-Structural Materials Properties Microstructure and Processing 2009;516:253.

[127]   Wang F, Xu KW. An investigation of nanoindentation creep in polycrystalline Cu thin film. Materials Letters 2004;58:2345.

[128]   Wang CL, Lai YH, Huang JC, Nieh TG. Creep of nanocrystalline nickel: A direct comparison between uniaxial and nanoindentation creep. Scripta Materialia 2010;62:175.

[129]   Wang CL, Zhang M, Nieh TG. Nanoindentation creep of nanocrystalline nickel at elevated temperatures. Journal of Physics D-Applied Physics 2009;42.

[130]   Date EHF, Andrews KW. ANISOTROPIC AND COMPOSITION EFFECTS IN ELASTICPROPERTIES OF POLYCRYSTALLINE METALS. Journal of Physics D-Applied Physics 1969;2.

[131]   Kese K, Li ZC. Semi-ellipse method for accounting for the pile-up contact area during nanoindentation with the Berkovich indenter. Scripta Materialia 2006;55:699.

[132]   Sireesha M, Albert SK, Sundaresan S. Microstructure and mechanical properties of weld fusion zones in modified 9Cr-1Mo steel. Journal of Materials Engineering and Performance 2001;10:320.

[133]   Gaffard V, Gourgues-Lorenzon AF, Besson J. High temperature creep flow and damage properties of 9Cr1MoNbV steels: Base metal and weldment. Nuclear Engineering and Design 2005;235.

[134]   Sawant A, Tin S. High temperature nanoindentation of a Re-bearing single crystal Ni-base superalloy. Scripta Materialia 2008;58:275.

[135]   Oyen ML, Cook RF, Emerson JA, Moody NR. Indentation responses of time-dependent films on stiff substrates. Journal of Materials Research 2004;19:2487.

[136]   Wang F, Xu KW. Effect of grain size and holding load on nanoindentation creep of Cu film. Acta Metallurgica Sinica 2004;40:1032.

[137]   Cheng YT, Cheng CM. Relationship between contact stiffness, contact depth, and mechanical properties for indentation in linear viscoelastic solids

using axisymmetric indenters. Structural Control & Health Monitoring 2006;13:561.

[138]   Kassner ME. Fundimentals of creep in metals and alloys. London: Elsevier, 2009.

[139]   Tang B, Ngan AHW, Lu WW. Viscoelastic effects during depth-sensing indentation of cortical bone tissues. Philosophical Magazine 2006;86:5653.

[140]   Fischer-Cripps AC. A simple phenomenological approach to nanoindentation creep. Materials Science and Engineering A 2004;385:74.

[141]   Ngan AHW, Wang HT, Tang B, Sze KY. Correcting power-law viscoelastic effects in elastic modulus measurement using depth-sensing indentation. International Journal of Solids and Structures 2005;42:1831.

[142]   Beake BD, Chen S, Hull JB, Gao F. Nanoindentation behavior of clay/poly(ethylene oxide) nanocomposites. Journal of Nanoscience and Nanotechnology 2002;2:73.

[143]   Oyen ML. Sensitivity of polymer nanoindentation creep measurements to experimental variables. Acta Materialia 2007;55:3633.

[144]   Ngan AHW, Tang B. Viscoelastic effects during unloading in depth-sensing indentation. Journal of Materials Research 2002;17:2604.

[145]   Lu H, Wang B, Ma J, Huang G, Viswanathan H. Measurement of creep compliance of solid polymers by nanoindentation. Mechanics of Time-Dependent Materials 2003;7:189.

[146]   Cheng L, Xia X, Yu W, Scriven LE, Gerberich WW. Flat-punch indentation of viscoelastic material. Journal of Polymer Science Part B-Polymer Physics 2000;38:10.

[147]   Lu JP, Burn LS, Tiganis BE. Creep modeling of ABS pipes at variable temperature. Polymer Engineering and Science 2000;40:2407.

[148]   Oyen ML, Cook RF. Load-displacement behavior during sharp indentation of viscous-elastic-plastic materials. Journal of Materials Research 2003;18:139.

[149]   Shen L, Phang IY, Chen L, Liu TX, Zeng KY. Nanoindentation and morphological studies on nylon 66 nanocomposites. I. Effect of clay loading. Polymer 2004;45:3341.

161

Bibliography

[150]   Pharr GM, Bolshakov A. Understanding nanoindentation unloading curves. Journal of Materials Research 2002;17:2660.

[151]   Mase GT, Smelser R, Mase GE. Continuum Mechanics for Engineers. Boca Raton: CRC Press, 2010.

[152]   Falat L, Vyrostkova A, Homolova V, Svoboda M. Creep deformation and failure of E911/E911 and P92/P92 similar weld-joints. Engineering Failure Analysis 2009;16.

[153]   El-Magd E, Gebhard J. Influence of tempering on the hot hardness of P92 sheet metal. Materialwissenschaft Und Werkstofftechnik 2005;36.

[154]   Wang X, Pan Q-g, Ren Y-y, Shang W, Zeng H-q, Liu H. Microstructure and type IV cracking behavior of HAZ in P92 steel weldment. Materials Science and Engineering a-Structural Materials Properties Microstructure and Processing 2012;552.

[155]   Sugiura R, Yokobori AT, Jr., Suzuki K, Tabuchi M. Characterization of incubation time on creep crack growth for weldments of P92. Engineering Fracture Mechanics 2010;77.

[156]   Ennis PJ, Zielinska-Lipiec A, Wachter O, Czyrska-Filemonowicz A. Microstructural stability and creep rupture strength of the martensitic steel P92 for advanced power plant. Acta Materialia 1997;45:4901.

[157]   Chudoba T, Jennett NM. Higher accuracy analysis of instrumented indentation data obtained with pointed indenters. Journal of Physics D-Applied Physics 2008;41.

[158]   Schuh CA, Packard CE, Lund AC. Nanoindentation and contact-mode imaging at high temperatures. J. Mater. Res. 2006;21:725.

[159]   Pierson HO. Handbook of Carbon, Graphite, Diamond and Fullerenes - Properties, Processing and Applications. William Andrew Publishing/Noyes, 1993. p.258.

[160]   Datchi F, Dewaele A, Le Godec Y, Loubeyre P. Equation of state of cubic boron nitride at high pressures and temperatures. Physical Review B (Condensed Matter and Materials Physics) 2007;75:214104.

Bibliography

[161]   Kukushkin SA, Osipov AV, Bessolov VN, Medvedev BK, Nevolin VK, Tcarik KA. Substrates for epitaxy of gallium nitride: New materials and techniques. Reviews on Advanced Materials Science 2008;17:1.

[162]   Spinner S. ELASTIC MODULI OF GLASSES AT ELEVATED TEMPERATURES BY A DYNAMIC METHOD. Journal of the American Ceramic Society 1956;39:113.

[163]   Smithells Metals Reference Book: Elsevier, 2004.

[164]   Goto T, Anderson OL, Ohno I, Yamamoto S. ELASTIC CONSTANTS OF CORUNDUM UP TO 1825 K. J. Geophys. Res. 1989;94:7588.

[165]   Rice RW. Effects of environment and temperature on ceramic tensile strength–grain size relations. Journal of Materials Science 1997;32:3071.

[166]   Mitchell TE. Dislocations and Mechanical Properties of MgO-Al2O3 Spinel Single Crystals. Journal of the American Ceramic Society 1999;82:3305.

[167]   Krell A. A new look at the influences of load, grain size, and grain boundaries on the room temperature hardness of ceramics. International Journal of Refractory Metals & Hard Materials 1998;16:331.

[168]   Coble RL, Kingery WD. Effect of Porosity on Physical Properties of Sintered Alumina. Journal of the American Ceramic Society 1956;39:377.

<u>Appendix I - Nanoindentation Calibrations</u>

There are three properties which have to be calibrated on the Nanotest[TM] in order to obtain accurate mechanical properties from the samples tested. These are the load frame compliance, the indenter area function and the depth corresponding to the output voltage from the capacitance bridge. The techniques used to calibrate the system are different for room temperature testing and elevated temperature testing and so are discussed separately in the following sections.

<u>Room Temperature Calibrations</u>

<u>Load frame compliance and indenter area function</u>

The load frame compliance is a measure of the stiffness of the Nanotest™ frame. It is important to calculate the load frame compliance as the Oliver and Pharr analysis technique assumes that the elastic behaviour is that of the sample only, see 3.2.3 for details. Similarly, as the analysis is based on the projected contact between the indenter and sample surface, it is important to determine the geometry of the indenter tip.

Typically, in order to determine the compliance of the loading frame, large depth indentations are made in a calibrated fused silica reference sample with known Young's modulus and hardness. The contact stiffness calculated from the data is compared to the expected results and corrected by automated software to find the frame compliance.

It should be noted that in order to find frame compliance in this way, it is important to know the area function of the indenter. When beginning calibrations on a new system neither the frame compliance or indenter area function is known. In order to work around this problem, an iterative method was used to calibrate both the indenter area function and frame compliance concurrently[46]. High depth indentations were used in order to minimise the

164

influence of the low depth non-ideal geometry of the indenter. Initially the indenter is assumed to conform to an ideal geometry as described by Equation 20, where h_c is the contact depth as described in section 3.2.3, in order to determine an approximate compliance value.

$$A(h_c) = 24.5 h_c^2$$

Equation 20

$$\sqrt{A(h_c)} = ah_c + b$$

Equation 21

In practice the true indenter area function is assumed to be of the form shown in Equation 21[112]. To determine the indenter area function sets of indentations were made through the full load range of the nanoindenter and then analysed using the approximate compliance value. This data was then used to generate a plot of projected contact area against contact depth for the area function as shown in Figure 61.

The high load hysteresis curves were then re-analysed using the calculated indenter area function. This compliance was then used to generate another area function. Compliance calibration and area function calculation steps were then performed iteratively starting with a repeat of the compliance analysis using the newly generated area function. This was done until there was a convergence in the calculated hardness and Young's modulus values to those expected for the fused silica sample. It has been shown that area function calibrations made in this way may be affected by the analysis technique not accounting for radial displacement of the indented material[157]. The influence of this is proportional to the H/E ratio of the sample and can lead to underestimation of the contact area of up to 5% for highly elastic materials such as fused silica. As a result there is a systematic error for results on materials with different H/E ratios to the fused silica

reference sample. As no method of directly calibrating the tip (i.e. AFM) was available, it should be noted that should the reader wish to compare any results with those obtained on systems using directly calibrated indenter area functions, corrections to the data may be needed.
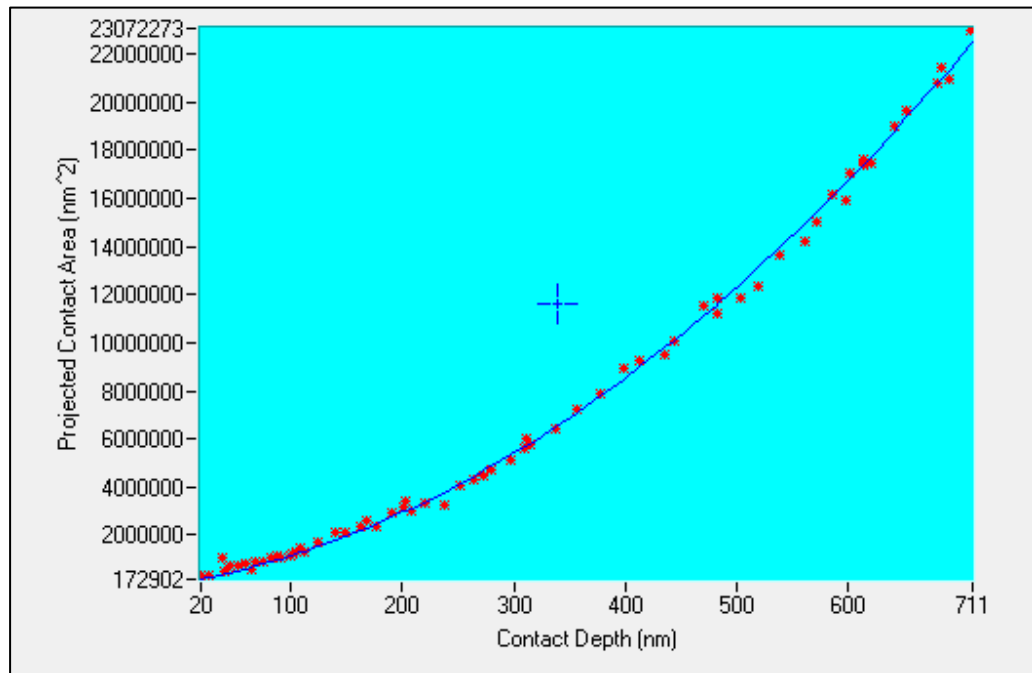

Figure 61: Typical Indenter area function data

Depth calibration

The third calibration needed for the Nanotest™ is the "Depth calibration" this establishes the relationship between the change in output voltage from the capacitance bridge and the distance moved by the indenter. The calibration is then stored and used by the data collection software.

At room temperature the calibration can be performed in two ways. When calibrating the system from new a "Stage encoder" calibration is used. This automated procedure moves the indenter into contact with a relatively hard sample and uses a small load to hold the indenter at the sample surface. The

166

stage motor is then moved a certain number of encoder counts and the change in output voltage from the Wheatstone bridge recorded. This is done over several distances in a number of locations in order to calibrate the relationship between the distance moved and change in output voltage. This calibration assumes there is no penetration of the indenter into the sample surface as the indenter is moved. In the case of calibrations with sharp indenters this is not always the case, therefore in order to ensure the calibration is accurate a reference sample depth calibration, described in the paragraph below, is used.

If the indenter area function is well known, then a reference sample depth calibration is used. A set of high load indentations are made on the fused silica reference sample. These are then analysed by calibration software which analyses the data using different depth calibrations and frame compliance values until it finds the values which returned the expected hardness and modulus for the reference sample. Both frame compliance and depth calibration are altered, as compliance has a greater effect on the calculated Young's modulus, and depth calibration has a larger effect on hardness. It is therefore important to optimise both for the most thorough calibration.

Elevated Temperature Nanoindentation Calibrations

At elevated temperatures the calibration of the Nanotest™ is made more difficult by the lack of a suitable calibration material. Therefore it is necessary to think about the effect of heating the system on the calibrations and look at empirical evidence in order to assess the state of the system. Also the addition of heated components around the depth sensor means that the thermal stability of the system must be considered even more carefully.

Elevated temperature indenter area function and load frame compliance

As mentioned, it is not possible to repeat the room temperature calibrations at elevated temperature due to the lack of a suitable reference sample. When considering the change in area function the same assumptions were made as those published by Schuh et al. [158] In Schuh's work the indenter was treated as the superposition of the self-similar geometry described by its included half angle θ and the rounded tip described by its radius R. The area function of such an indenter, Ap, is shown in Equation 22, where h_c is the contact depth of the indentation.

$$A_p = \frac{\pi}{\cot^2 \theta} \cdot h_c^2 + 4\pi \cdot R \cdot h_c + 4\pi \cdot R^2 \cdot \cot^2 \theta$$

Equation 22

The pyramidal part of the indenter geometry will maintain its self-similarity as the temperature is increased therefore not affecting the overall area function. Only the change in the geometry of the tip is considered to influence the indenter area function. The change in radius is assumed to be linear with temperature as shown in Equation 23. α is the coefficient of thermal expansion.

$$\frac{dR}{dT} = \alpha \cdot R$$

Equation 23

The effect of this on the overall area function can be found by combining Equations 22 and 23 to give Equation 24 shown below[158].

$$\frac{dA_p}{dT} = 4\pi \cdot \alpha \cdot R \cdot \left[h_c + 2 \cdot R.\cot^2 \theta \right]$$

Equation 24

Schuh used this to consider the change in area function of a diamond indenter at test temperatures up to 400K. This has been expanded in the current work to consider both the increased test temperatures, up to 1050K, and the use of cBN and sapphire indenters. For the calculations below, room temperature was taken to be 300K with the change in temperature taken from this value. For both indenter materials two tip radii were examined, 25nm and 500nm, representing the extremes of possible indenter geometry as outlined in the work from Schuh. The thermal expansion coefficient was taken to be $3 \times 10^{-6}K^{-1}$ for diamond at 750K[159] , $1.6 \times 10^{-5}K^{-1}$ for cBN at 1050K [160] and 7×10^{-6} for sapphire[161].
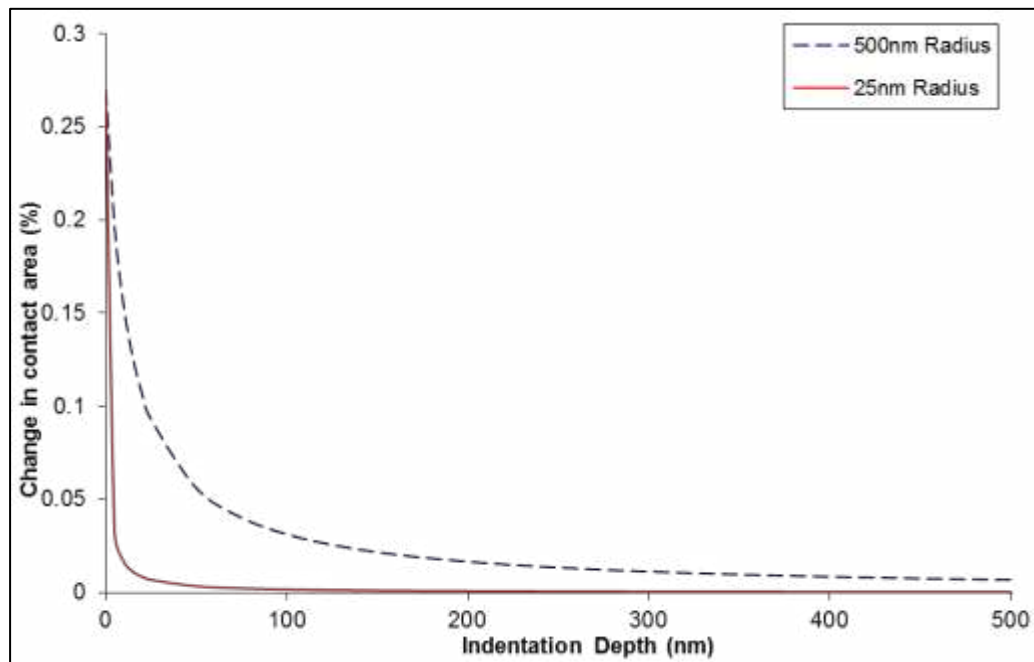

Figure 62: Change in indenter area function for Diamond at 750K compared to room temperature

For diamond there is very little change in contact area compared to room temperature, see Figure 62. Even in the extreme case of an indenter with a 1µm diameter tip the change in contact area is at most ~0.25%, dropping below 0.03% for indentations 100nm or deeper. This change in contact area corresponds to a projected change of less than 1% in both the calculated hardness and Young's modulus for the samples tested and can therefore been treated as insignificant as the standard deviation of results tends to be around 10%.
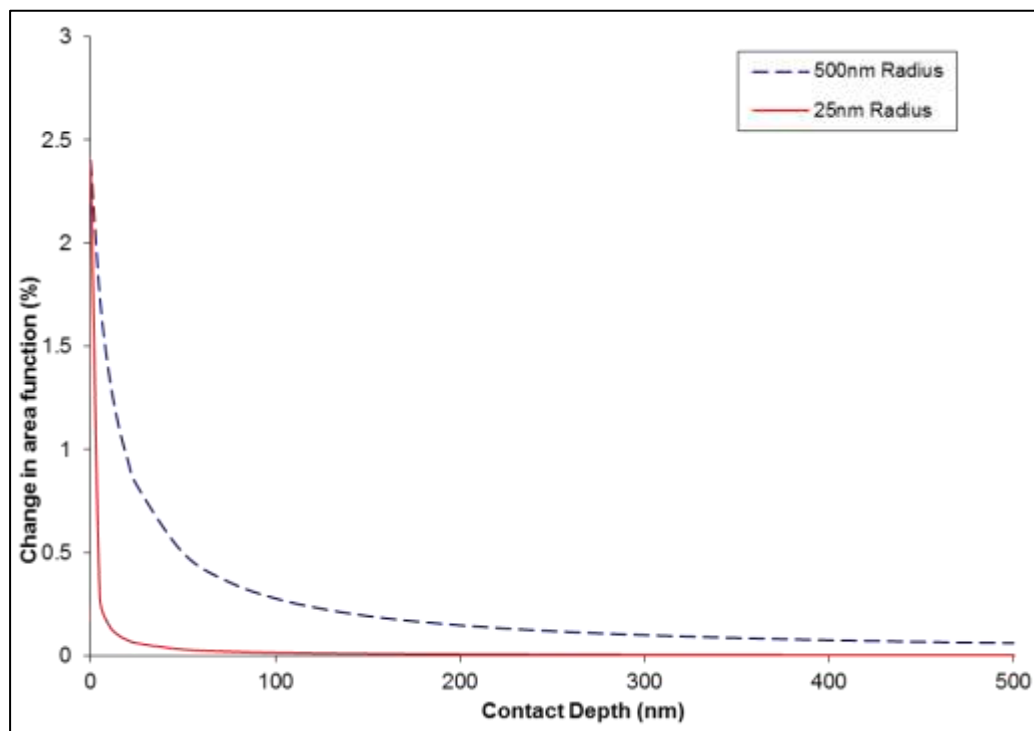

Figure 63: Change in indenter area function for cBN at 1050K

As expected because of its larger thermal expansion, for boron nitride at higher test temperatures the projected change in contact area is significantly larger than for diamond. The results are shown in Figure 63. For the 1µm diameter tip there is ~2% change in the contact area for low depth indentations. However this again drops dramatically as contact depth increases and for indents above 100nm the change is less than 0.3%. A 2% change in area function corresponds to approximately a 4% drop in calculated hardness and a 2% drop in Young's Modulus. Again this is well within the standard deviation of the values observed in experimental data. However in

order to minimise the possible influence of the geometry change experiments performed at these temperatures were performed to depths of at least 300nm.

High Temperature Depth Calibration

When the system is heated the overall ambient temperature of the cabinet increases. The resulting thermal expansion of the hardware leads to the reduction of the spacing of the capacitor plates thus changing the balance of the Wheatstone bridge. Once the bridge has been adjusted it is necessary to repeat the depth calibration at elevated temperature in order to re-establish the relationship between the output voltage and the indenter displacement [77]. As there is no high temperature reference sample only the stage encoder depth calibration can be used at elevated temperatures. As mentioned this could introduce errors as the indenter may penetrate the surface as the stages move. It is therefore important to evaluate any potential errors introduced in this way.

Appendix II - Validation of nanoindentation calibrations

The calibration routine for nanoindentation hardware at room temperatures is well established. Routines to evaluate the frame compliance, indenter area function and depth calibration are all provided by the instrument manufacturer based on experimental procedures reported in the literature [46] and if followed ensure the accuracy of property measurement made using this instrument. At elevated temperatures similar calibration is required in order to ensure accurate results. In the previous section several techniques and assumptions were outlined which will be used when evaluating elevated temperature indentation data. It is less well established how accurate these calibration routines are therefore ways must be determined to assess their use.

The depth calibration can be repeated at elevated temperatures and so what is needed in this case is to ensure that the measurements made for the calibration are still suitable at the test temperatures used. The other two main calibrations, the frame compliance and area function, are assumed to remain constant or approximately constant through the possible test temperature range. The assumption is therefore that the same values determined by the room temperature calibration can be applied to high temperature measurements. In order to test this assumption, measurements were made on standard calibration materials chosen because of their well characterised properties at elevated temperatures.

$$E_r = \frac{\sqrt{\pi}}{2\sqrt{A}\left(C - C_f\right)}$$

Equation 25

As these calibrations are all tied together within the analysis procedure it is difficult to assess each calibration individually by observations of empirical

172

data. However different calibrations will have a different degree of effect on the hardness and Young's modulus. Equation 25 is used to determine the reduced modulus of samples using the Oliver and Pharr method [112], C is the measured compliance, C_f the frame compliance and A the contact area. The reduced modulus is inversely proportional to the contact compliance, $(C-C_f)$, therefore any uncorrected change to the instrument compliance will have a direct effect on the measured sample modulus.

Equation 25 also has a lesser dependence on contact area. As this is only a square root dependence the modulus will be more strongly affected by changes in compliance.

$$H = \frac{P}{A}$$

Equation 26

Equation 26 shows the formula used to determine the hardness from the contact area, A, at maximum load P. The value of hardness is directly related to the contact area, therefore this can be used to evaluate any change in the contact area and depth calibration which is affecting the results. The difficulty is in finding materials for which the hardness measured using depth sensing indentation can be compared with other results. Studies have shown that in materials where pileup occurs it is difficult to directly compare the results to those from conventional measurements due to the inability of depth sensing indentation to account for the additional load support provided by this displaced material [43]. Tests were made on materials for which the results could be readily compared to literature measurements.

Fused silica data

Fused silica was selected as a good material for validation of high temperature tests as its surface properties are completely homogeneous and surface roughness is low so hardness and modulus measurements are very easy to compare to those obtained using other test techniques. Tests were performed to a variety of maximum loads. This was done in order to look at any potential effect of instrument compliance and indenter area function on the results. If there was any change in calibration that has not been detected and corrected it would show in the results.

Experiments were performed at room temperature, 300^oC and 600^oC in order to evaluate any potential change in the calibrations at steps through the potential test temperature range. At each temperature the techniques outlined in the methodology section using a heated indenter were used to ensure that there was isothermal contact between the indenter and sample.

Table 21 shows the results of the indentation experiments on fused silica. Statistical analysis of the data indicates that there is no statistically significant difference between the hardness and modulus from high and low load indentations on fused silica at 300^oC. This indicates that the tip area function of the indenter determined at room temperature is still a good fit at higher temperatures as there is no modification of the low load data. Similarly there is no difference between the moduli at high and low loads indicating that the compliance correction made to the data was suitable. If the compliance correction was not accurate then there would be a larger effect on the high load data which would lead to differences between the modulus values calculated from high and low load data. There is no statistically significant difference between these data so we can assume that the compliance room temperature compliance correction is still valid at this temperature.

Table 21: Fused silica properties

Test Temperature ^{o}C	Maximum Load mN	Young's modulus GPa	Hardness GPa
25	50-100mN	71.7 ± 0.4	9.6 ± 0.4
300	10	78 ± 2	8.8 ± 0.2
	100	79.5 ± 1	9.1 ± 0.2
600	100	81.4 ± 1.6	6.4 ± 0.2

It is well known that the modulus of fused silica increases with temperature. Figure 64 compares the moduli value of the FS tested in this study with those from other sources. Both sets of comparison data are from separate sources in the NIST database, one set was measured by ultrasonic velocity measurements and the other by dynamic resonance methods. The results correlate well at lower temperatures however there is some divergence as the test temperature increases with the nanoindentation data giving higher values. However all of the data points are within 4% or less of the NIST values. Schuh et al [158] noted that the results of nanoindentation and acoustic measurements are not entirely comparable. The values calculated for Young's modulus in Table 6 assume that the Poisson's ratio of the sample is constant though the test temperature. Measurements made on fused silica using ultrasonic velocity measurements have shown that there is actually a slight increase in the Poisson's ratio as the temperature increases [162]. This would bring the nanoindentation results closer to the results from the NIST database. The correction was not made as it was not possible to make measurements on the sample tested in nanoindentation tests.
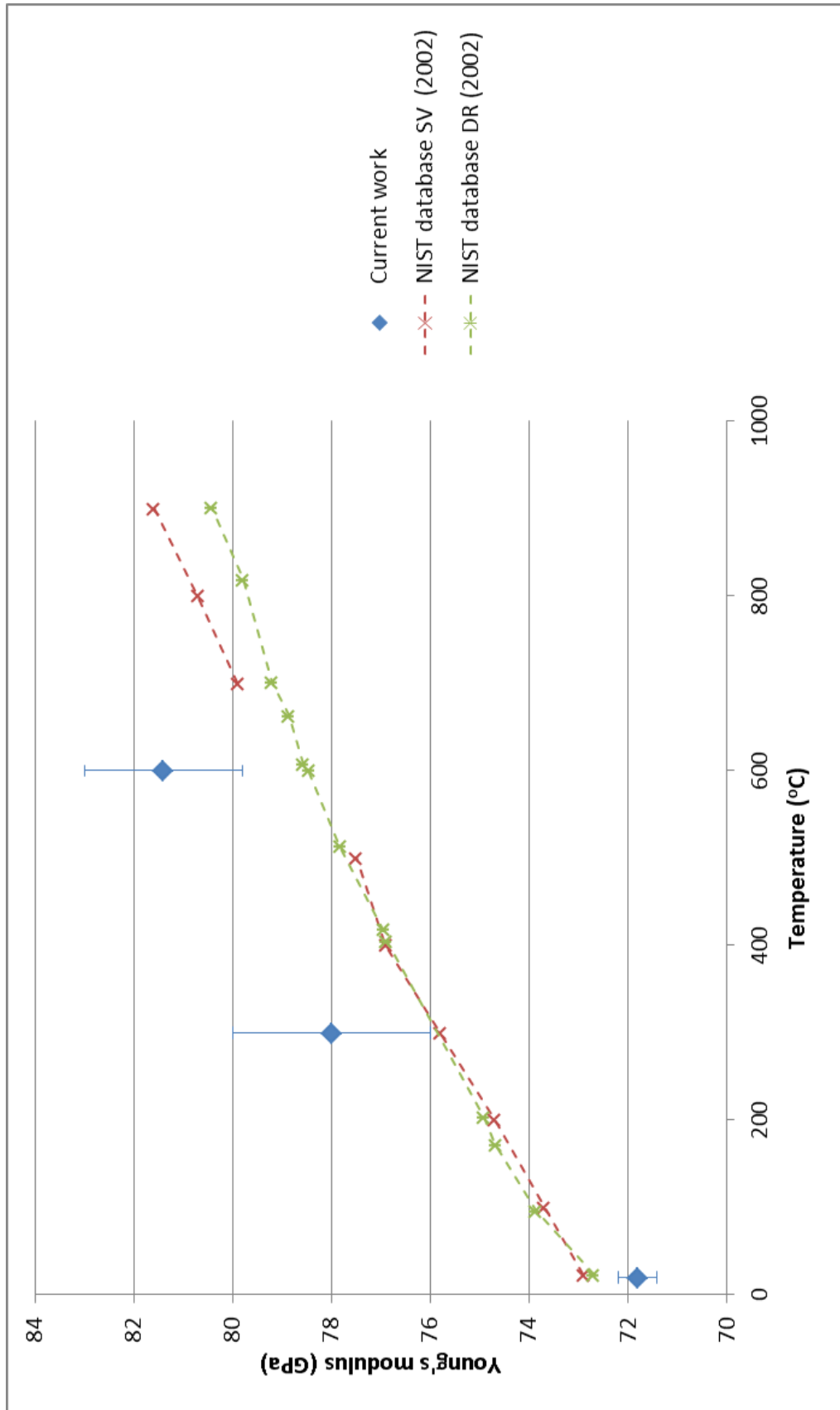
Figure 64: Comparison of indentation data moduli with that obtained by other methods

Appendix II – Validation of nanoindentation calibrations

Figure 65 shows the modulus values for fused silica normalised to the room temperature modulus from a variety of sources. The data are normalised in order to allow examination of the change in modulus with temperature. All of the data from the NIST sources are plotted, these results were gathered using various ultrasonic and dynamic resonance measurements. These data have been plotted to represent the distribution of data from conventional measurements techniques on fused silica. Some of the variation in this data could be due to the relative purity of the fused silica used in each case. The data from Beake and Smith [61] was collected using similar NanoTest hardware to that used in the current study. The basic principles of the loading mechanism remain unchanged although several modifications have been made to the design of the heated indenter and stage since the paper was published. Schuh et al. [158] used a very different design of high temperature indentation hardware to that used in the current study.

The data from the current study falls between the literature indentation results. The Beake and Smith data shows a very high rate of modulus increase compared to the other data. The sample used in this study was from the same source as the fused silica used in the current study therefore we would expect similar results. As mentioned above, the design of the heating stage has changed significantly since the paper was published and the construction is now completely different. It is possible that the old stage was more compliant than the current design and that the compliance increased as the test temperature increased this could explain why the values are much higher than the NIST database data.
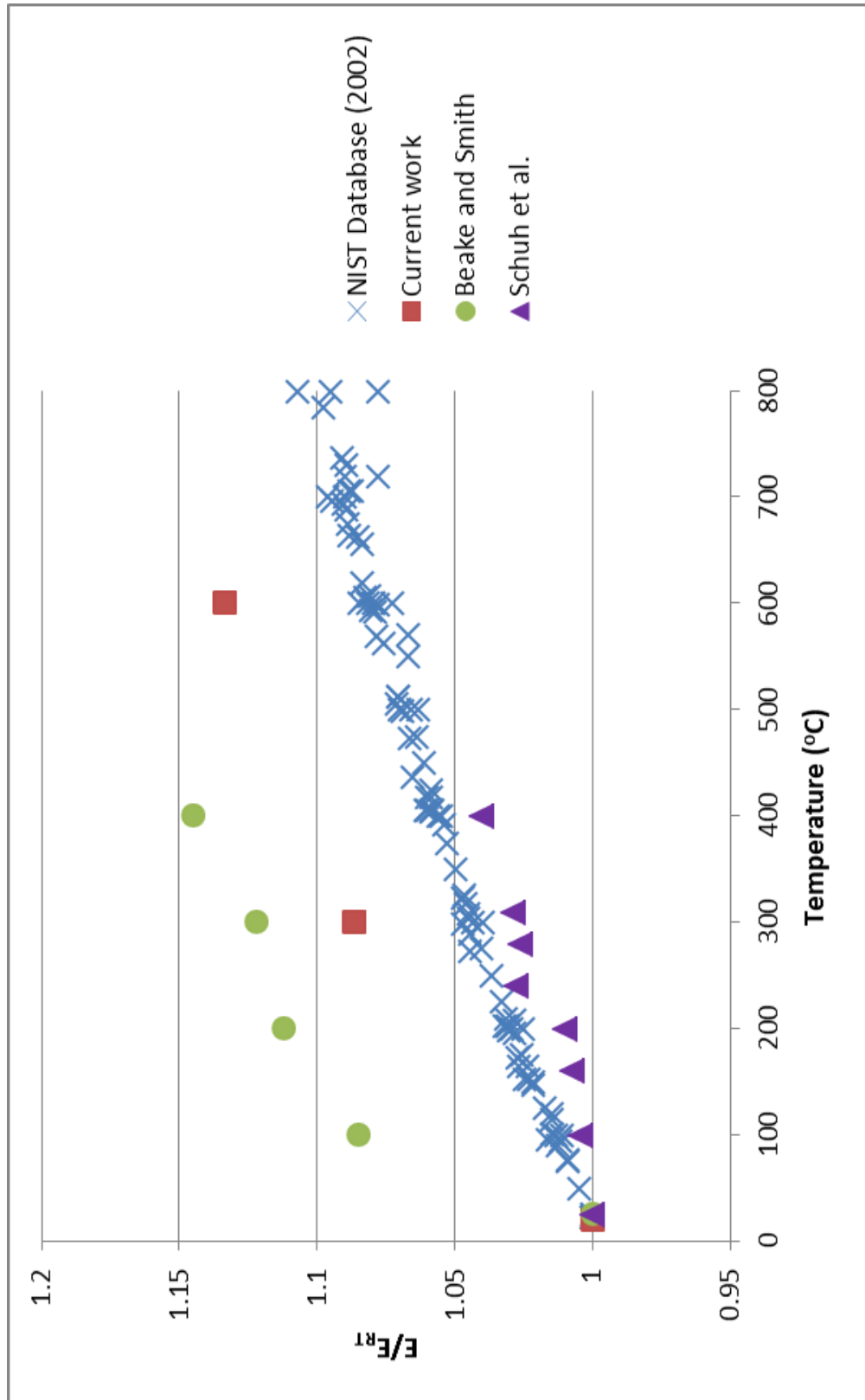
Figure 65: Fused silica normalised modulus comparison

The data from Schuh data is in much better agreement with the data from the dynamic resonance and ultrasonic velocity data [158]. All of the data points are within 2% of the NIST data and show a much less severe increase with temperature than the other nanoindentation data. It should be noted however that the data in this paper was gathered without the use of a heated indenter. As discussed in section 3.3.1, when an unheated indenter is left in contact with a heated sample to stabilise a thermal equilibrium will be reached. However the temperature at the point of contact between the indenter and sample is lower than the temperature of the bulk of the sample therefore it is difficult to assess the exact test temperature for these measurements.

Figure 66 shows the hot nanoindentation hardness measurements from the same sources used in the modulus comparison. All three sets of data show a gradual reduction in hardness with increasing temperature as we would expect for this material. There is no substantial agreement between the hardness data from either of the previous studies and the current work. However the room temperature hardness in each case was determined to be different and there is no literature nanoindentation resource which currently has data from fused silica above 400°C. As outlined in Chapter 2 it is difficult to directly compare nanoindentation hardness to those determined by other methods due to indentation size effects and pileup.

Given the lack of agreement between sources, instead of looking for a direct comparison to the data from previous studies the data was normalised to room temperature values. This way it was possible to examine the trend in the hardness drop for each of the sources. Figure 67 shows these data, it is clearer from this plot that the trend in the change of hardness for this current work falls between those determined in the previous studies.

The results from Beake and Smith indicate that the fused silica is reasonably thermally stable up to 400°C, they report only ~5% drop in hardness in this range. By comparison Shuh et al report a drop of ~20% over the same

temperature range, the thermal stability of the hardness could be affected by differences in the purity of the glass used in each of the studies but the difference may also be related to the methodology used in each case. Beake and Smith used heated indenters in their study attempting to match sample and indenter temperature to ensure isothermal contact. Schuh et al. used unheated indenters and left them in contact with the sample surface to reach a thermal equilibrium before making the indentation. As discussed in section 3.3.1 thermal modelling indicates that this leads to the formation of a region around the indenter contact which is at a lower temperature to the bulk of the sample [115]. This leads to heat flow between the indenter and sample as soon as the indenter starts to move into the sample. Therefore it is difficult to directly compare the results of this method to those from the current work.

The sample used in the current work was from the same source as that in the Beake and Smith work and the methodology and hardware are largely similar therefore the data should be more comparable. This is clear as the 300^oC point is within 4% of the Beake and Smith data, ~6% higher than the Schuh data at the same temperature. There may be some contribution to the difference from the fact that a different indenter material was used in each study. For the Beake and Smith work a diamond indenter was used limiting the test temperature to a maximum of 400^oC, in the current work a cubic boron nitride indenter was used. As discussed in section Appendix I the indenter area function will change slightly as the test temperature increases, however in both works the indentation depth was over 1 μm therefore the change in contact area at 300^oC would be less than 0.01% for both materials and is unlikely to have had a significant effect on the resulting hardness evaluation.
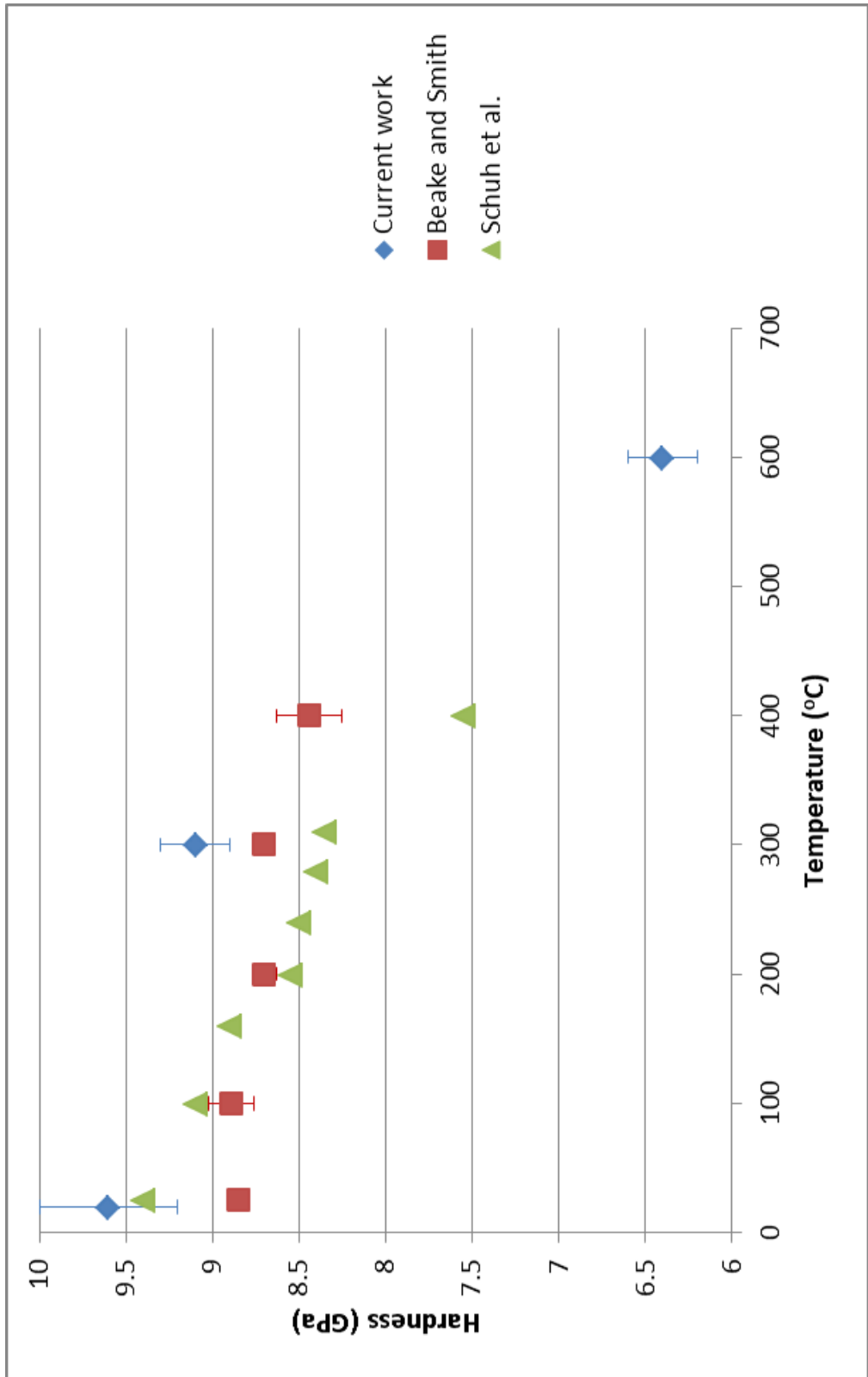
Figure 66: Fused silica hardness data comparison
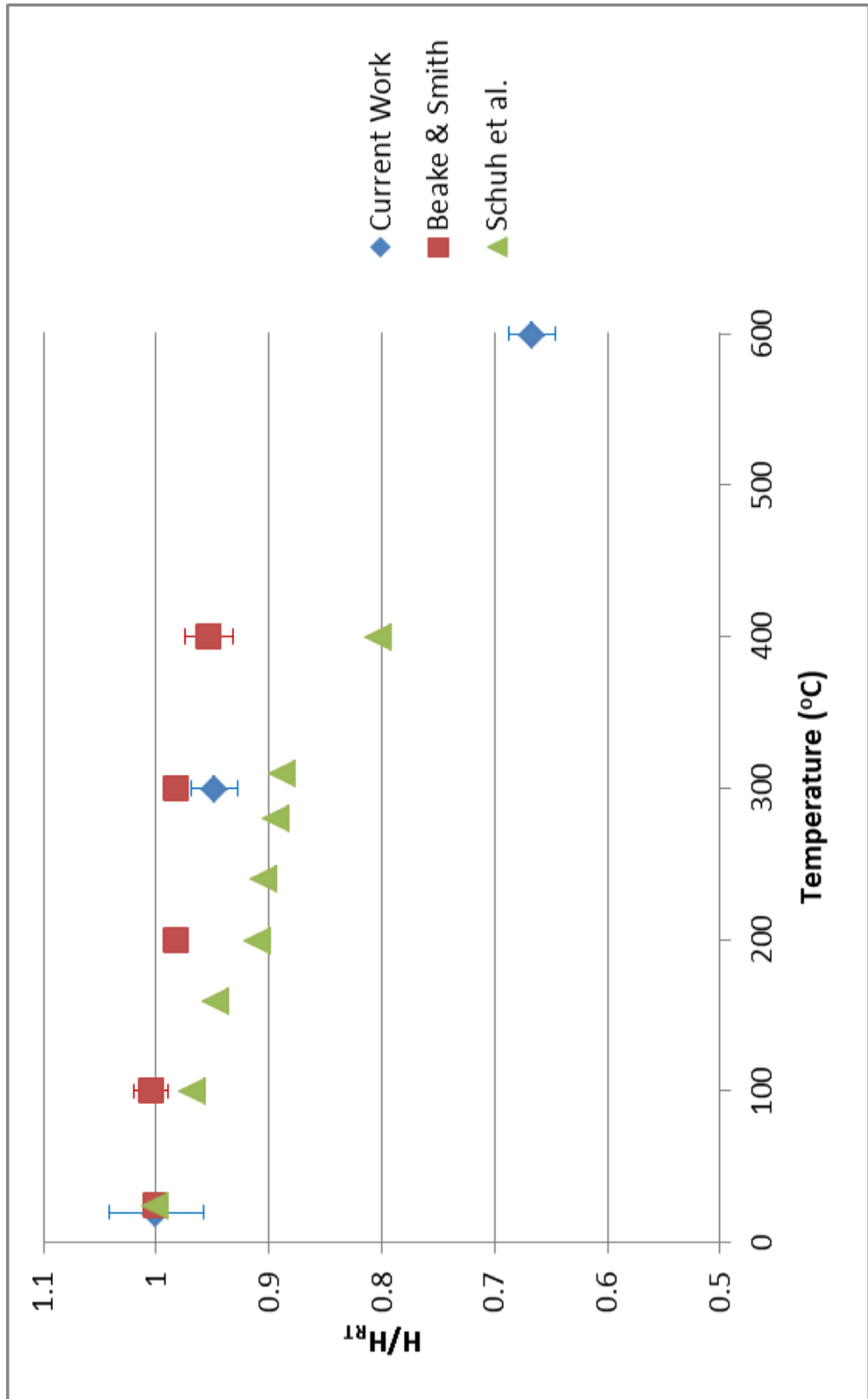
Figure 67: Fused silica hardness data normalised to room temperature values

Gold data

In addition to fused silica, a 24 carat gold sample was tested at both room temperature and 300°C, gold was selected as a suitable material because unlike other readily available materials this gold is virtually the pure element, 99.9% purity. Therefore the surface properties are homogeneous allowing results to be compared to previous studies. The gold used in this work was a jewellers sample mechanically polished then annealed at 600°C for 8 hours to allow the grains to grow preventing grain growth during the nanoindentation tests.

Table 22: Gold data

Test Temperature ^{o}C	Max Load mN	E (GPa)	Hardness (GPa)
25	10	81 ± 8	0.47 ± 0.08
300	10	63 ± 14	0.29 ± 0.1

The results of the testing are shown in Table 22, the modulus of gold at room temperature compares favourably with the literature value of 78.5 GPa [163] so the instrument calibrations can be accepted to be reliable for this material at room temperature. For comparison to elevated temperature data we again look to the study by Beake and Smith. Figure 68 shows the Young's modus against temperature and, as expected for metals, there is a reduction in the modulus with increasing temperature. There is a good correlation between the data from the Beake and Smith paper and the current work, no error bars are available for the literature data. The errors in the data from the current study are due to surface roughness introduced by the grain growth during annealing affecting the scatter of the hysteresis data. What is important in this comparison is that the data in the Beake and Smith paper data was collected using a diamond indenter where the current study used a cubic boron nitride indenter. It is therefore reasonable to say that at this test

temperature the boron nitride indenter has not undergone a substantial change in its area function compared to a diamond at the same temperature.

Figure 69 shows a similar comparison plot for the hardness determined in both studies, this data has been normalised to the room temperature values. This has been done to allow direct comparison of the change in with hardness temperature. For metallic materials the sample preparation can have an effect on the hardness, work hardening through polishing, stress relaxation through annealing etc. There is no information given about the preparation in the Beake and Smith paper, therefore it is not possible to be more specific about possible reasons for the differences in the room temperature hardness. It is clear however that the hardness drop with temperature follow the same trend in both cases.
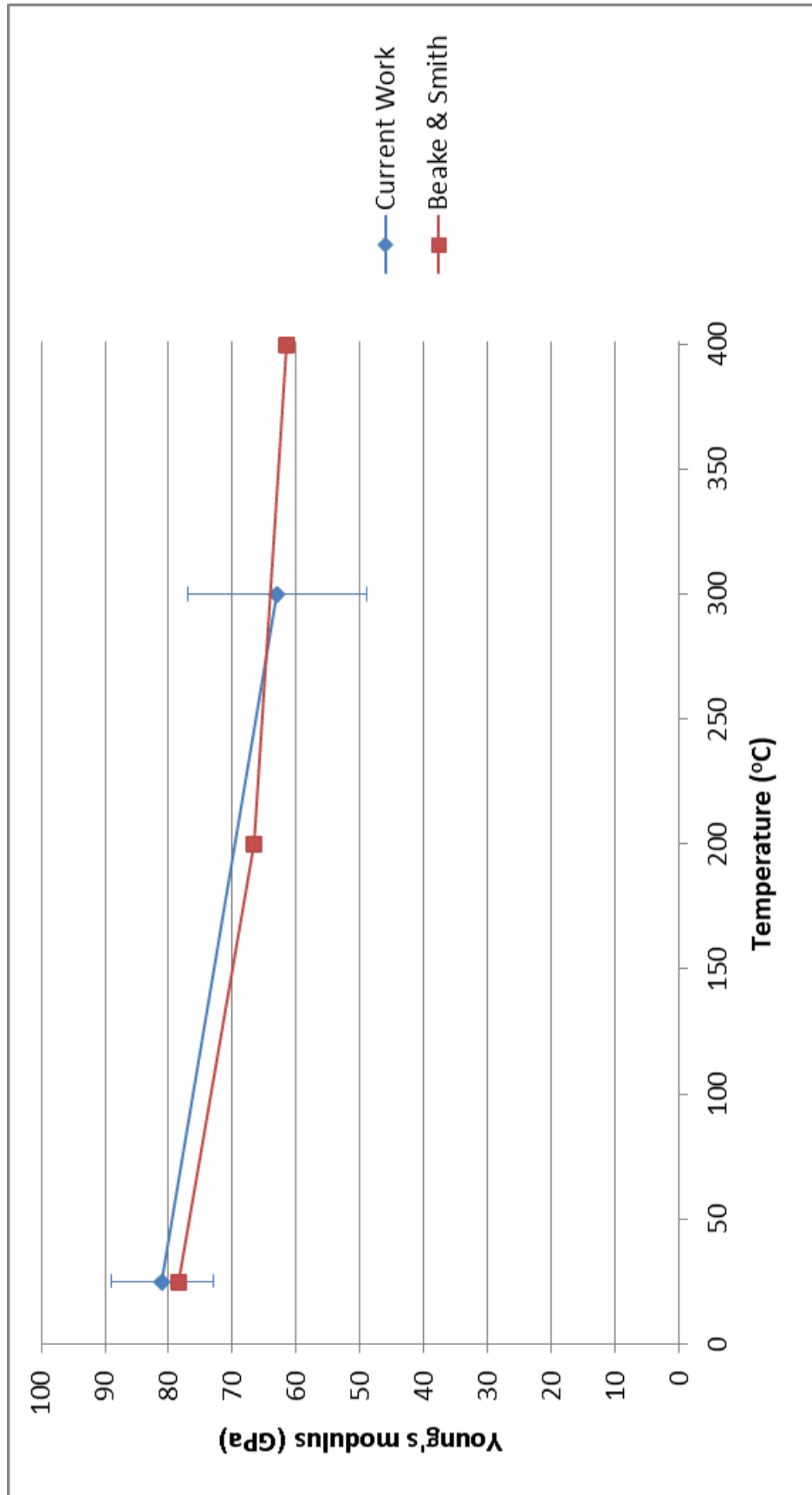
Figure 68: Gold modulus against temperature
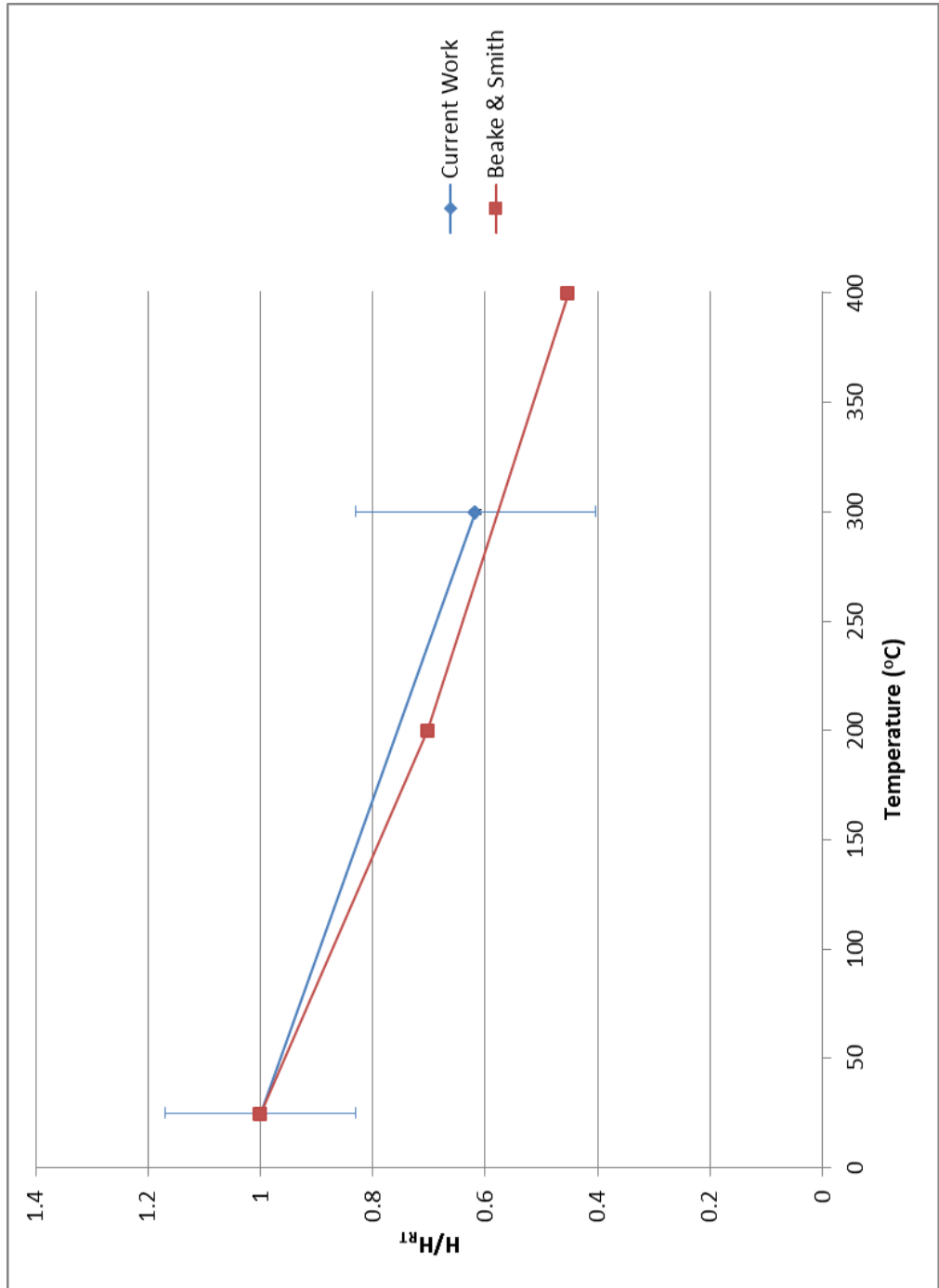
Figure 69: Gold hardness

Sapphire data

As well as gold and fused silica a single crystal sapphire sample was used to further examine the validity of the calibration assumptions. Sapphire was selected as the H/E ratio is very different from the previous 2 samples therefore any effect from the fused silica reference calibration of the area function may be visible in this data. The sample surface of the sapphire is homogenous making this a useful sample for analysis. Table 23 shows the indentation results for the sapphire sample tested at both room temperature and 300°C. The room temperature modulus is in line with results reported in the literature for this material [164-166], in addition to this the hardness results also compare favourably with previous works[167].

Table 23: Sapphire data

Test Temperature ^{o}C	Max Load mN	E (GPa)	Hardness (GPa)
25	50	405 ± 3	28.4 ± 0.4
500	50	400 ± 14	17.6 ± 0.4

In order to examine the change in modulus with temperature reference was again made to the NIST database of ceramic materials. Figure 70 shows the drop in modulus with temperature from several sources in the NIST database and the current study. As there was some variation in the room temperature modulus between sources each has been normalised to its room temperature value to allow direct comparison of the trends in decreasing modulus. The data from source 86 were gathered using sonic resonance methods [164], as with the fused silica data the results from indentation experiments return a higher modulus than these data.
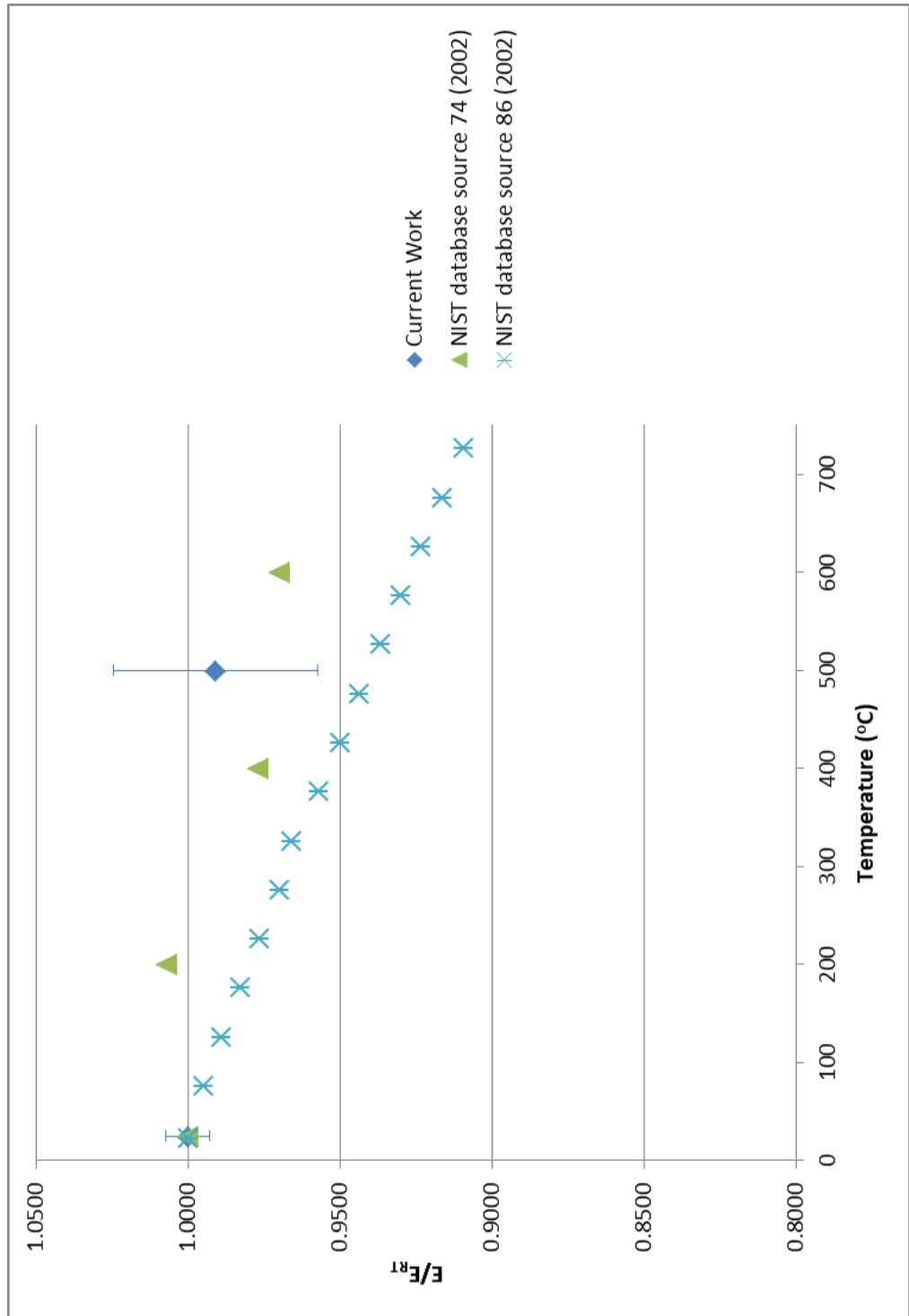
Figure 70: Sapphire Young's modulus vs. Temperature

The data from source 74 were collected using bending methods [168], interestingly there is a much more direct correlation between the bending test and nanoindentation data than resonance data suggesting that this may be the case. What is clear is that for this sample the results are consistent with those reported in literature and there are no obvious calibration issues affecting the results.

Summary

When viewed from the stand point of assessing the validity of the calibration assumptions, the fused silica data indicates that there may have been a small change in the instrument compliance as the temperature increased. A higher frame compliance would lead to a higher than expected measured modulus value as observed in these experiments when compared to the NIST database data. However it has been noted by Schuh et al. that acoustic measurements are performed without significant hydrostatic pressure in the measurement region, in indentation measurements a hydrostatic stress field is generated in the measured volume. Therefore it is unclear whether it is possible to directly compare the results of these different techniques. Nanoindentation data shows a much better correlation to those gathered using bending methods, in these tests compressive stresses are also introduced into the test volume. Therefore the test conditions are more similar to nanoindentation tests than those performed using resonance methods.

Comparison with previous indentation studies indicates that the chosen calibration and experimental procedure are sufficient to give reproducible indentation measurements on both crystalline materials and metals. The results compare well with those from these previous studies and therefore it should be possible to replicate experiments performed using this technique or compare data generated by this work to other nanoindentation studies.